ABSTRACT

Title of dissertation: TOWARDS AN IMPROVED LONG-TERM
DATA RECORD FROM THE ADVANCED
VERY-HIGH RESOLUTION RADIOMETER:
EVALUATION, ATMOSPHERIC CORRECTION,
AND INTERCALIBRATION

Andrés E. Santamaría Artigas
Doctor of Philosophy, 2021

Dissertation directed by: Christopher Justice, Chair and Professor,
Department of Geographical Sciences

Long-term data records from satellite observations are crucial for the study of land surface properties and their long-term dynamics. The AVHRR long term data record (LTDR) is an ongoing effort to generate a consistent climate record of daily atmospherically corrected observations with global coverage that is suitable for long term studies of the Earth surface. In this dissertation, I identified three areas for the improvement of the LTDR: (1) The comprehensive evaluation of the LTDR performance and characterization if its uncertainties. (2) The retrieval of water vapor information from AVHRR data for a more accurate atmospheric correction. (3) The recalibration of the record to address inconsistency issues. The first study consisted on a global long-term evaluation of the LTDR with matched observations from the Landat-5 Thematic Mapper instrument. Results from this evaluation showed that the record performance was close to the proposed specification. The second study proposed a method for the retrieval of water vapor from

AVHRR data, which provides a crucial input for the atmospheric correction process. Evaluation of the retrieved values with reference datasets showed excellent results, with a water vapor error lower than 0.45g/cm2. Finally, the last chapter proposed a novel method for the selection of stable areas suitable for satellite intercalibration and for the derivation of recalibration coefficients. The evaluation of the original and recalibrated record showed that for most cases the recalibrated record performed better.

TOWARDS AN IMPROVED LONG-TERM DATA RECORD
FROM THE ADVANCED VERY-HIGH RESOLUTION
RADIOMETER: EVALUATION, ATMOSPHERIC CORRECTION,
AND INTERCALIBRATION

by

Andrés E. Santamaría Artigas

Dissertation submitted to the Faculty of the Graduate School of the
University of Maryland, College Park in partial fulfillment
of the requirements for the degree of
Doctor of Philosophy
2021

Advisory Committee:
Professor Christopher Justice, Chair
Professor Belén Franch, Co-Chair
Professor Jean-Claude Roger
Professor Eric F. Vermote
Professor Sergii Skakun

Dedication

To my grandparents

Acknowledgments

To Vale♡, my love and wife, thank you for always being there. Your support these years has been essential. Thanks for believing in me and for helping me keep my sanity in the most challenging moments. I love you.

To my family. Carmen, Patricio, Francisca, y Marisol; who always pushed me to find and follow what I really wanted to do. I am incredibly lucky and tremendously grateful.

Thanks to Jose Luis, I don't think I could have asked for a better Ph.D. companion to share this process with. Your approach to life and research -with authenticity and honest curiosity- is something that I truly admire.

To Belen Franch, thanks for guiding me through this stage and for always supporting me when I needed it. Thanks also for your advice, both professional and personal.

To Jean-Claude Roger, for your continuous effort in making Jose-Luis and me make the most out of this program, and for always being committed to making everyone at SALSA feel part of more than just a research group.

To Sergii Skakun, for our talks that helped provide context to the research and your insights as an early-career scientist.

I want to give particular thanks to Eric Vermote, who welcomed me to the

team and gave me an incredible opportunity to work among the best researchers in our field. Thanks for your continuous advice and for helping me keep focus.

To Chris Justice, for reminding me to think about the broader impact of my research, something that can be easily forgotten between datasets and lines of code.

Finally, to the friends that during these years made me feel at home. To Dé, Shannons, Motzerlaskos, Latinlovers, and FitzGaugheys.

Table of Contents

List of Tables

List of Figures

List of Abbreviations

AOD	Aerosol Optical Depth
APU	Accuracy, Precision, and Uncertainty
AVHRR	Advanced Very High Resolution Radiometer
BELMANIP2	Benchmark Land Multisite Analysis and Intercomparison of Products Version 2
BRDF	Bidirectional Reflectance Distribution Function
CMG	Climate Modeling Grid
CWV	Columnar Water Vapor
FAPAR	Fraction of Photosynthetically Active Radiation
H0	Hyperion hyperspectral radiometer
LAI	Leaf Area Index
LTDR	Long-Term Data Record
MODIS	Moderate Resolution Imaging Spectroradiometer
NASA	National Aeronautics and Space Administration
NIR	Near Infrared
NOAA	National Oceanic and Atmospheric Administration
PICS	Pseudo Invariant Calibration Sites
POES	Polar-Orbiting Operational Environmental Satellites
RSR	Relative Spectral Response
SBAF	Spectral Band Adjustment Factor
TIROS-N	Television Infrared Operational Satellite Next-Generation
TM5	Landsat 5 Thematic Mapper

Chapter 1:   Introduction

Satellite remote sensing has become a crucial source of quantitative information for the global monitoring and study of our planet. Consistent long term records from satellite observations are essential for the better understanding of extreme events and changes in our planet to an extent that would not be possible otherwise [1–5]. Among long-term satellite records, the Advanced Very High-Resolution Radiometer (AVHRR) onboard NOAA polar-orbiting environmental satellites (POES) provides the longest time-series of daily global observations.

1.1   The Advanced Very High-Resolution Radiometer

The first AVHRR was launched onboard the Television Infrared Operational Satellite Next-Generation (TIROS-N) in October 1978 with the objective of studying global cloud coverage, land characteristics, sea surface temperature, ice, and snow cover [5]. Forty years later, in November 2018, the last AVHRR instrument was launched onboard Metop-C, marking the end of the POES program. During that forty years, the AVHRR instrument was included on over 18 POES missions (Table 1.1).

Platform	Instrument	Launch Date	Service Start	Service End
TIROS-N	AVHRR/1	10/1978	10/1978	01/1980
NOAA-6	AVHRR/1	06/1979	06/1979	11/1986
NOAA-7	AVHRR/2	06/1981	08/1981	06/1986
NOAA-8	AVHRR/1	03/1983	05/1983	10/1985
NOAA-9	AVHRR/2	12/1984	02/1985	05/1994
NOAA-10	AVHRR/1	09/1986	11/1986	09/1991
NOAA-11	AVHRR/2	09/1988	11/1988	09/1994
NOAA-12	AVHRR/2	05/1991	05/1991	12/1994
NOAA-13[*]	AVHRR/2	08/1993	–	–
NOAA-14	AVHRR/2	12/1994	12/1994	05/2007
NOAA-15	AVHRR/3	05/1998	05/1998	Ongoing
NOAA-16	AVHRR/3	09/2000	09/2000	06/2014
NOAA-17	AVHRR/3	06/2002	06/2002	04/2013
NOAA-18	AVHRR/3	05/2005	08/2005	Ongoing
NOAA-19	AVHRR/3	02/2009	06/2009	Ongoing
Metop-A	AVHRR/3	10/2006	06/2007	Ongoing
Metop-B	AVHRR/3	09/2012	04/2013	Ongoing
Metop-C	AVHRR/3	11/2018	07/2019	Ongoing

[*]NOAA-13 failed 12 days after launch and collected no data.

Table 1.1: Satellite platforms that carry the AVHRR instrument.

There have been three revisions of the AVHRR instrument (Table 1.2): The first revision, AVHRR/1, was a four-band radiometer flown onboard the TIROS-N and NOAA-6/-8/10 platforms. The next model, AVHRR/2, narrowed the band-pass of the existing $11\mu m$ thermal band and added a second one centered at $12\mu m$; it was flown on NOAA-7/-9/-11/-12/14 platforms. Finally, AVHRR/3 added an extra band on the short-wave infrared centered at $1.6\mu m$[1] and was first flown on NOAA-15. Note that while the visible bands band-pass is maintained between AVHRR sensors, the specific spectral responses vary between instruments, which can generate biases in the data record [6].

---

[1]Note however that only one of the $1.6\mu m$ or $3.7\mu m$ bands is active at a given time.

	Bandpass (μm)		
Band	**AVHRR/1**	**AVHRR/2**	**AVHRR/3**
1	0.580 - 0.680	0.580 - 0.680	0.580 - 0.680
2	0.725 - 1.100	0.725 - 1.100	0.725 - 1.000
3A	Not Present	Not Present	1.580 - 1.640
3B	3.550 - 3.930	3.550 - 3.930	3.550 - 3.930
4	10.500 - 11.500	10.300 - 11.300	10.300 - 11.300
5	Not Present	11.500 - 12.500	11.500 - 12.500

Table 1.2: Spectral bands available on AVHRR instruments

Throughout the more than forty years in which AVHRR has provided continuous daily observations at global scale, its data have contributed significantly to our understanding of Earth's atmosphere, land, and ocean processes, and their long term dynamics. A comprehensive review of these was recently published by [5].

1.2 The AVHRR Long Term Data Record

The AVHRR long term data record (LTDR) is an ongoing effort to generate a consistent climate record of daily atmospherically corrected observations with global coverage that is suitable for long term studies of the Earth surface [7,8]. The LTDR is generated using L1b Global Area Coverage (GAC) [9] data from AVHRR instruments onboard seven POES platforms: N07, N09, N11, N14, N16, N18, and N19 (Table 1.3). The LTDR has been used for studies at both regional and global scales, and for areas such as agricultural yield estimation [8], agricultural drought risk quantification [2], long-term global land change mapping [3]; and the estimation of parameters such as albedo [10], aerosol loading [11,12], and Leaf Area Index (LAI) and Fraction of Photosynthetically Active Radiation (FAPAR) [13].

Platform	AVHRR Sensor	Period	
NOAA-7	AVHRR/2	1982 - 1985	
NOAA-9	AVHRR/2	1985 - 1988	
NOAA-11	AVHRR/2	1988 - 1994	
NOAA-14	AVHRR/2	1995 - 2000	pre-MODIS
NOAA-16	AVHRR/3	2000 - 2005	MODIS era
NOAA-18	AVHRR/3	2005 - 2009	
NOAA-19	AVHRR/3	2009 - 2020	

Table 1.3: AVHRR instruments in the LTDR

Since its inception[2] in the early 2000s, the LTDR team has developed a processing chain that includes an accurate geolocation with an error lower than one pixel [8]; absolute calibration accounting for sensor degradation using observations of ocean and clouds [14], and desert sites [15]; atmospheric correction based on the Second Simulation of the Satellite signal in the Solar Spectrum (6S) radiative transfer code [16]; the homogenization from the GAC resolution (4000m at nadir) to the 0.05° Climate Modeling Grid (CMG) (5600m); normalization of directional reflectance using the Vermote-Justice-Breon (VJB) method [17], and cloud masking based on albedo thresholds derived from Moderate Resolution Imaging Spectroradiometer (MODIS) information [18]. Figure 1.1 shows the processing steps required to generate a daily LTDR file from corresponding AVHRR L1b GAC data. These steps are further detailed in the following sections.
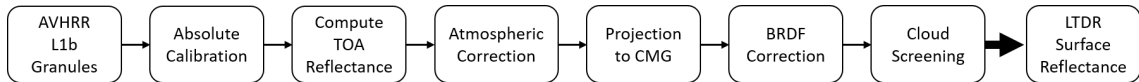
Figure 1.1: Processing steps for the generation of an AVHRR LTDR file.

---

[2]Saleous, N. "Long Term Land Data Record". MODIS Science Team Meeting, July 2004.

1.2.1 LTDR Absolute Calibration

A consistent well calibrated data set is crucial for the generation a long term data record. Calibration of the AVHRR reflective bands is problematic due to the lack of an on-board calibration system [19], which has made the topic of AVHRR calibration popular in the literature for many years [14,15,20–22] [3], and has pushed the development and improvement of several of the post-launch calibration techniques currently in use.

For the LTDR, the calibration of AVHRR data is done through the "Ocean and Clouds" method [14]. This method uses observations of high-altitude, bright clouds to inter-calibrate the Red and NIR bands. Then, off-nadir ocean observations are used for the absolute calibration of the Red band, which signal (after accounting for aerosols) is mainly due to molecular scattering and can be accurately estimated using radiative transfer models. While the results from this method have been evaluated positively for some of the AVHRR instruments [8,15], recent studies have evidenced inconsistency issues that still persist [3,4,23].

1.2.2 LTDR Atmospheric Correction

The atmospheric correction is the process by which the perturbation of remotely sensed signals due to atmospheric effects is removed. It is essential for the estimation of physical derived parameters of the surface and their multi-temporal analysis. Therefore, it is important to apply this process as accurately as possi-

---

[3]These are only a few examples of many. A more complete review is given on [22].

ble. Atmospheric constituents can affect the signal measured by the remote sensor through the scattering and absorption processes. Scattering is the process in which electromagnetic radiation is forced to deviate from a straight trajectory after interacting with particles in the atmosphere, and it may increase or decrease the signal that reaches the sensor. In contrast, absorption can only decrease it. The atmospheric correction process attempts to estimate and remove these effects from the signal measured by the remote sensor bands that are impacted. This process depends primarily on **(1)** the model selected to simulate the atmospheric constituents influence on the at-sensor signal, and **(2)** on the ancillary information used to describe those constituents.

The LTDR atmospheric correction is based on Equation 1.1, which describes the reflectance from a Lambertian surface measured by the AVHRR sensor at the top of the atmosphere[4].

$$\rho_{TOA} = Tg_{O_2}Tg_{O_3}\left(\rho_R + \frac{T_R Tg_{H_2O}\rho_s}{1 - S\rho_s}\right) \tag{1.1}$$

where ρ_{TOA} is the reflectance at the top of the atmosphere measured by AVHRR; ρ_s is the surface reflectance; Tg_{O_2} is the oxygen transmittance; Tg_{O_3} is the ozone transmittance; Tg_{H_2O} is the water vapor transmittance; and ρ_R, T_R and S are, respectively, the Rayleigh atmospheric reflectance, transmittance, and spherical albedo.

For the LTDR, Rayleigh contributions are simulated using analytical formulas developed by [24], and the influence of atmospheric gases on the AVHRR signal is

---

[4]Note that this equation does not account for the effect of stratospheric or tropospheric aerosols and neither does the current LTDR atmospheric correction.

modeled using the Second Simulation of the Satellite signal in the Solar Spectrum (6S) radiative transfer code [16]. The 6S code has been thoroughly validated [25–27] and has uncertainties lower than $0.05\rho + 0.005$ (where ρ is the surface reflectance value) [28, 29].

1.2.2.1   Effect of atmospheric gases on the AVHRR signal

As shown in Equation 1.1, the LTDR atmospheric correction accounts for three[5] main gases on the AVHRR signal: Water Vapor, Ozone, and Oxygen. Figure 1.2 shows the spectral transmittance of these three gases and their specific effect on the AVHRR signal is described below.
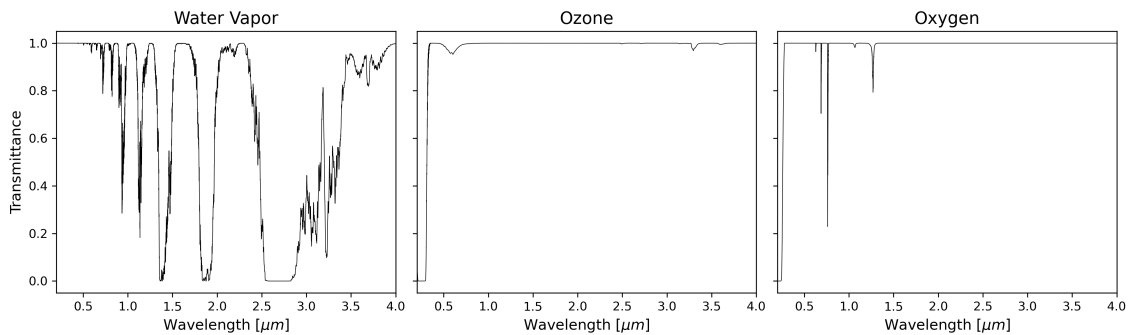
Figure 1.2: Spectral Transmittance of Water Vapor, Ozone, and Oxygen.

Water Vapor:

Atmospheric water vapor primarily absorbs electromagnetic radiation at wavelengths longer that $0.7\mu m$. This absorption has a small impact on the AVHRR Red band but can strongly affect the NIR due to its wide bandwidth [30]. On the LTDR, the

---

[5]While there are other gases that affect the signal, their effect is overshadowed by these three.

water vapor transmittance (Tg_{H_2O}) is computed as shown in Equation 1.2:

$$Tg_{H_2O} = exp\left(-a(Mu_{wv})^b\right) \tag{1.2}$$

where M is the airmass, u_{wv} is the integrated water vapor content in , and a and b are band specific coefficients derived from 6S simulations.

Ozone

Ozone molecules in the atmosphere limit Earth observations at wavelengths shorter than $0.35\mu m$ and are a source of significant absorption between 0.55 and $0.65\mu m$. This effect, which is quantified by the ozone transmission function (Tg_{O_3}), can have significant effects over the AVHRR Red band but is negligible over the NIR [30]. For the LTDR, Tg_{O_3} is computed as shown in Equation 1.3:

$$Tg_{O_3} = exp\left(-aMu_{O_3}\right) \tag{1.3}$$

where M is the airmass, u_{O_3} is the total ozone amount in [cm/atm], and a is a band specific coefficient derived from 6S simulations.

Oxygen:

Oxygen has a narrow absorption band located at around $0.7\mu m$ which weakly affects both the Red and NIR bands. The oxygen transmittance (Tg_{O_2}) can be written as a function of the air mass and surface pressure, and in the LTDR is computed as

shown in Equation 1.4:

$$Tg_{O_2} = exp\left(-(aP)(M^{exp(-(b+cP))})\right) \qquad (1.4)$$

where M is the airmass, P is the surface pressure in [atm], and a, b, and c are band specific coefficients derived from 6S simulations.

1.2.2.2 LTDR atmospheric characterization

The atmospheric correction process previously described requires knowledge of specific atmospheric variables and constituents, i.e. surface pressure, ozone concentration, and water vapor content. In the LTDR, this information is obtained from satellite data, gridded observations, and reanalysis sources (Table 1.4).

Sources[1]	Variables[2]	Period	Spatial Res.[3]	Temp. Res.
MODIS [31]	WV	2000-2020	0.05° x 0.05°	daily
TOMS [32]	O3	1984-2005	1.00° x 1.25°	daily
NCEP/GDAS [33]	O3/WV/P	1984-2020	1.00° x 1.00°	6 hours
NCEP R1 [34]	O3/WV/P	1984-2020	2.50° x 2.50°	6 hours

[1]Data selection is prioritized as: MODIS/TOMS→NCEP/GDAS→NCEP R1.
[2]O3: Ozone; WV: Water Vapor; P: Surface Pressure.
[3]Spatial resolution is shown in latitude x longitude.

Table 1.4: Ancilliary data used in the LTDR atmospheric correction over land

The selection of which data source to use depends on the time period of the AVHRR data being corrected and on the availability of information for a given area. It is important to note that the spatial and temporal resolution varies within data sources, and that while this might not be a problem for slow spatially and temporally varying variables such as the surface pressure and ozone concentration, it

could present an issue for the water vapor content, which varies strongly in time and space [29].

1.2.3 LTDR BRDF Normalization

One of the benefits of the AVHRR LTDR for long term analysis of the surface is that it provides Bidirectional Reflectance Distribution Function (BRDF) corrected surface reflectance. That is, surface reflectance that has been normalized to a standard observation geometry such that signal variations due to changes in the sun-sensor geometry of individual observations are minimized. In particular, the LTDR uses the Vermote-Justice-Breon (VJB) method [17] to normalize the observations to a sun zenith angle (θ_s) of 45°; view zenith angle (θ_v) of 0°; and relative azimuth angle (ϕ) of 0°.

The surface reflectance (ρ) for a certain geometric configuration (Θ) can be expressed as:

$$\rho(\Theta) = k_{iso} + k_{vol}F_{vol}(\Theta) + k_{geo}F_{geo}(\Theta) \qquad (1.5)$$

where Θ represents the observation conditions of solar zenith angle (θ_s), view zenith angle (θv), and relative azimuth angle between sun and sensor (ϕ); F_{geo} and F_{vol} are the geometric and volumetric scattering components that characterize the shape of the bidirectional reflectance distribution function (BRDF) [35, 36]; and k_{iso}, k_{vol}, and k_{geo} are isotropic, volumetric, and geometric kernels. It is possible to rewrite

the model using variables $V = \frac{k_{vol}}{k_{iso}}$ and $R = \frac{k_{geo}}{k_{iso}}$ proposed by [17] as:

$$\rho(\Theta) = k_{iso}(1 + VF_{vol}(\Theta) + RF_{geo}(\Theta)) \qquad (1.6)$$

Both V and R can be derived as a function of the Normalized Difference Vegetation Index (NDVI) [17,37]. If we assume no change in the surface between two observations (A, B) with different geometric configurations, we can express this relationship as:

$$\rho AVHRR(\Theta_B) = \rho AVHRR(\Theta_A)\frac{(1 + VF_{vol}(\Theta_B) + RF_{geo}(\Theta_B))}{(1 + VF_{vol}(\Theta_A) + RF_{geo}(\Theta_A))} \qquad (1.7)$$

On the LTDR BRDF correction, the V and R parameters are obtained from a global database generated from MODIS data between 2010-2011 [17]. The matter of whether to use VJB parameters derived from MODIS or from AVHRR to normalize the BRDF effects of AVHRR surface reflectance was analyzed by [38], who found that VJB parameters derived from MODIS performed 3% (Red) to 5% (NIR) better than ones derived from AVHRR itself.

1.2.4 LTDR Cloud Screening

In the current LTDR version, cloud screening is performed by comparing the BRDF-corrected AVHRR surface reflectance against thresholds derived from monthly climatological values of MODIS Red and NIR BRDF-corrected reflectances. This per-pixel climatology was computed using 10 years of MODIS Aqua data [18]. However simple in its implementation, this approach has been shown to provide

higher accuracy than the "Clouds from AVHRR" (CLAVR) algorithm [39] which was used on previous versions of the LTDR [8]. More recently, a new approach based on the combination AVHRR, MODIS, and reanalysis data has been proposed for implementation on the next version of the LTDR [40].

1.2.5   LTDR Performance Evaluation

Despite the benefit that LTDR data can provide for long-term studies of Earth's surface processes [2–4, 8, 23], surprisingly few published articles evaluate its performance and uncertainties. In this regard, previous studies have focused on either assessing the calibration of top-of-atmosphere (TOA) values from AVHRR [21,22,41] or evaluating surface reflectance values for only a particular set of AVHRR instruments [14, 15]. There is only one publication from the LTDR development team that provides some information on the record's performance [8]; however, it is limited to the MODIS-era and only gives globally averaged information. Until now (that is, until the results from this thesis were published [42]), there was no comprehensive evaluation of the entire surface reflectance record and no information on the magnitude and spatiotemporal distribution of its uncertainties.

1.3   Research Objective

The main goal of this dissertation is to advance the development of the AVHRR Surface Reflectance Long Term Data Record. To this end, I selected three key areas which appeared to be most relevant for potential improvement of the AVHRR record:

(1) The need of a comprehensive evaluation of the performance of the record and the spatiotemporal-temporal characterization of its uncertainties (1.2.5); **(2)** The lack of an adequate water vapor source for the atmospheric correction process during the pre-MODIS era (1.2.2.2); and **(3)** calibration inconsistencies present between the AVHRR instruments in the data record (1.2.1).

1.4   Research Questions and Thesis Structure

This thesis is structured to answer the following major research questions:

1. **What is the magnitude of the AVHRR LTDR uncertainties and how are they distributed in time and space?**

   For this study, globally distributed surface reflectance data from Landsat-5 Thematic Mapper 5 (TM5) generated by the United States Geological Survey (USGS) is used as a well-calibrated reference. The evaluation is carried out using a methodology that accounts for directional effects using the Vermote-Justice-Breon (VJB) BRDF normalization method, and for spectral differences using spectral adjustment factors derived from EO-1/Hyperion hyperspectral data. The AVHRR record performance is reported in terms of the accuracy, precision, and uncertainty metrics. This work is presented in Chapter 2: "Evaluation of the AVHRR Surface Reflectance LTDR", which provides the first global comprehensive evaluation of the AVHRR surface reflectance LTDR during the period 1984-2011.

2. **What are the uncertainties associated to estimating water vapor globally from multiple AVHRR instruments in the absence of specific water vapor retrieval bands?**

To this end, this study uses near simultaneous observations of AVHRR N19 brightness temperature difference and MODIS Aqua integrated water vapor content to derive per-pixel split-window coefficients globally. Spectral adjustment factors are used to adjust the brightness temperature difference from the rest of the LTDR AVHRR instruments to N19 spectral characteristics and derive water vapor on a per-pixel basis. The AVHRR-derived water vapor is evaluated against water vapor estimates from sunphotometer observations of the Aerosol Robotic Network (AERONET) and against water vapor content estimated from MODIS Aqua Near-Infrared bands. Finally, the AVHRR-derived water vapor is evaluated in terms of the atmospheric correction process. This work is developed in Chapter 3: "Global estimation of water vapor from AVHRR", which presents a method to estimate atmospheric water vapor content from AVHRR thermal data.

3. **What effect do calibration discrepancies between multiple AVHRR sensors have on the LTDR record?**

In this study, a novel method for the automatized selection of pseudo-stable areas is proposed. The method uses the temporal profile of the ratio between the Red and NIR surface reflectance to search for pseudo-stable areas around the globe that are suitable for the AVHRR recalibration. Once these areas

are selected, the climatological mean for each band is computed from MODIS Aqua data and used as a stable reference to recalibrate the surface reflectance record. This work is presented as Chapter 4: "Recalibration of the AVHRR Long-Term Data Record", which attempts to mitigate calibration discrepancies between AVHRR instruments in the LTDR.

The final chapter of the thesis, entitled "Discussion and Conclusions", summarizes the findings of the previous chapters and puts them into context of the AVHRR LTDR project evolution. In addition, Chapter 5 gives insight of ongoing work and future evolution of the LTDR.

Chapter 2:   Evaluation of the AVHRR Surface Reflectance LTDR[1]

2.1   Abstract

Due to the length of the AVHRR surface reflectance LTDR and previous un-availability of a well calibrated reference, no comprehensive evaluation of the entire record has been reported so far. Recently, the United States Geological Survey (USGS) began production of surface reflectance datasets from the Landsat 4-8 satellites, which provide a suitable reference against which the LTDR can be compared to. In this chapter, we evaluate the LTDR between 1984 and 2011 using surface reflectance data from the Landsat-5 Thematic Mapper (TM5) Collection-1 as a reference. Data from TM5 was obtained from over 740,000 globally distributed scenes which gave a representative set of land surface types and atmospheric conditions. Differences due to observation geometry were accounted for using the Vermote-Justice-Breon (VJB) Bidirectional Reflectance Distribution Function (BRDF) normalization method to adjust the AVHRR surface reflectance to TM5 observation conditions; the spectral response differences were minimized using spectral band adjustment factors (SBAFs) derived from the Earth Observing One (EO-1) Hyperion

atmospherically corrected hyperspectral spectra. The performance of the AVHRR record is reported in terms of the accuracy, precision, and uncertainty (APU). Results show that the LTDR performance is close or within the combined uncertainty specification of $0.071\rho+0.0071$, where ρ is the estimated reflectance.

2.2   Introduction

The long-term data record (LTDR) from the Advanced Very High-Resolution Radiometer (AVHRR) provides daily surface reflectance with global coverage from the 1980s to present day, which makes it at invaluable source of information for the study of land surface properties and their long-term dynamics. Surface reflectance is a critical input for the generation of products such as vegetation indices, albedo, and land cover. Therefore, quality of the surface reflectance record should be the highest possible, and the assessment of its uncertainties is crucial to understand the record's potential and limitations, and how the uncertainties might propagate to downstream products.

Nowadays, data from MODIS is routinely used to evaluate the surface reflectance performance of the most recent AVHRR sensors [8]. While MODIS provides a well calibrated reference dataset, with daily global coverage, a robust atmospheric correction, and uncertainties lower than $0.05\rho + 0.005$ (where ρ is the surface reflectance), its data is only available since 2000 for Terra and 2002 for Aqua, which leaves over 19 years of record without a consistent surface reflectance reference.

In recent years, the United States Geological Survey (USGS) began production of surface reflectance products[2] from Landsat 4, 5, 7, and 8 [43–45], providing a long-term 16-day dataset at 30m spatial resolution. Data from the Landsat-5 Thematic Mapper (TM5) sensor spans a period of over 27 years, which covers most of the LTDR record lifetime. While it was initially shown that the internal calibration (IC) system of TM5 was not particularly stable [46], the bands calibration has been routinely updated based on the detectors response to the IC, the continuous observation of pseudo-invariant sites, and the cross-calibration with Landsat-7 ETM+ [46–48]. These efforts have achieved a radiometric calibration uncertainty of 7% for the at-sensor radiance [49].

The surface reflectance product provided by USGS is generated using the Landsat Ecosystem Disturbance Adaptive Processing System (LEDAPS) [44]. LEDAPS processing involves the calibration of images using revised coefficients and the atmospheric correction based on the 6S radiative transfer code. Performance of the LEDAPS TM5 surface reflectance product was shown to be better than specification of $0.071\rho + 0.0071$ in terms of surface reflectance uncertainty [50]. This record provides a unique opportunity for cross-comparison and evaluation of the AVHRR surface reflectance LTDR.

This chapter aims to design and conduct the first comprehensive evaluation of the AVHRR surface reflectance LTDR. For this, we use globally distributed LEDAPS TM5 surface reflectance data between 1984-2011 as a well-calibrated reference. The evaluation methodology accounts for directional effects using the VJB

---

[2]https://usgs.gov/land-resources/nli/landsat/landsat-collection-1-surface-reflectance

method, and for spectral differences using spectral adjustment factors derived from EO-1/Hyperion hyperspectral data. The AVHRR record performance is reported in terms of the accuracy, precision, and uncertainty metrics (APU) [28], which are evaluated in terms of their dependence to surface reflectance magnitude, temporal evolution, seasonality, spatial distribution, and land cover. Section 2.3 describes the data and materials used in this chapter. Section 2.4 presents the methodology. Section 2.5 presents the results and section 2.6 their discussion. Finally, section 2.7 gives the chapter conclusions.

2.3   Data

2.3.1   AVHRR Surface Reflectance

In this study, we evaluated the AVHRR surface reflectance Long Term Data Record (LTDR) [8], which is generated from Global Area Coverage AVHRR L1b data. The LTDR spans the period between 1981 to the present day and provides daily BRDF-normalized observations at spatial resolution of 0.05°x0.05° in the Climate Modeling Grid (CMG). The surface reflectance product includes information for 5 spectral channels, solar and view zenith angles, relative azimuth angles, and quality assessment. For this study, we use surface reflectance from the red (0.58-0.68 µm) and near infrared (0.72-1.10 µm) channels, the solar zenith, view zenith, and relative azimuth angles, and the quality layer, which was used to remove pixels contaminated by clouds or other atmospheric effects and analyze only those with the highest quality. The AVHRR surface reflectance products were obtained from

the LTDR project website[3].

2.3.2 Landsat-5 TM Surface Reflectance

Surface reflectance from the Landsat-5 Thematic Mapper sensor (TM5) was used as a reference to evaluate the AVHRR record. TM5 acquired images between 1984 and 2012, making it the longest operating Earth observation satellite. Data from TM5 has a temporal resolution of 16 days and a spatial resolution of 30m. We used data from over 740,000 scenes of surface reflectance generated by LEDAPS [44] from terrain corrected L1TP top-of-atmosphere products (Collection-1, Tier-1). The spatial distribution of scenes is shown in Figure 2.1, and the temporal distribution of scenes is shown in Figure 2.2. The method for scene selection is explained in 2.4.1. For this study, we use surface reflectance from the red (0.63-0.69 µm) and near infrared (0.76-0.90 µm) channels, and quality information from the pixel quality, radiometric saturation, and atmospheric opacity layers. Evaluation of the TM5 LEDAPS surface reflectance found that it performed better than $0.071\rho+0.0071$ [50]. The TM-5 Collection-1 Tier-1 surface reflectance products were downloaded from Google Earth Engine[4].

---

[3]https://ltdr.modaps.eosdis.nasa.gov
[4]https://developers.google.com/earth-engine/datasets/catalog/LANDSAT_LT05_C01_T1_SR
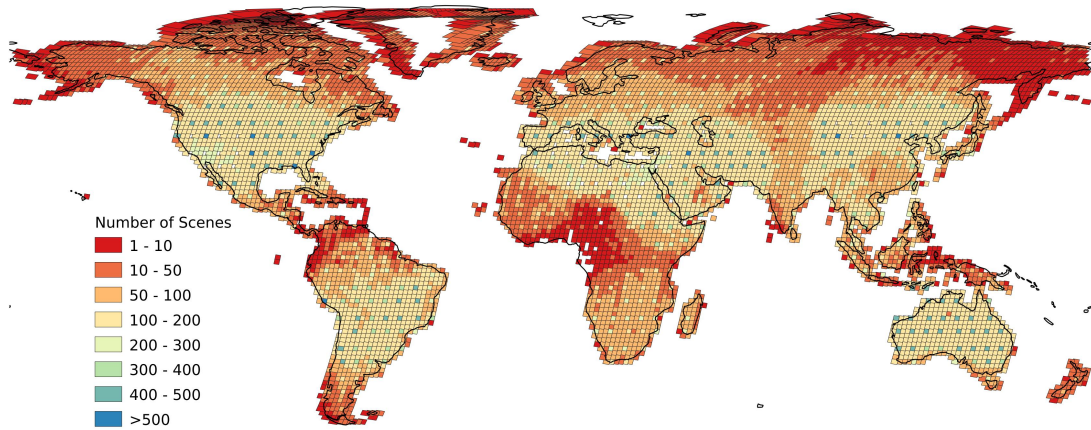
Figure 2.1: Global distribution of Landsat-5 TM scenes used for evaluation.
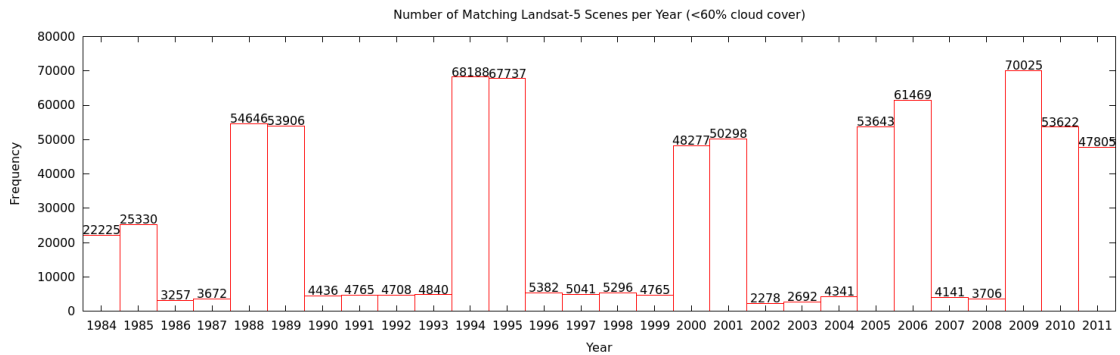
Figure 2.2: Number of matching Landsat-5 TM scenes per year.

2.3.3 Landsat-5 TM per-pixel angles

The TM5 surface reflectance product metadata provides information on the sun elevation and azimuth angles for the center of the scene but gives no information on the observation zenith and azimuth angles. With the purpose of having a better description of the solar and observation geometric characteristics of each scene, we computed the per-pixel solar zenith, solar azimuth, view zenith, and view azimuth angles using routines made available by USGS[5]. These routines read an angle coeffi-

---

[5]https://usgs.gov/land-resources/nli/landsat/solar-illumination-and-sensor-viewing-angle-coefficient-files

cient file unique to each scene and processes it using the Landsat Image Assessment System Geometric Libraries [51].

2.3.4 MODIS Land Cover Data

To analyze our results by land cover types we followed the International Geosphere-Biosphere Program (IGBP) classification included on MODIS product MCD12C1 [52]). The MCD12C1 product provides yearly global land cover information in the CMG grid from 2001 to present year. To reduce possible misclassification on years before the MODIS era, we generated a single classification map from all available years by selecting only the pixels that remained constant during the entire period. The original IGBP classes were then simplified following an approach similar to [53]. Water areas were excluded from the analysis, and urban, snow, and wetland classes were removed because they had low pixel counts or were not present at all. The class reclassification scheme is showed in Table 2.1, and the global distribution of classes is shown in Figure 2.3.

Abbreviation	New Class Name	Original IGBP Classes
NLF	Needleleaf Forest	Evergreen Needleleaf Forest, Deciduous Needleleaf Forest
BLF	Broadleaf Forest	Evergreen Broadleaf Forest, Deciduous Broadleaf Forest
SSM	Shrublands, Savannas, Mixed Forest	Open Shrubland, Closed Shrubland, Savannas, Woody Savannas, Mixed Forest
CGL	Croplands and Grasslands	Croplands, Grasslands, Cropland Natural Vegetation Mosaic
BRN	Bare Areas	Barren

Table 2.1: Reclassification of IGBP land cover classes
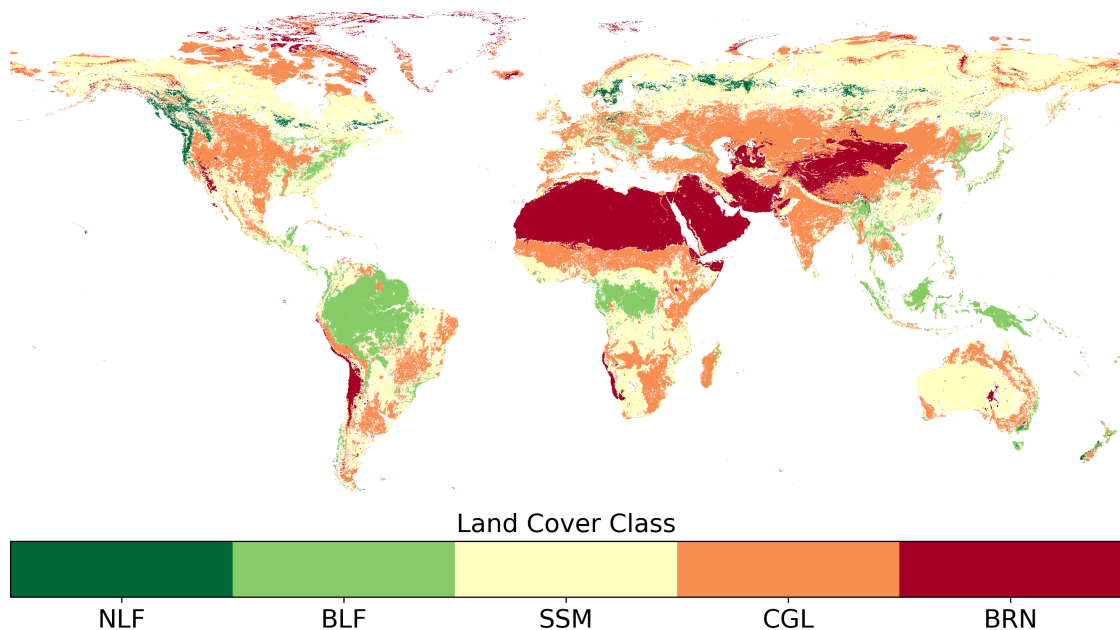
Figure 2.3: International Geosphere-Biosphere Program (IGBP) land cover classification from MODIS MCD12C1. Labels were simplified according to Table 2.1.

2.3.5 Hyperion Surface Reflectance Spectra

In this study, spectral band adjustment factors (SBAF) between AVHRR and TM5 were derived from a set of more than 100,000 hyperspectral surface reflectance spectra acquired by the Hyperion (H0) spectrometer onboard the Earth Observer-1 (EO-1) satellite. Hyperion is a hyperspectral imager that acquires data from 198 calibrated bands in the range of 400 to 2500nm with a 10 nm spectral resolution and 30 m spatial resolution [54]. For the purpose of deriving SBAFs over a wide range of conditions, data from two readily available surface reflectance data sets collected over Australia between 2001 and 2010 [55] and the Amazon rainforest between 2002 and 2005 [56] were used. In total, 152 H0 granules were included for the derivation of SBAF, with most of the data coming from the Australian dataset (133 granules

versus 19 from the Amazon dataset). The spectra were sampled from the middle of the images, in the center of the swath. Although the spectra came from surface reflectance products, still some of them had to be manually removed as they showed traces of water vapor absorption (evidenced by plotting the spectra and observing the 940nm band), were noisy, or did not report values. After filtering, the number of H0 spectra considered from each dataset was 54,333 from Australia, and 53,677 from the Amazon.

2.3.6 Relative Spectral Responses

Relative spectral responses (RSR) from AVHRR and TM5 were used to spectrally convolve the H0 surface reflectance spectra and derive spectral adjustment factors. Figure 2.4 shows the RSR for each AVHRR sensor considered (N07 to N19), and for TM5. The RSR were obtained from the NASA Langley cloud and radiation research webpage[6].

2.4 Method

2.4.1 Selection of reference Landsat-5 TM dataset

The Landsat-5 scenes used as reference for this study were selected with the objective of maintaining a high spatial and temporal representativeness. This was achieved in two steps: First, we generated a global 5° latitude-longitude uniform grid of points and selected all Landsat-5 scenes that intersected a point for the

---

[6]https://cloudsway2.larc.nasa.gov
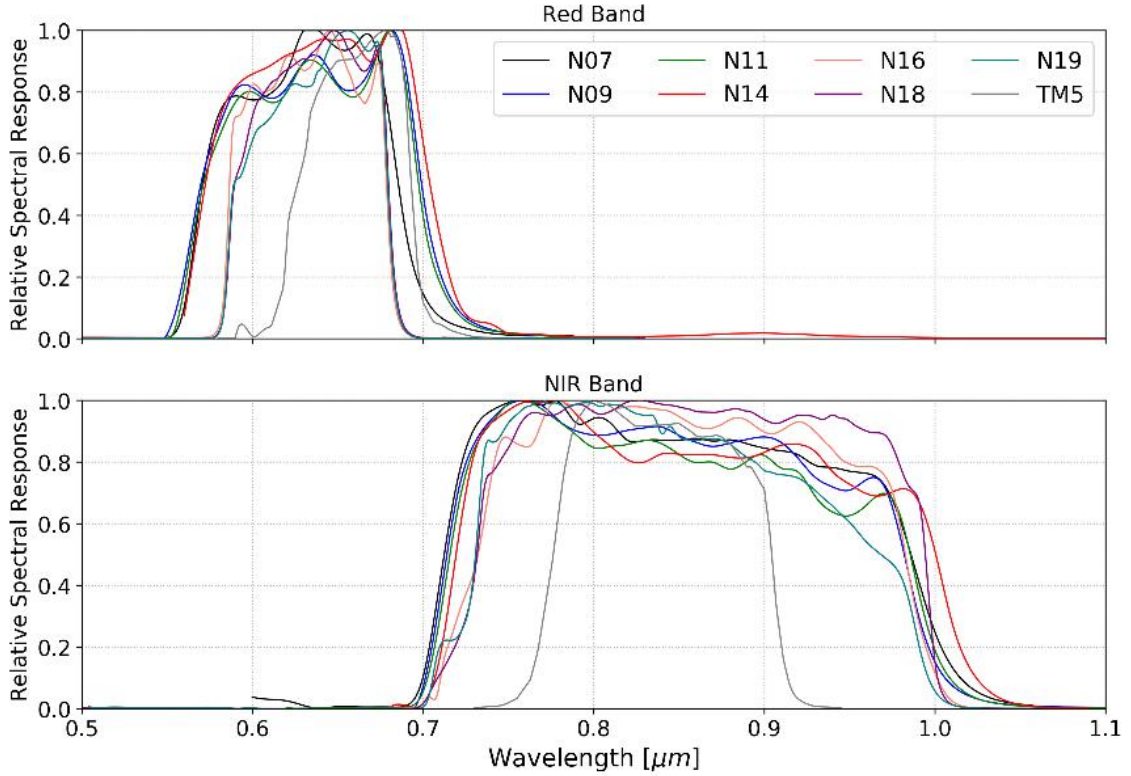
Figure 2.4: AVHRR and TM5 Relative Spectral Responses.

entire period of study. Second, for the first and last year of each POES satellite, we selected all globally available scenes. In both cases, we discarded the scenes that had more than 60% of cloud cover over land. This process generated a database of more than 740,000 globally distributed scenes (Figures 2.1 & 2.2). Finally, for all remaining scenes we downloaded a 120kmx120km subset located on the center of each image.

2.4.2 Spatial aggregation of Landsat 5 TM surface reflectance

The first step in the evaluation was to aggregate the 30m TM5 surface reflectance pixels to the scale of the AVHRR climate modeling grid (CMG) of 0.05°x0.05°.

For this, we first selected the valid TM5 pixels following the criteria proposed by [50]: clear land pixels (with no cloud, cloud-shadow, water, or snow), that show no saturation, and with an atmospheric opacity lower than 0.3. Once the valid pixels were selected, we aggregated them to CMG scale using an averaging filter. Finally, we discarded all aggregated pixels generated from less than 100% valid TM5 pixels.

2.4.3   Geometric adjustment of AVHRR surface reflectance

The AVHRR LTDR product is originally normalized to a sun zenith angle (θ_s) of 45°; view zenith angle (θ_v) of 0°; and relative azimuth angle (ϕ) of 0°. To analyze the impact of BRDF on the LTDR performance, we started by undoing the current normalization in order to have a baseline dataset with no geometric or spectral adjustment whatsoever. We refer to this dataset as "No adjustment" in the rest of the manuscript. It is important to remark that comparing reflectance data from different sensors without accounting for BRDF effects should be avoided, as different geometric configurations can produce different errors that depend on both sensors sun-view geometries and on the observed surface characteristics. We then used the VJB method [17] explained on section 1.2.3 to account for observation geometry differences between AVHRR and Landsat-5 by adjusting the AVHRR surface reflectance to the corresponding Landsat-5 sun and view angles.

Following the relationship described in Equation 1.7, the same-day AVHRR surface reflectance can be adjusted to the corresponding TM5 observation geometry

26

as:

$$\rho AVHRR(\Theta_{TM5}) = \rho AVHRR(\Theta_{AVHRR}) \frac{(1 + VF_{vol}(\Theta_{TM5}) + RF_{geo}(\Theta_{TM5}))}{(1 + VF_{vol}(\Theta_{AVHRR}) + RF_{geo}(\Theta_{AVHRR}))}$$

(2.1)

For this study, the AVHRR angles were obtained directly from the LTDR product, and the TM5 angles were computed as described in subsection 2.3.3.

2.4.4 Spectral adjustment of AVHRR surface reflectance

Relative spectral responses (RSR) determine how a continuous spectrum from the surface is recorded on a sensor discrete band. Thus, differences in RSR between AVHRR and TM5 can affect the results of the cross-comparison, and a spectral adjustment should be applied to mitigate this [57]. Amongst spectral adjustment methods the statistical based ones are the most common [6]. These methods consist in deriving statistical relationships between two analogous bands using radiative transfer simulations [41, 58], remotely sensed data [41, 59], or hyperspectral spectra convolutions [60, 61]. For this study, we derived the spectral adjustment factors using the latter method. We first extracted over 100,000 H0 atmospherically corrected reflectance spectra from two readily available datasets (more information is given in 2.3.5). Because the spectral mixture inside an AVHRR CMG pixel (5600m) is typically more diverse than that of a Hyperion pixel (30m), we followed the approach proposed by [6], and simulated a dataset of 500,000 surface reflectance spectra from the linear combination of up to three independent H0 spectra. This provided a spectra database more representative of the CMG pixels scale. The

27

generated spectra were convolved with each sensor RSR as shown in Equation 2.2, where λ represents the Red or NIR band.

$$\bar{\rho}_\lambda = \frac{\int \rho_\lambda RSR_\lambda d_\lambda}{\int RSR_\lambda d_\lambda} \tag{2.2}$$

The convolved values were used to derive spectral band adjustment factors (SBAF) for each TM5/AVHRR pair as:

$$SBAF_\lambda = \frac{\bar{\rho}_{\lambda,TM5}}{\bar{\rho}_{\lambda,AVHRR}} \tag{2.3}$$

We tested several spectral adjustment models [6] and found that the best fit was obtained by fitting the SBAFs to the quadratic NDVI:

$$SBAF_\lambda = a_\lambda + b \cdot \lambda NDVI_{AVHRR} + c \cdot \lambda NDVI^2_{AVHRR} \tag{2.4}$$

Finally, the derived coefficients are used to spectrally adjust the AVHRR to TM5-like values as:

$$\rho_{\lambda,TM5} = \rho_{\lambda,AVHRR} \cdot SBAF_\lambda \tag{2.5}$$

2.4.5   Evaluation of Surface Reflectance

For the evaluation we assumed no daily variation of the surfaces and relied on same day AVHRR and TM5 acquisitions. We only considered AVHRR observations with a sun zenith angle smaller than 75° and view zenith angle smaller than 45°. Finally, we used the Local Outlier Factor method to remove any remaining outliers

[62]. We evaluate the differences between AVHRR and TM5 using three statistical metrics designed to quantify the accuracy, precision, and uncertainty (APU). The accuracy (A) represents the mean bias of the estimates versus the reference (ϵ_i):

$$Accuracy\ (A) = \frac{\sum_{i=1}^{n} \epsilon_i}{N} \tag{2.6}$$

The precision (P) represents the repeatability of the estimates corrected for the mean bias:

$$Precision\ (P) = \sqrt{\frac{1}{N-1} \sum_{i=1}^{n} (\epsilon_i - A)^2} \tag{2.7}$$

The uncertainty (U) represents the actual statistical deviation including the mean bias:

$$Uncertainty\ (U) = \sqrt{\frac{1}{N} \sum_{i-1}^{N} \epsilon_i^2} \tag{2.8}$$

To provide a better perspective of each band performance, it is helpful to show the uncertainty relative to the average reference value (m). The relative uncertainty (rU) is then computed as:

$$Relative\ Uncertainty\ (rU) = \frac{U}{m} \tag{2.9}$$

In this chapter, A, P, and U follow the definitions from [28]. Thus, higher values reflect larger discrepancies between both datasets and lower values reflect a better agreement.

To assess the evaluation results, we compare the uncertainty values against a certain specification (S). For surface reflectance products, this specification is based on a sensitivity analysis of the atmospheric correction method, which for both AVHRR LTDR and TM5 LEDAPS is based on the 6S model and has been previously found to be $0.05\rho+0.005$ (where ρ is the surface reflectance magnitude) [28, 29]. Because in this study we evaluate AVHRR using TM-5 as a reference, the evaluation specification is then defined as the quadratic sum of each sensor's specification, which for this case is $0.071\rho+0.0071$. This approach has been adopted by other surface reflectance evaluation and intercomparison studies [50, 59].

2.5 Results

In this section we present the results from the AVHRR evaluation. First, we show the impact of the BRDF and spectral adjustment on the comparison between AVHRR and TM5 surface reflectance 2.5.1; we then show the evaluation results in terms of the surface reflectance magnitude 2.5.2, temporal evolution 2.5.3, seasonal variation 2.5.5, spatial distribution 2.5.4, and land cover 2.5.6.

2.5.1 Impact of geometric and spectral adjustment

We first analyzed the impact of the geometric and spectral adjustment on the accuracy, precision, and uncertainty. Figure 2.5 shows the comparison between AVHRR and TM5 surface reflectance for four adjustment levels: No Adjustment, only BRDF adjustment, only spectral adjustment, and with both adjustments.
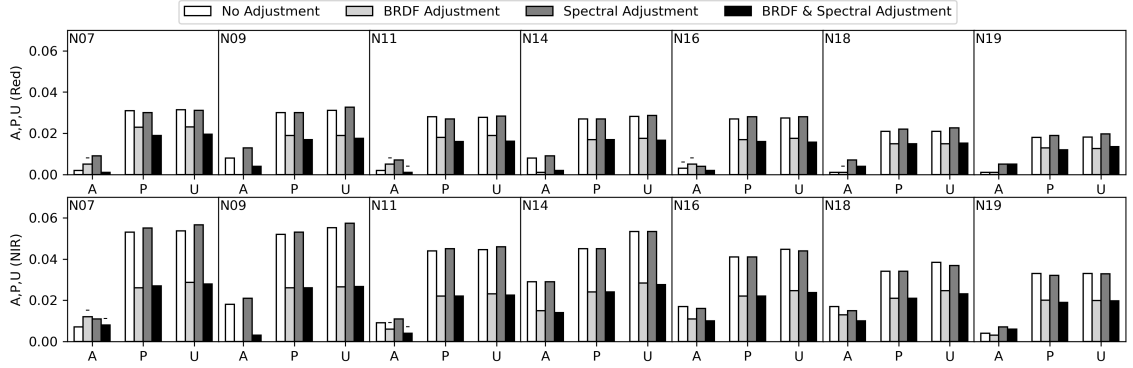
Figure 2.5: Impact of the geometrical and spectral adjustments on the accuracy (A), precision (P), and uncertainty (U). Results are shown for the Red (top row) and NIR (bottom row) bands. A "-" sign above the accuracy bars indicates negative values. Lower values show better agreement between AVHRR and Landsat-5 TM.

The BRDF adjustment improved the results on all the metrics for both bands. In particular, the improvements were more evident on the Precision metric, which represents the scattering of the errors between AVHRR and TM5 and is mainly affected by differences in their sun-view geometry. The accuracy metric also showed improvements with BRDF correction but were not as consistent across all sensors.

When the spectral adjustment was applied to the not-BRDF adjusted data, the results tended to show worse agreement between AVHRR and TM5, with only minor improvements in the best of cases. In general, the best results for accuracy, precision and uncertainty were achieved when both adjustments were applied to the AVHRR data.

For all cases, the Red band showed lower uncertainty values than the NIR. However, because the surface reflectance magnitudes on the NIR are usually higher, its relative uncertainties were lower. Table 2.2 summarizes the relative uncertainty results for the case with no adjustment and with both BRDF and spectral adjust-

ments.

Band / Adjustment	N07	N09	N11	N14	N16	N18	N19
Red / No Adjustment	23%	22%	19%	18%	18%	17%	17%
Red / BRDF + Spectral	14%	13%	11%	11%	10%	12%	13%
NIR / No Adjustment	20%	21%	17%	20%	17%	16%	14%
NIR / BRDF + Spectral	10%	10%	9%	10%	9%	10%	8%

Table 2.2: Relative uncertainty before and after BRDF and spectral adjustment

2.5.2 Performance of LTDR in terms of reflectance magnitude

Performance of surface reflectance products varies with the reflectance magnitude of the measured target. Here we present this dependence using APU graphs (Vermote and Kotchenova, 2008), which represent the accuracy, precision, and uncertainty for a range of reference reflectance values. Figure 2.6 shows APU graphs of the evaluation for each sensor and band using both the geometric and spectral adjustments. For most sensor-band combinations, the uncertainty increased with surface reflectance magnitude but remained under the combined specification $(0.071\rho + 0.0071)$. For the Red band, average values ranged between -0.001 to 0.005 for the accuracy, 0.012 to 0.019 for the precision, and 0.014 to 0.020 for the uncertainty. In the case of the NIR band, the average values ranged between -0.008 to 0.014 for the accuracy, 0.019 to 0.027 for the precision, and 0.020 to 0.028 for the uncertainty. Overall, data from KLM (N16 to N19) sensors showed better performance than pre-KLM ones (N07 to N14).
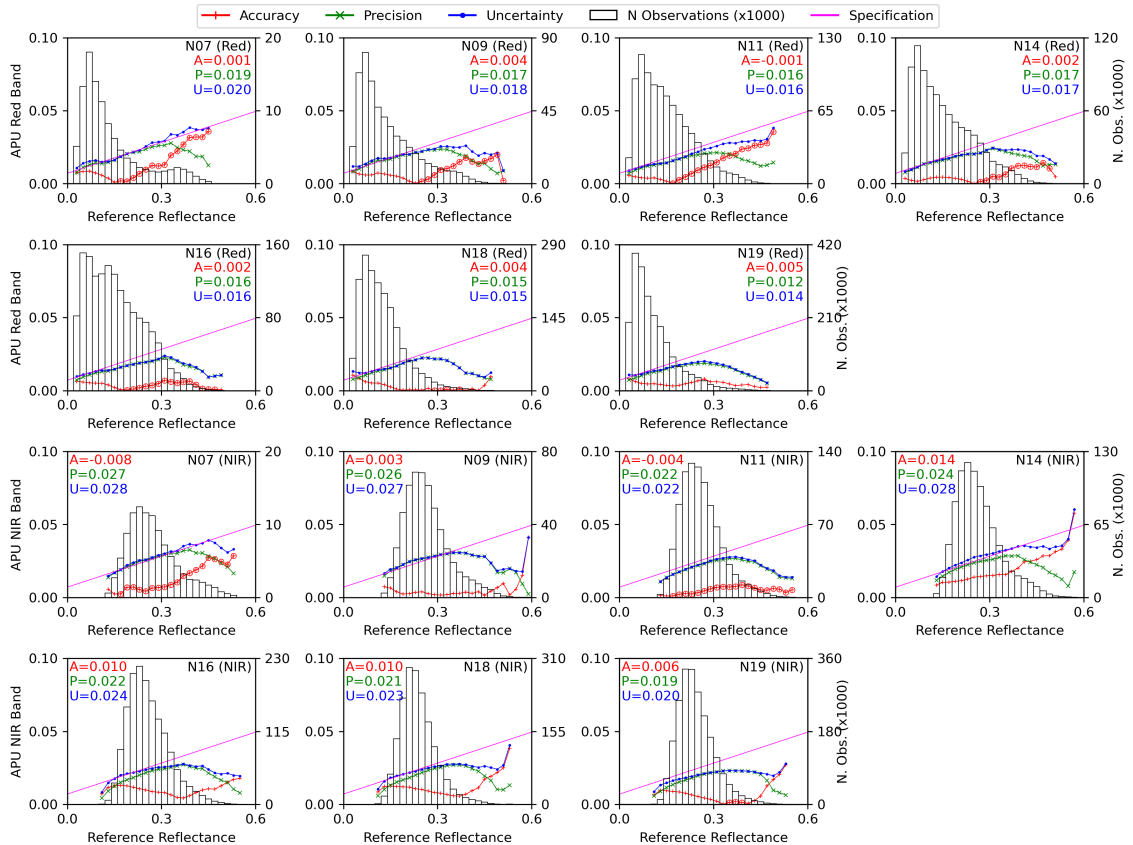
Figure 2.6: Accuracy (A), Precision (P), and Uncertainty (U) of AVHRR surface reflectance evaluation. Metrics are computed in bins of 0.02 reflectance units and the overall value is given in the top of each subplot. The histogram of values is displayed in black (right axis). Circles on the accuracy line represent negative values. The magenta line represents the specification of $0.071\rho + 0.0071$ from the TM5 product.

2.5.3 Temporal evolution of LTDR performance

Performance of a satellite data record can change in time, as changes in platform orbit, sensor degradation, and data calibration can affect the quality of top-of-atmosphere data. Moreover, performance of the atmospheric correction process depends on the quality of available ancillary data used to characterize atmospheric conditions. In this regard, it is important to evaluate how the performance of the AVHRR LTDR changes with time. Figure 2.7 shows the temporal evolution of the

APU metrics during the 1984-2011 study period. Yearly results are shown for each sensor-band combination for the geometrical and spectrally adjusted AVHRR data. Accuracies showed a generally consistent behavior for each independent sensor, i.e., in most cases a particular AVHRR sensor showed either negative or positive bias with respect to TM5. One exception was N11 NIR band, which exhibited variations in the bias direction during its lifetime and an opposite bias behavior both when transitioning from its predecessor (N11) and to its successor (N14). In terms of precision, the pre-KLM sensors (N07-N014) showed an increasing trend of the P metric during their lifetimes that was present in both bands. This was not the case for the KLM sensors (N16-N19) which showed a more stable temporal behavior.
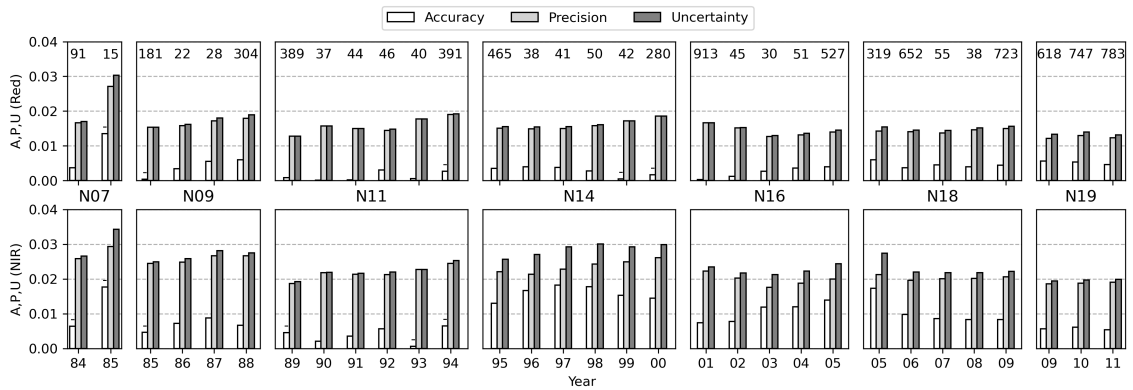
Figure 2.7: Temporal evolution of the Accuracy, Precision, and Uncertainty. A "-" sign above the accuracy bar represents negative values. The number of CMG pixels (in thousands) is shown at the top.

2.5.4 Spatial distribution of bias and relative uncertainty

Performance of the LTDR is not spatially uniform. Two metrics helpful to represent this are the accuracy, which shows the mean bias of AVHRR with respect

to TM5; and the relative uncertainty, which gives context to the uncertainty metric in relation to the actual average reflectance of a particular site. We display these metrics in 2.5° latitude and longitude bins that provide enough data to compute the statistical metrics. For each bin, the metrics were computed from all included CMG pixels. Wider spatial coverage in the results of newer AVHRR sensors is due to a larger number of TM5 scenes available and is not related with AVHRR data availability. Accuracy results showed lower biases for the Red than for the NIR band (Figure 2.8). The Red band accuracy values for 95% of bins varied within -0.028 to 0.026 for N07, -0.015 to 0.018 for N09, -0.021 to 0.013 for N11, -0.012 to 0.014 for N14, -0.008 to 0.012 for N16, -0.005 to 0.015 for N18, and -0.003 to 0.015 for N19. For the NIR band, accuracy values for 95% of the bins varied within -0.040 to 0.017 for N07, -0.025 to 0.025 for N09, -0.026 to 0.014 for N11, -0.008 to 0.034 for N14, -0.008 to 0.023 for N16, -0.006 to 0.022 for N18, and -0.001 to 0.018 for N19. There is a change in the bias direction and magnitude (sign of the accuracy value) on the NIR band when transitioning from N11 to N14 which is especially noticeable on Northern Africa and Western Asia.

N07 Red

N07 NIR

N09 Red

N09 NIR

N11 Red

N11 NIR

N14 Red

N14 NIR

N16 Red

N16 NIR

N18 Red

N18 NIR
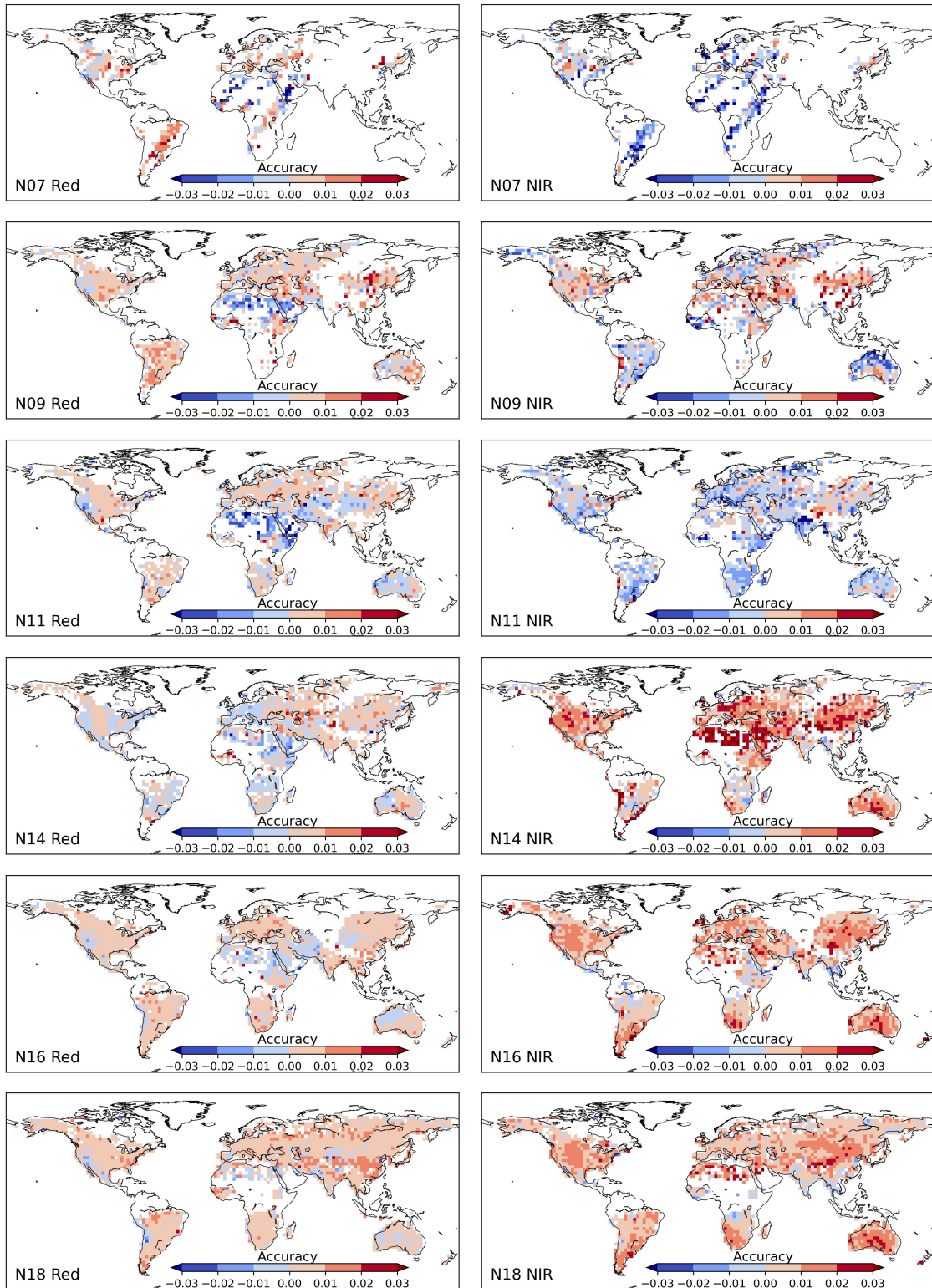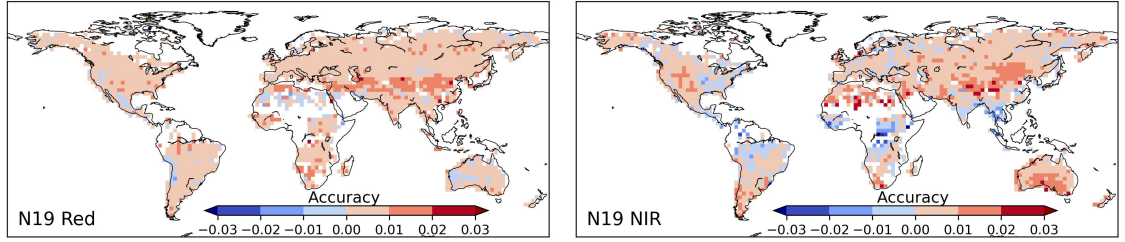
Figure 2.8: Accuracy maps for AVHRR LTDR Red and NIR bands. Values closer to 0 represent better performance. The values were computed in 2.5° (latitude and longitude) bins considering all corresponding CMG pixels.

The spatial distribution of relative uncertainties was generally consistent between all sensors (Figure 2.9). The highest relative uncertainties were observed over high latitudes and over tropical regions. In particular, the largest values were observed over the Amazon forest, where the density of observation is low due to frequent cloud cover. The Red band showed worse performance than the NIR. When considering 95% of the bins, the global relative uncertainty average values for the Red band were (15±6)% for N07, (14±6)% for N09, (13±4)% for N11, (13±4)% for N14, (14±6)% for N16, (16±6)% for N18, and (15±6)% for N19. In the NIR band, the values were (10±3)% for N07, (10±2)% for N09, (9±2)% for N11, (10±2)% for N14, (9±2)% for N16, (9±2)% for N18, and (8±2)% for N19. On the next sections, we analyze these results in terms of seasonality and land cover class.
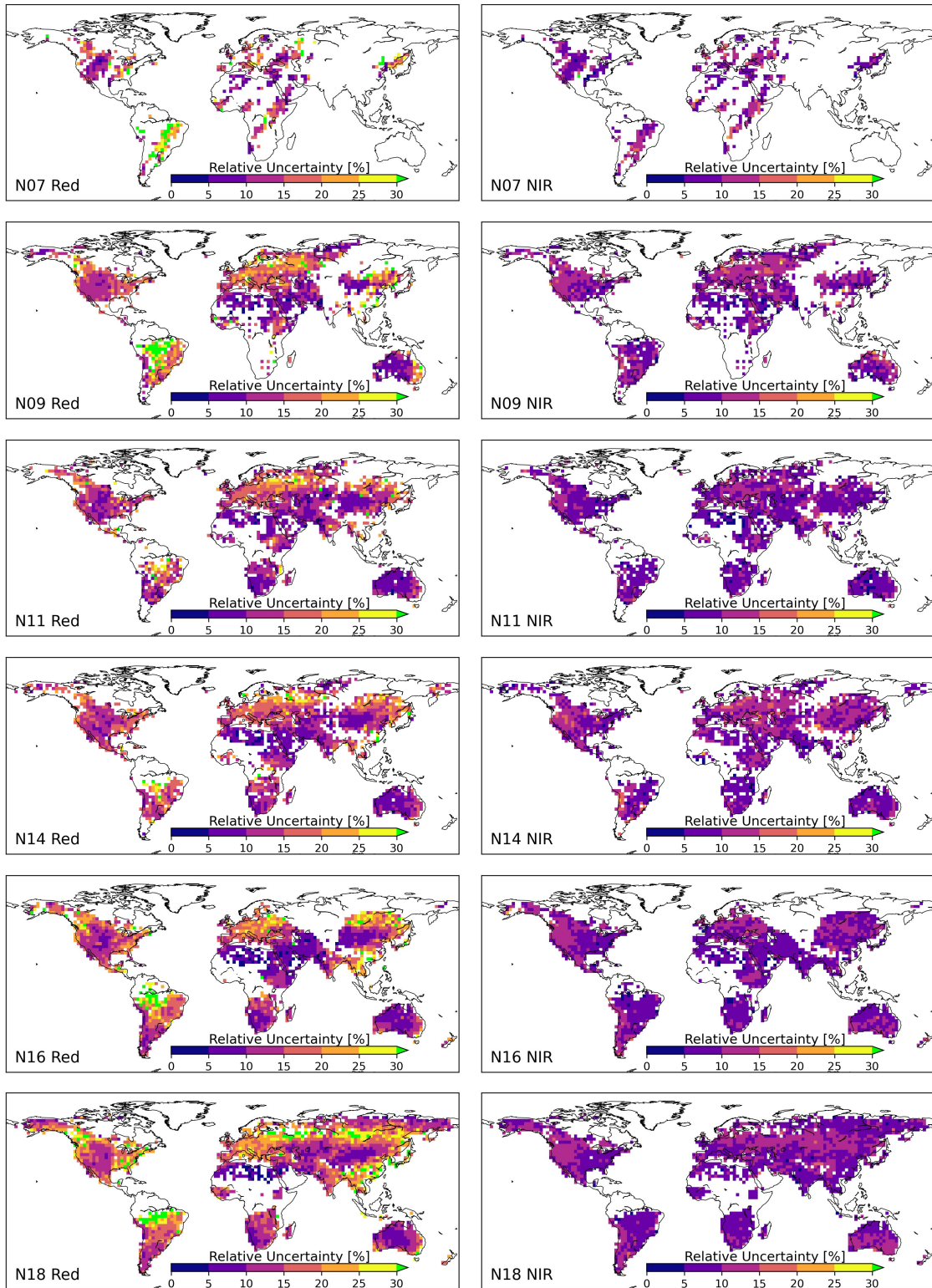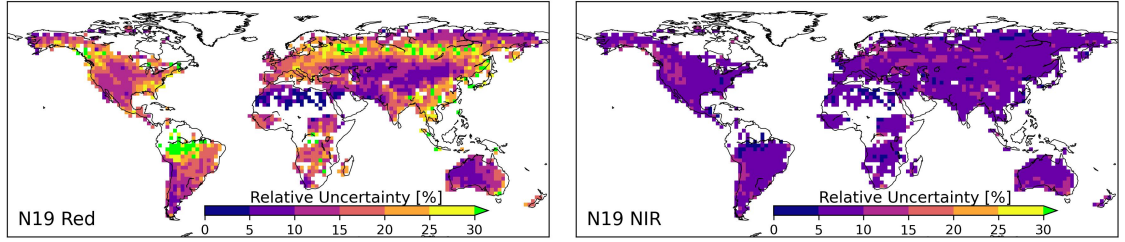
Figure 2.9: Relative uncertainty maps for AVHRR LTDR Red and NIR bands. Values closer to 0 represent better performance. The values were computed in 2.5° (latitude and longitude) bins considering all corresponding CMG pixels.

2.5.5 Seasonal variation of Accuracy and Relative Uncertainty

The seasonal variation of the Accuracy and Relative Uncertainty are shown in Figure 2.10. The metrics were first computed per pixel, and then aggregated by season and analyzed for the Northern (NH) and Southern (SH) hemispheres separately. Seasons correspond to December-January-February (DJF), March-April-May (MAM), June-July-August (JJA), and September-October-November (SON). Only pixels with more than 30 valid observations were considered in the analysis. The number of pixels per season, hemisphere, and satellite is shown in Table 2.3.

The number of pixels with more than 30 observations is, on average, around 4 times larger on the Northern hemisphere than in the Southern hemisphere, which is likely due to distribution of land bodies as well as TM5 data availability. On both hemispheres, the JJA season showed the highest number of observations available.

Average Red band accuracies ranged between -0.013±0.015 (N07 in DJF) to 0.007±0.006 (N18 in JJA) on the northern hemisphere, and between -0.024±0.017 (N07 in MAM) to 0.019±0.009 (N07 in JJA) on the southern hemisphere. Results for the NIR band showed average accuracies that ranged between -0.021±0.014 (N07

	Season							
	Northern Hemisphere				Southern Hemisphere			
Platform	DJF	MAM	JJA	SON	DJF	MAM	JJA	SON
N07	14527	14109	27725	19077	1695	862	7152	4631
N09	50760	98427	114798	97697	13442	20172	32442	21383
N11	66669	179228	219928	147291	17795	50791	96986	28075
N14	123343	166604	146475	182020	10230	42750	82012	29062
N16	142899	258199	323567	255178	32492	63199	175859	62986
N18	95938	171564	282999	415161	16426	118936	300556	94323
N19	129799	201134	522381	494477	24814	109541	184704	100931

Table 2.3: Number of CMG pixels per season

in DJF) to 0.015±0.012 (N14 in JJA) on the northern hemisphere, and between
-0.024±0.017 (N07 in MAM) to 0.019±0.009 (N07 in JJA) on the southern hemi-
sphere. For most cases, the spread of values was generally similar between the Red
and NIR bands. In terms of relative uncertainties, average values for the Red band
ranged between (10±5)% (N16 in DJF) to (20±8)% (N18 in JJA) on the northern
hemisphere, and between (10±5)% (N11 in JJA) to (37±13)% (N07 in MAM) in the
southern hemisphere. In the case of the NIR band, average values ranged between
(8±2)% (N19 in DJF) to (11±4)% (N07 in DJF) on the northern hemisphere, and
between (7±2) (N11 in JJA) to (13±6)% (N07 in MAM) in the southern hemisphere.
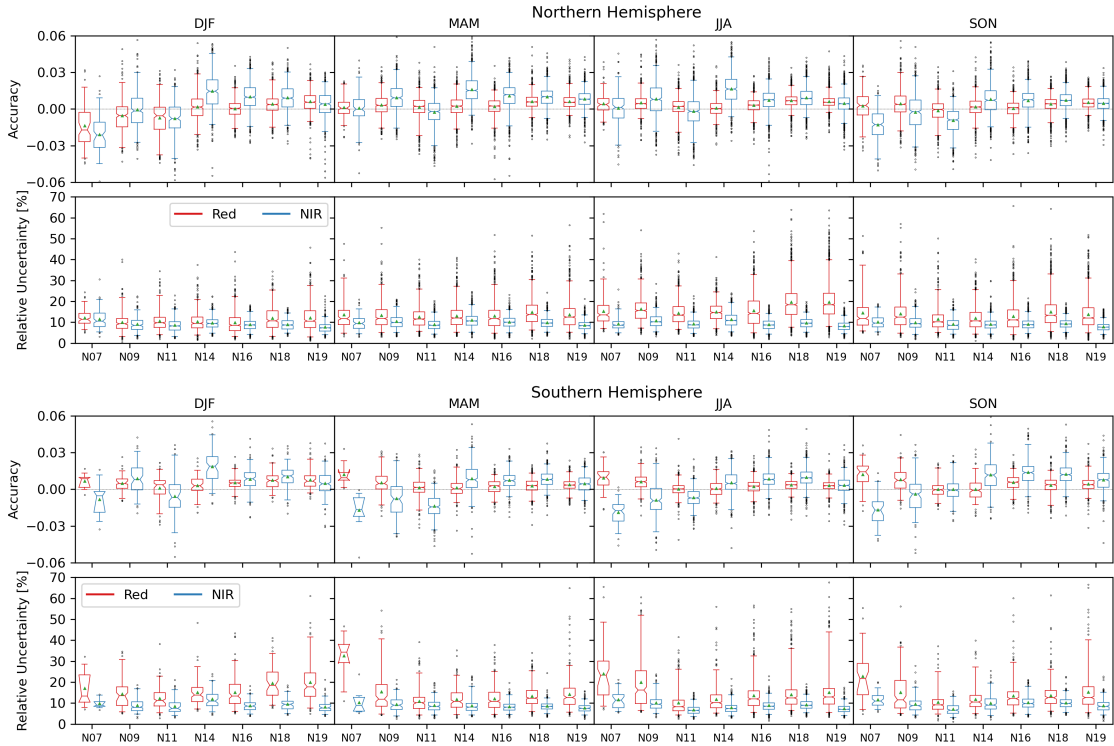
Figure 2.10: Seasonal variation of accuracy and relative uncertainty for Red and NIR bands on the northern (top) and southern (bottom) hemispheres. Boxplot notches represent the median confidence interval. Green triangles represent the mean. Values outside the 2.5th and 97.5th percentiles are plotted individually outside the boxplot whiskers.

2.5.6 Accuracy and Relative Uncertainty analysis by land cover

Accuracy and relative uncertainty aggregated by land cover class are shown in Figure 2.11. The land cover classes analyzed correspond to the ones shown in Table 1. The metrics were first computed per pixel, and then aggregated by land cover class. Only pixels with more than 30 valid observations were considered for the analysis. The number of pixels per land cover class for each POES satellite is shown in Table 2.4.

Average accuracy values for the Red and NIR bands showed little variation

Platform	Land Cover Class				
	NLF	BLF	SSM	CGL	BRN
N07	435	4674	18985	50202	15548
N09	2770	17543	120336	225264	82994
N11	2855	17168	204620	422263	159665
N14	1951	16295	189696	368736	205684
N16	12485	42271	372754	565779	320876
N18	11090	44301	557509	755103	127602
N19	21853	82534	649113	850797	162205

Table 2.4: Number of CMG pixels per land cover class

between sensors and land cover classes. Values ranged between -0.016±0.013 (N07 on BRN) to 0.012±0.005 (N18 on NLF) for the Red band, and between -0.014±0.015 (N07 on BRN) to 0.02±0.019 (N14 on NLF) for the NIR band. The newer sensors generally showed less variability within the same land cover. Overall, the largest spread of values was shown by the BRN class. In terms of relative uncertainties, results showed that for the Red band the largest uncertainties occurred on the Forest classes, which ranged between (19±9)% (N14 on BLF) to (34±14)% (N18 on NLF). In contrast, the BRN class showed the lowest relative uncertainties, ranging between (8±3)% (N16) to (10±4)% (N18). In the case of the NIR band, results were more consistent between land classes and sensors, and were noticeably lower than those of the Red band, ranging between (7±2)% (N19 on BLF) to (14±8%) (N14 on NLF).

2.5.7 Relationship between Red and NIR bands relative errors

Knowledge of possible correlation between the Red and NIR band errors can be of interest for downstream data producers and users. In this context, Figure 2.12 shows the spatial distribution of the determination coefficient (R^2) computed between the Red and NIR bands relative errors with data from all AVHRR sen-
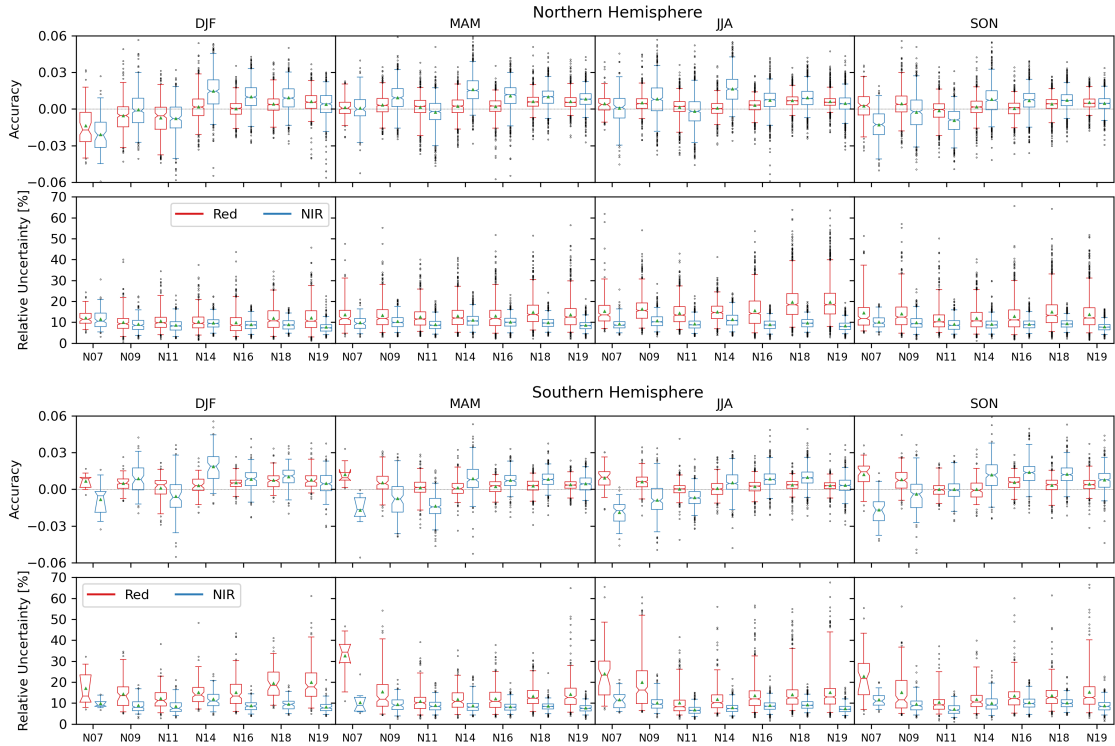
Figure 2.11: Accuracy (top) and relative uncertainty (bottom) results by land cover class for Red and NIR bands. Boxplot notches represent the median confidence interval. Green triangles represent the mean. Values outside the 2.5th and 97.5th percentiles are plotted individually outside the boxplot whiskers.

sors. Results showed a strong relationship between relative errors over bare areas in North Africa and Southern Asia ($R^2 > 0.8$), and over open shrubland areas in North America, South America, South Africa, and Australia ($R^2 > 0.5$). Similar results were obtained for each sensor independently but are excluded for brevity.

2.6 Discussion

In this chapter, we evaluated the performance of the AVHRR surface reflectance long-term data record between 1984 and 2011 using Landsat-5 TM surface reflectance as reference. While the current LTDR temporal coverage spans the pe-
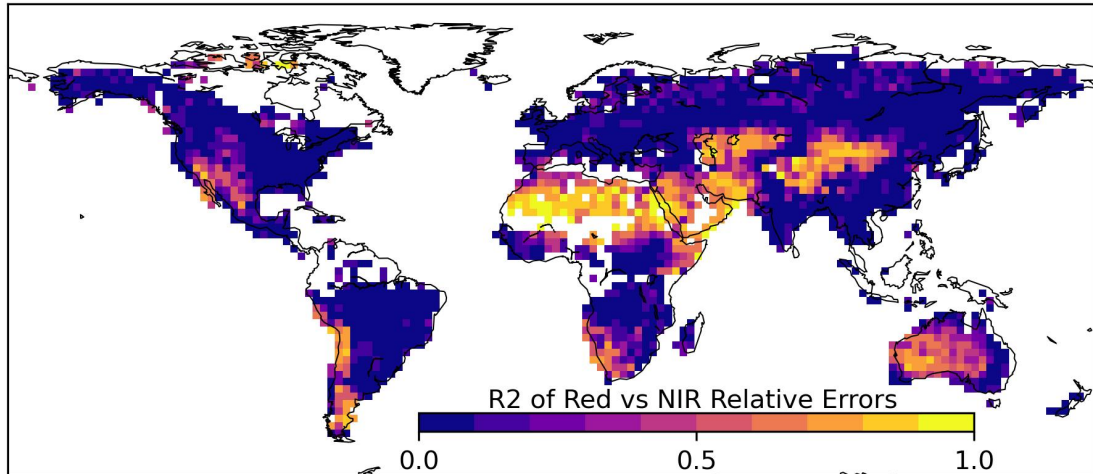
Figure 2.12: Determination coefficient between Red and NIR bands relative errors. The values were computed in 2.5° (latitude and longitude) bins considering all corresponding CMG pixels.

riod between 1982 to present day, we limited this study to the period where Landsat-5 was active. This allowed us to evaluate the performance of all AVHRR sensors with one consistent reference that has gone through a series of strict recalibration procedures [48].

The VJB method was used to normalize the AVHRR surface reflectance to the observation geometry of TM5, which largely improved the uncertainties between sensors, and is explained by the minimization of errors generated from the very different observation geometries. These results agree with previous studies [37, 38, 63, 64] that showed the good performance of the BRDF-adjustment obtained with the VJB method. For this study we used global V and R coefficients derived from MODIS and applied them to adjust AVHRR data, which are the same coefficients used to normalize the BRDF in the LTDR product.

Adjustment of spectral differences showed mixed performance. When applied

44

alone, only a couple of sensor-band combinations improved the agreement between AVHRR and TM5, and the general results showed an overcompensation and increase of bias. On the other hand, when the SBAFs were used to spectrally adjust the BRDF-normalized data, results improved as it further reduced the mean bias between AVHRR and TM5 for almost all cases. This might be explained by the dependence of the spectral adjustment factors on the NDVI, which although is less perturbed than independent bands to observation geometry, it is affected to some extent due to the increase of BRDF effects with wavelength, something that is evidenced by the larger improvements on the NIR band after the BRDF adjustment showed in Figure 5, and that is in agreement with previous studies [50, 65, 66]. The largest improvements in APU were obtained with both the BRDF and spectral adjustments applied.

The accuracy, precision, and uncertainty graphs revealed similar performance between the Red and NIR bands, with results for most of the AVHRR sensor-bands close or within the combined AVHRR and TM5 specification. Regarding the shape of the APU curves, two effects can be noted: First, the aerosol and Rayleigh scattering that increase the signal reaching the sensor at low surface reflectance values; and second, the signal attenuation by aerosol absorption that occurs at higher values [67]. These effects are shown by the APU with low and high reflectance values showing a positive and negative bias, respectively.

Temporal variations in APU were relatively small, with a general decreasing trend during the study period. In the case of the N07-N14, there is an increase in the uncertainty during the lifetime of each sensor, which can be attributed to

45

their orbital drift [68, 69]. This effect was not evident on N16-N19 platforms, as their orbits were more stable during the years included in the study period. These results were consistent with the errors reported by the previous evaluation of N16-N19 surface reflectance using MODIS [8]. Seasonal analysis of relative uncertainties did not show significant differences between seasons.

The spatial distribution of accuracies showed better performance of the Red band, which had biases closer to zero and that were more stable. Results for the NIR showed inconsistencies in the biases between some sensors, which were more noticeable between N11 and N14. These results are coherent to findings of previous studies that reported abrupt changes in the LTDR surface reflectance magnitude when transitioning between sensors [3,23]. Spatial distribution of relative uncertainties was consistent between the sensors on all POES satellites. The highest values were located over high latitudes and over tropical regions, which might be attributed to stronger atmospheric effects [28], cloud and snow pixel miss-classification in these areas [50,70], and varying performance of the LTDR over different land cover types. The latter was also evidenced by the land cover analysis that revealed larger and less consistent uncertainties over forest classes. Overall, the NIR showed lower relative uncertainties than the Red, which is due to the normally higher NIR reflectance magnitudes.

The spatial analysis of Red versus NIR bands errors showed strong correlations over barren and sparsely vegetated areas, which are commonly associated with low values of vegetation indices such as the Normalized Difference Vegetation Index (NDVI) and 2-band Enhanced Vegetation Index (EVI2). In contrast, only weak

relationships were found over other regions and land covers. This might be of particular interest to producers and users of AVHRR land datasets, as error correlation between bands can impact downstream products.

2.7   Conclusions

In this study we evaluated the accuracy, precision, and uncertainty of the AVHRR Long Term Data Record for the period 1984-2011 using globally distributed data from the Thematic-Mapper sensor onboard Landsat-5 used as a reference. The evaluation was carried out for the AVHRR sensor on each POES satellite independently.

We analyzed four different adjustment levels of AVHRR data: a "No-Adjustment" level, obtained by removing the BRDF normalization initially present on the LTDR product, which represents the original AVHRR data after the atmospheric correction process; a "BRDF adjusted level" which was obtained by implementing the VJB method to account for reflectance variations due to changes in sun and view geometries; a "spectrally adjusted level", where spectral adjustment factors derived from Hyperion hyperspectral data were applied to minimize the band spectral differences between sensors; and a final adjustment stage, where both the BRDF and spectral adjustments are applied. The VJB BRDF-correction method used in the LTDR showed good performance when it was used to adjust the AVHRR observations to the Landsat-5 geometry, reducing the uncertainties when compared to unadjusted data. The spectral adjustment factors derived from Hyperion data proved to be ef-

ficient, when applied to BRDF-normalized data, further reducing the uncertainties in most cases. However, when it was applied to data without BRDF correction, the results were mixed, and evidence of over adjustment was observed.

Results of the cross-comparison showed a good agreement between AVHRR and TM5, with uncertainties that were close to or within the proposed combined specification of $0.071\rho+0.0071$. The Red band showed biases closer to zero and more temporally consistent than the NIR band, which broad spectral response makes it especially sensitive to water vapor absorption effects. Moreover, certain regions showed inconsistencies in the surface reflectance bias between contiguous AVHRR sensors, which suggests that, depending on the nature of their study, users of the current LTDR version might still need to utilize data normalization steps and carefully examine their results for artifacts.

The next chapters of the dissertation will attempt to reduce some of the record inconsistencies found in this study. Chapter 3 will target the atmospheric correction process, and in particular, the retrieval of water vapor for atmospheric correction. Chapter 4 will target the calibration inconsistencies and attempt to calibrate the surface reflectance product using stable areas.

Chapter 3:   Global estimation of water vapor from AVHRR

3.1   Abstract

Water vapor impact on the AVHRR signal has been estimated to be between 0.7% to 4.4% for the red channel and between 7.7% to 25% for the NIR channel. Previous studies have shown that water vapor can be derived from AVHRR thermal channels using a split-window model based on the strong linear relationship between water vapor content and the brightness temperature difference (ΔBT) of two channels with differential attenuation by water vapor. This relationship is strongly dependent on local characteristics such as spectral emissivity, surface temperature, and atmospheric conditions, which has historically limited it's global applicability. This study proposes a method to statistically calibrate the split-window coefficients for AVHRR using ΔBT from AVHRR N19 channels 4 (11μm) and 5 (12μm) with collocated total water vapor content from MYD09CMG using data between 2010 and 2014. The split-window coefficients derived from N19 are then used estimate the column water vapor from AVHRR ΔBT. Spectral response differences between AVHRR instruments are accounted for using spectral adjustment factors derived from MODTRAN simulations. The water vapor estimations are evaluated with observations from globally distributed AERONET sunphotometers and the

water vapor estimates from MODIS Aqua. Results show good agreement between AVHRR-estimated water vapor and both reference datasets, with a determination coefficient greater than 0.75 and an error lower than $0.50 g \cdot cm^{-2}$.

3.2 Introduction

Absorption of electromagnetic radiation by water vapor limits the atmospheric windows available for Earth observation. Water vapor absorbs electromagnetic radiation through rotational, vibrational, and electronic transitions. Rotational transitions are responsible for absorption in the far-infrared and microwave regions, vibrational transitions for absorption in the infrared, and electronic transitions for absorption in the visible and ultra-violet. Modern Earth observation instruments count with narrow spectral channels designed to avoid regions of water vapor absorption. Unfortunately, due to technological limitations at the time of its design[1], this is not the case for AVHRR, which counts with broad spectral channels that overlap water vapor absorption bands (Figure 3.1).

Several authors have studied the effects of water vapor on AVHRR visible channels and derived indices. From radiative transfer simulations, [30] estimated that for typical water vapor contents between 0.5 - 4.1 $g \cdot cm^{-2}$, the Red channel signal can decrease between 0.7% - 4.4%, the NIR signal between 7.7% - 25%, and the NDVI between 0.011 - 0.12 units. [71] analyzed the effects of water vapor uncertainty on the AVHRR NDVI over the Sahel with similar results. The atmospheric correction process in the current LTDR version considers the water vapor content from three

---

[1]Broad spectral channels were needed to achieve an acceptable signal-to-noise ratio.
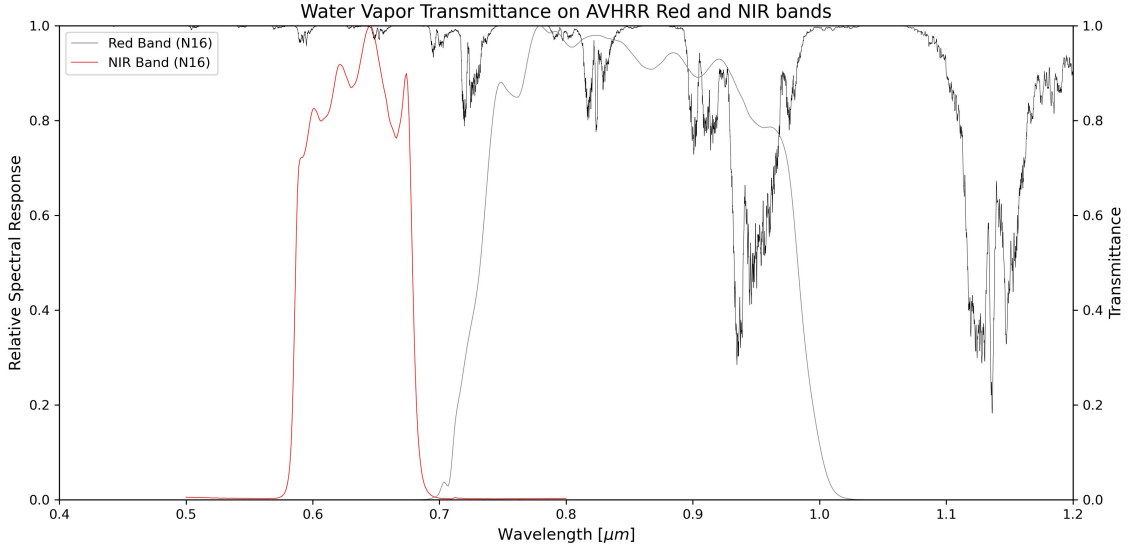
Figure 3.1: Water vapor transmittance spectrum on the range of AVHRR visible channels. A weak absorption band occurs within the waveband of AVHRR Red Channel and a much stronger one on the NIR.

ancillary sources. For the pre-MODIS era (N-7/-9/-11/-14), water vapor information is obtained from either the NCEP/NCAR Reanalysis (NCEP R1) or the NCEP Global Data Assimilation System (GDAS). During the MODIS era (N-16/-18/-19), water vapor is obtained from same-day MODIS Terra or Aqua observations. If MODIS data for a particular day is not available, then the LTDR processing system uses GDAS or NCEP R1 data. Table 3.1 shows the main characteristics of the three ancillary datasets.

Sources[1]	Period	Spatial Res.[2]	Temp. Res.
MODIS [31]	2000-2020	0.05° x 0.05°	daily
NCEP/GDAS [33]	1984-2020	1.00° x 1.00°	6 hours
NCEP R1 [34]	1984-2020	2.50° x 2.50°	6 hours

[1]Data selection is prioritized as: MODIS→NCEP/GDAS→NCEP/R1.

[2]Spatial resolution is shown in latitude x longitude.

Table 3.1: Water vapor sources for LTDR atmospheric correction.

The three datasets have different spatiotemporal characteristics and are pro-

cessed differently. Data from MODIS is obtained in the same CMG grid as the LTDR product and correspond to the same-day observation from Terra or Aqua (in that order[2]). Due to this characteristics, no spatial or temporal interpolation of MODIS water vapor is done before it's use on the LTDR. Data from the NCEP/GDAS and NCEP R1 is much coarser than the LTDR CMG resolution and requires interpolation before being used. In both cases, the data is bi-linearly interpolated in space from the closes four grid cells, and linearly interpolated in time from the two closest observations to AVHRR's overpass. This situation is not ideal, as NCEP data might be too coarse to characterize local water vapor variations [15, 72, 73] and MODIS data might be too temporally distant to represent the water vapor value at AVHRR overpass time accurately.

If possible, the water vapor used for atmospheric correction should be derived from the same sensor that measures the TOA reflectance [71]. This approach was first tested with MODIS, which counts with three NIR channels located within the $0.94 \mu m$ water vapor band absorption region that were implemented with the purpose of water vapor retrieval [31]. Other modern sensors have also implemented this approach. More recent missions, such Sentinel-2 [74] and Sentinel-3 [75] also implement a similar approach.

Unfortunately, AVHRR does not count with bands specifically implemented with the purpose of water vapor retrieval over land [76]. However, starting with AVHRR/2 on N07 (Table 1.2), the instrument design included a second band on

---

[2]MODIS ancillary data used was originally intended to correct Landsat-8 observations, which overpass time matches closely with Terra.

the thermal infrared region. The presence of two thermal infrared bands centered at $11\mu m$ and $12\mu m$ enabled the development and implementation of numerous split-window algorithms, which depends on the differential atmospheric absorption in two adjacent thermal infrared channels. Split-window algorithm have been applied to AVHRR data for retrieving Sea Surface Temperature (SST) [77, 78], Land Surface Temperature (LST) [79, 80], and water vapor content over oceans [76] and land [15, 71, 81]. The latter ones are of particular interest for this chapter, as they provide an insight of potential methods for the operational retrieval of AVHRR water vapor over land.

[76] showed that, the brightness temperature difference (ΔBT) between AVHRR bands 4 ($11\mu m$) and 5 ($12\mu m$) is linearly related to the atmospheric water vapor content (u_{wv}), such that: $u_{wv} = a\Delta BT + b$. He first derived the split-window relationship using radiative transfer simulations and then evaluated it using simulated AVHRR bands and radiosonde measurements over the ocean. His results showed that AVHRR thermal bands can retrieve water vapor concentration with an error of $\pm 0.5 g \cdot cm^{-2}$. The method proposed by [76] was later evaluated by [71] over the Sahel region, who found different coefficients but similar errors ($\pm 0.51 g \cdot cm^{-2}$) when compared to radiosonde measurements. He suggested that the difference in regression coefficients between both studies might be explained by several surface and atmospheric characteristics. This was in agreement with previous results from [79] that showed a strong dependency between ΔBT and spectral emissivity.

The dependency of the relationship between ΔBT and u_{wv} with local atmospheric and surface conditions is something that historically has limited its global

application. Contrary to the ocean surface, where emissivity is stable, land surface emissivity varies with land cover, and makes the estimation of globally-applicable split-window parameters a more complex matter.

This chapter presents a method to derive water vapor globally over land using the split-window algorithm from [76] and an approach proposed by [15]. The method is based on near-simultaneous observations from AVHRR (N19) thermal bands and MODIS Aqua Total Column Water Vapor (TCWV) derived from bands 18 and 19. To transfer the split-window coefficients from N19 to other AVHRR instruments, we use spectral adjustment factors derived from radiative transfer simulations to account for spectral differences. We then evaluate the derived water vapor using collocated sunphotometer observations from AERONET and near-simultaneous observations from MODIS Aqua. Finally, we evaluate the water vapor estimates in the context of the LTDR atmospheric correction by comparing the LTDR surface reflectance generated using water vapor from AVHRR to surface reflectance values generated using MODIS water vapor. Section 3.3 describes the data and materials used in this chapter. Section 3.4 presents the methodology. Section 3.5 presents the results and Section 3.6 their discussion. Finally, section 3.7 gives the chapter conclusions.

3.3 Data

3.3.1 AVHRR Brightness Temperature

The AVHRR surface reflectance Long Term Data Record (LTDR) V5 [8] spans the period between 1981 to the present day and provides daily global BRDF-normalized surface reflectance, brightness temperature, and view and solar geometry information at a spatial resolution of 0.05°x0.05° (latitude-longitude) in the Climate Modeling Grid (CMG). For this study, we use brightness temperature from bands 4 (11μm) and 5 (12μm); the view zenith angles; and the control quality layer, which was used to remove observations contaminated by clouds or other atmospheric effects and leave only those with the highest quality. The AVHRR LTDR products were obtained from the LTDR project website[3].

3.3.2 MODIS Brightness Temperature and Water Vapor

The MYD09CMG product from MODIS Aqua collection 6 provides daily global surface reflectance, brightness temperature, view and solar geometries, and information of several atmospheric variables from 2002 to the present day. Similarly to the AVHRR LTDR, the MYD09CMG product is generated at a spatial resolution of 0.05°x0.0° (latitude-longitude) in the Climate Modeling Grid (CMG). For this study we use brightness temperature from bands 31 (11μm) and 32 (12μm), the columnar water vapor (CWV) content, view and solar angles information, and the quality

---

[3]https://ltdr.modaps.eosdis.nasa.gov

assessment layer. As with the AVHRR data, we used the quality layer to remove observations contaminated by clouds and other atmospheric effects. The water vapor content in the MYD09CMG product is derived from bands 18 (0.936μm) and 19 (0.940μm) following a two-band approach with a theoretical accuracy of 5-10% [31]. Recent studies have shown wet biases between Aqua water vapor derived using the two-band approach when compared to data from ground based stations [82–84]. The MYD09CMG data was obtained from the Land Processes Distributed Active Archive Center[4].

3.3.3 AERONET Water Vapor

We use columnar water vapor data from the AErosol RObotic NETwork (AERONET) to evaluate the water vapor derived from MODIS and AVHRR. AERONET is a federated network with more than 400 sites distributed globally, which represent a wide gamut of atmospheric conditions. Data from AERONET has been used to evaluate the retrieval of water vapor content by numerous studies [84–86]. For this study, we use *Precipitable Water* data from AERONET Version 3.0 Level 2.0. The *Precipitable Water* dataset corresponds to the columnar water vapor content and is retrieved using the Beer-Lamber-Bouguer attenuation law and modeled water vapor transmittances. More information on AERONET and its water vapor retrieval algorithm can be found in [87,88]. AERONET data was downloaded from the project's website[5].

---

[4]https://e4ftl01.cr.usgs.gov/MOLA/MYD09CMG.006/.
[5]https://aeronet.gsfc.nasa.gov/

3.3.4 Global Atmospheric Profiles from Reanalysis Information

The Global Atmospheric Profiles from Reanalysis Information database [89] (GAPRI) is a compilation of 8,324 globally distributed vertical atmospheric profiles from ERA-Interim [90]. Atmospheric profiles in GAPRI includes information on geopotential height, atmospheric pressure, air temperature and relative humidity at 29 vertical levels. The GAPRI database has been used by several studies for the radiative transfer simulation of brightness temperatures and the development of generalized algorithms to estimate land surface temperature. In this study, we used the atmospheric profiles to simulate 11um and 12um brightness temperatures from AVHRR and MODIS to derive spectral adjustment coefficients. GAPRI profiles were obtained directly from their authors.

3.3.5 Relative Spectral Responses of AVHRR and MODIS Thermal Channels

Relative spectral responses (RSR) from the AVHRR instruments on the LTDR were used to spectrally convolve simulated radiance spectra and derive spectral adjustment factors. Figure 3 shows the RSR for each AVHRR sensor considered (N07 to N19), and for MODIS Aqua. The RSR were obtained from the NASA Langley cloud and radiation research webpage[6].

---

[6]https://cloudsway2.larc.nasa.gov

3.4   Method

3.4.1   Collocation between satellite and AERONET measurements

To match and AERONET and satellite observations we utilized a collocation approach used by several studies [28, 43, 85]. At the location of each AERONET site, we extracted the value from the closest CMG pixel (AVHRR or MODIS) and compared it to the temporal average of all valid AERONET observations within 30 minutes of the satellite overpass.

3.4.2   Spectral adjustment of brightness temperatures

Relative spectral responses (RSR) determine how a continuous spectrum from the surface is recorded on a sensor's discrete band. In this work, we adjusted the differences between different sensors brightness temperatures using spectral adjustment coefficients derived from radiative transfer simulations. For this, atmospheric profiles from GAPRI were used as inputs of the Moderate Spectral Resolution Atmospheric Transmittance Model (MODTRAN) version 4 to simulate a dataset of 8,324 radiance spectra. The radiance spectra were then convolved with AVHRR and MODIS relative spectral responses as shown in Equation 3.1, where $L^{'}$ is the radiance spectra, $\bar{L}^{'}$ the convolved radiance, and λ represents each spectral band.

$$\bar{L}^{'}_{\lambda} = \frac{\int L^{'}_{\lambda} RSR_{\lambda} d_{\lambda}}{\int RSR_{\lambda} d_{\lambda}} \tag{3.1}$$

The convolved radiances were then converted to at-sensor brightness temperatures (BT) using Equation 3.2, where c_1 is equal to $1.1910427x10^{-5} \left[\frac{mW}{m^2 \cdot sr \cdot cm^{-4}}\right]$ and c_2 is equal to $1.4387770 \left[cm \cdot K\right]$; v_c is the central wavenumber of each channel; and A and B are sensor specific coefficients. For this study, the A and B coefficients were obtained from the RTTOV V12 radiative transfer code database [91]. Note that BT and $\bar{L}'$ correspond to spectral values, but the λ subscript was dropped for simplicity.

$$BT = \frac{\frac{c_2 v_c}{\ln\left(1 + \frac{c_1 v_c^3}{L'}\right)} - A}{B} \tag{3.2}$$

Finally, we used a linear fit to compute the adjustment coefficients between the brightness temperature of two sensors corresponding bands.

3.4.3 Calibration of Aqua TCWV with AERONET

For this study, we use TCWV from MODIS product MYD09CMG as a reference to calibrate a split-window algorithm with AVHRR thermal data. Due to wet biases reported by previous studies [82–84], we first calibrate the MYD09CMG water vapor using collocated data from AERONET sites between 2002 and 2019. For this, we kept only the collocated matches in which MODIS pixels were flagged as clear and with low aerosol content. The number of matched observations was mostly dependent on AERONET data availability and cloud conditions at Aqua overpass time. Figure 3.2 shows the number of matched observations at each AERONET site.
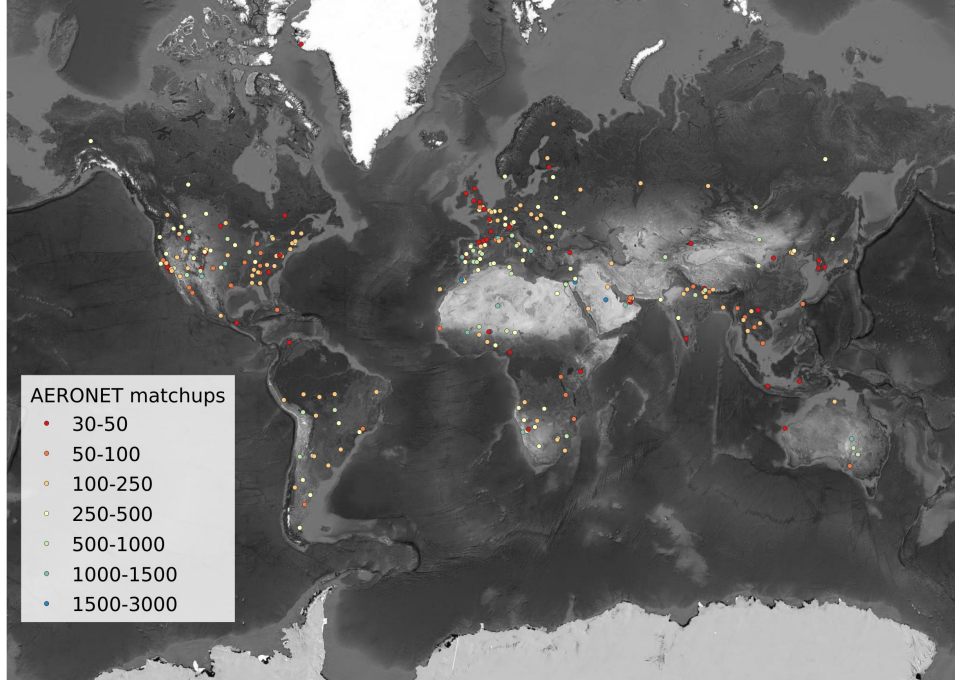
Figure 3.2: Number of match-ups between AERONET and MYD09CMG observations. The number of sites is 312 and the total number of observations after filtering is 52,637.

3.4.4 Global derivation of split-window coefficients

Our approach to derive water vapor from AVHRR data relies on the split-window model proposed by [76] and later tested by [15,71]. This model is based on the strong linear relationship between water vapor content (u_{wv}) and the brightness temperature difference (ΔBT) of two bands with different water vapor absorption coefficients (Equation 3.3).

$$u_{wv} = a\Delta BT + b \tag{3.3}$$

The a and b coefficients can be statistically derived using matched observations. Previous studies have suggested that these coefficients are site specific and depend on local conditions such as spectral emissivity, surface temperature, and atmospheric

conditions [71, 79].

3.4.4.1   MODIS bands 31 ($11\mu m$) and 32($12\mu m$)

We first evaluated the global validity of the split-window model using five years of MYD09CMG data (2004 through 2008) to analyze the relationship between the ΔBT of bands 31 (11um) and 32 (12um) with the water vapor content derived from near-infrared bands 18 and 19 [31]. It is important to mention that the water vapor in the MYD09CMG product correspond to the total column water vapor, i.e., the total water vapor in the signal path normalized by the total air mass. Note that in the case of thermal bands, the signal only travels through the atmosphere once: on its path from the surface emission to the sensor. In the case of the near-infrared bands, the signal travels through the atmosphere twice: first when it enters the Earth's atmosphere towards the surface, and then when is reflected and travels towards the sensor. This means that depending on the observation and solar geometry, the water vapor in the path of the NIR bands could differ substantially from the one in the path of the thermal bands.

3.4.4.2   AVHRR bands 4($11\mu m$) and 5($12\mu m$)

Next, to derive the split-window coefficients for AVHRR, we calibrated Equation using ΔBT from bands 4 (11um) and 5 (12um) with the collocated water vapor from MYD09CMG (previously calibrated using global AERONET observations as explained in section 3.4.3). The calibration of the split-window coefficients was

done using data from NOAA-19 between 2010 and 2014. We only considered clear observations with low or average aerosol content, and in which the overpass time difference between AVHRR and MODIS was smaller than 30 minutes. The clear observations were selected using each product's quality flags, and the aerosol quantity was obtained from the MYD09CMG product "State QA" dataset.

3.4.5 Global estimation of water vapor over land from AVHRR

We then used the split-window coefficients derived for the different AVHRR sensors to estimate the integrated water vapor content from AVHRR ΔBT. To account for spectral differences between N19 and the other AVHRR instruments, we used the spectral adjustment factors derived in section 3.4.2.

3.4.6 Evaluation of AVHRR water vapor performance

We evaluated the performance of the water vapor derived from AVHRR against two references datasets:

1. Collocated observations from AERONET sunphotometers.

2. Near-simultaneous ($\pm$30 minutes) TCWV from MODIS-Aqua.

In both cases, we evaluated the water vapor estimates from N16 (2002-2005), N18 (2005-2009), and N19 (2015-2017)[7] using three common statistical metrics:

$$Bias = \frac{\sum_{i=1}^{n} \epsilon_i}{N} \quad Sigma = \sqrt{\frac{1}{N-1} \sum_{i=1}^{n} (\epsilon_i - A)^2} \quad RMSE = \sqrt{\frac{1}{N} \sum_{i-1}^{N} \epsilon_i^2}$$

---

[7]Note that this period is different than the one used to calibrate N19.

where ϵ_i corresponds to the estimated value minus the reference value and N the number of observations.

3.4.7 Evaluation of AVHRR water vapor for atmospheric correction

Water vapor content is a crucial variable in the atmospheric correction of AVHRR data, particularly for the NIR band. To evaluate the performance of the AVHRR-derived water vapor in the context of the LTDR atmospheric correction, we first extracted the top-of-atmosphere (TOA) reflectance and ancillary data time series from N16, N18, and N19 over 444 BELMANIP-2 sites [92]. This provided a database that is well-representative of different land cover and atmospheric conditions, and that allows us to analyze the atmospheric correction process without having to reprocess the entire LTDR record. We then ran the 6S code twice for each observation: **(1)** with the water vapor from MODIS closest overpass; and **(2)** with the water vapor derived from AVHRR. All other ancillary variables were maintained equal between successive 6S runs. Finally, we used the dataset of surface reflectances based on MODIS water vapor as a reference to evaluate the surface reflectance obtained using water vapor from AVHRR.

3.5 Results

3.5.1 Evaluation of MODIS Aqua TCWV with AERONET

Results showed a strong relationship ($R^2>0.9$) and low errors (RMSE$<$0.5cm) between TCWV from Aqua and AERONET (Figure 3.3). However, there is a wet

bias in Aqua TCWV of around 0.4 [cm] that increased with water vapor content and should be accounted for. For the the rest of this study, we calibrated the TCWV from AQUA to AERONET-like values using the slope (0.827) and intercept (-0.113) computed in from this evaluation.
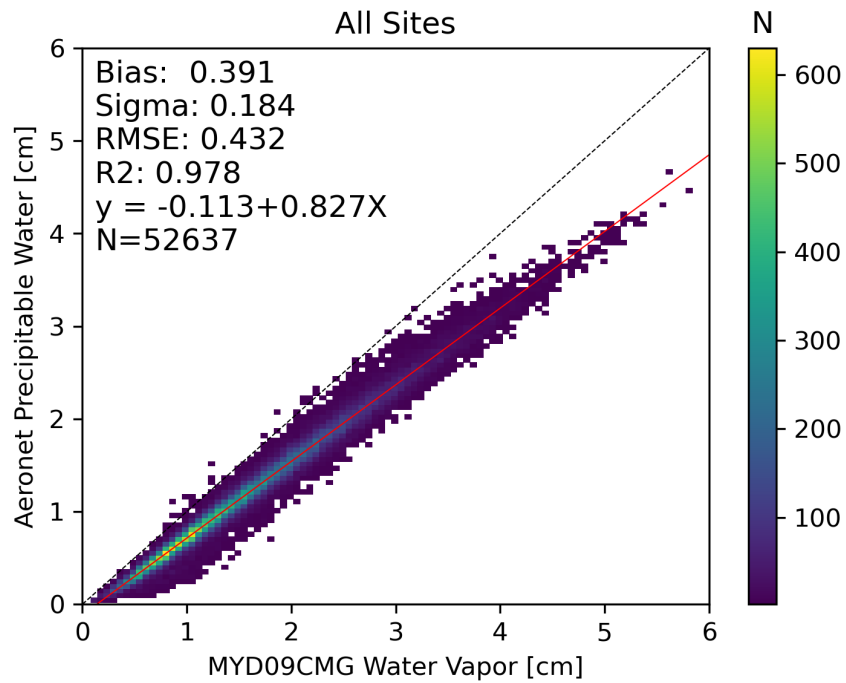
Figure 3.3: Evaluation of MYD09CMG water vapor with AERONET Data. The dashed line corresponds to the 1:1 line and the solid red line is the regression line.

3.5.2 Global estimation of split-window coefficients

3.5.2.1 MODIS Aqua B31-B32 ΔBT vs TCWV

Results showed a globally strong relationship between Aqua B31-B32 ΔBT and TCWV content. Figure 3.4 shows the global distribution and histogram of R^2 values.
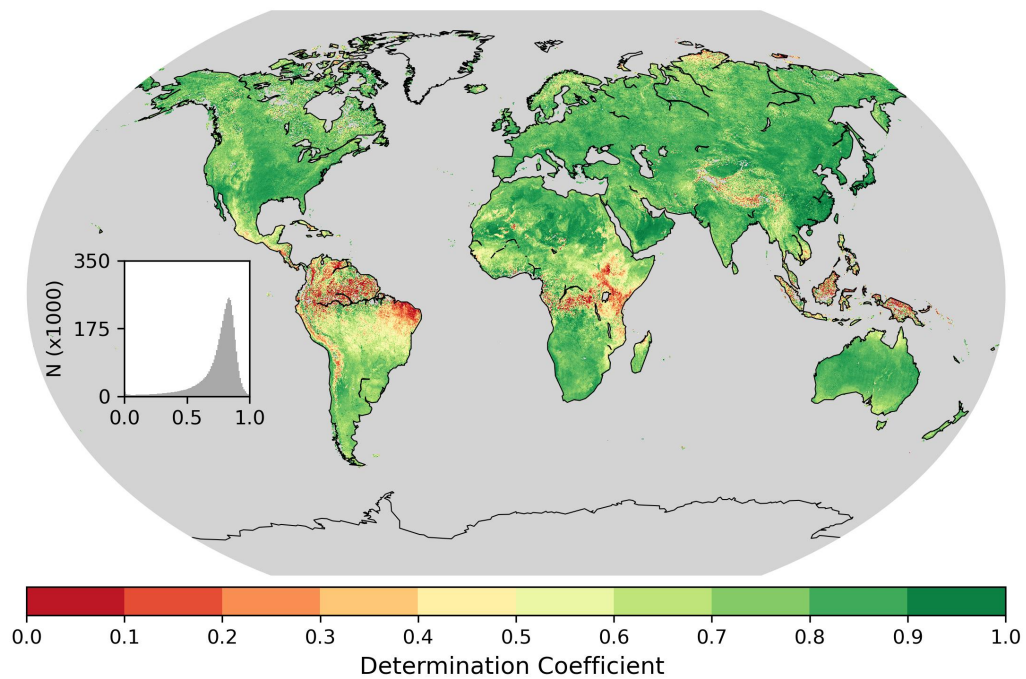
Figure 3.4: Determination coefficient between MYD09CMG B31-B32 brightness temperature difference and MYD09CMG columnar water vapor. Gray areas correspond to regions with no available data.

The distribution of R^2 values was skewed towards high values, with a mean of 0.75±0.14, and a median of 0.80 with and inter-quantile range of 0.14. Overall, 88% of pixels had a R^2 value higher than 0.6. Generally, tropical areas showed the lowest values. Next, Figure 3.5 shows results for the regression slope.
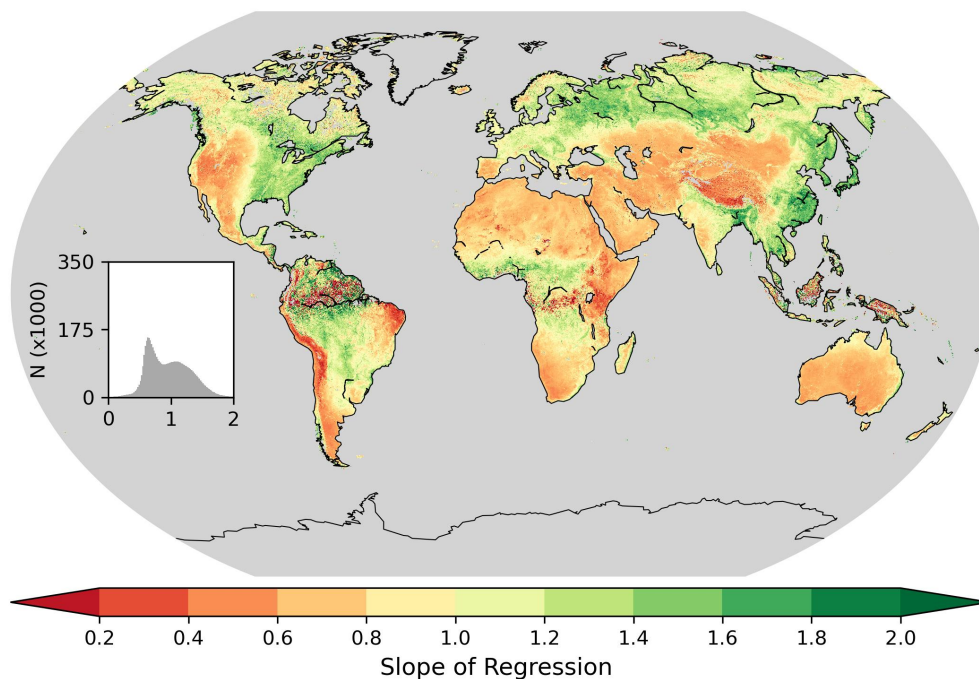
Figure 3.5: Regression slope between MYD09CMG B31-B32 brightness temperature difference and MYD09CMG columnar water vapor. Gray areas correspond to regions with no available data.

The regression slope showed a bimodal distribution, with the main peak at around 0.65 and a lower peak at around 1.10. There is a noticeable difference between areas with no or sparse vegetation (slopes<1) and vegetated areas (slope>1).

3.5.2.2   AVHRR NOAA-19 B4-B5 ΔBT vs MODIS Aqua TCWV

Similarly to MODIS, results showed a globally strong relationship between AVHRR N19 B4-B5 ΔBT and MODIS Aqua TCWV content. Figure 3.6 shows the global distribution and histogram of R^2 values.

The distribution of R^2 was skewed towards high values, with a mean of 0.70±0.17, and a median of 0.74 with and inter-quantile range of 0.18, with 78% of pixels scoring
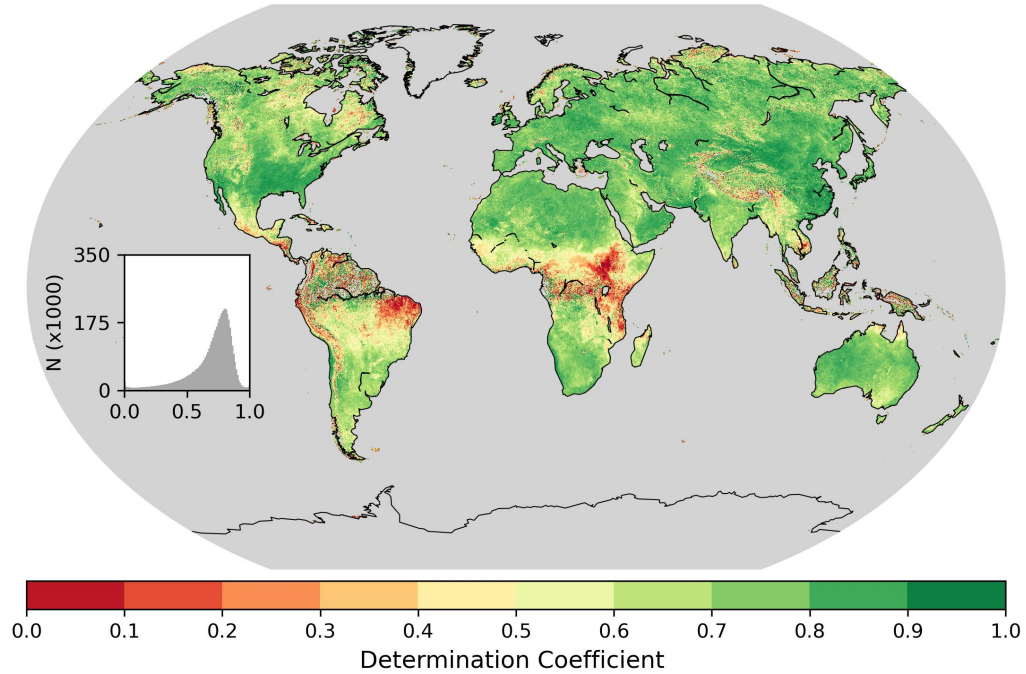
Figure 3.6: Determination coefficient between AVHRR (N19) B4-B5 brightness temperature difference and MODIS (Aqua) columnar water vapor. Gray areas correspond to regions with no available data.

a R^2 value higher than 0.6. As with MODIS, some pixels located in tropical regions showed particularly low R^2 values. Figure 3.7 shows results for the regression slope. Note that in this case the range of values is different than 3.5. For AVHRR the regression slope also showed a bimodal distribution. The the main peak was located at around 0.40 with a lower peak at around 0.57. Results for N16 and N18 were similar and are omitted for brevity.
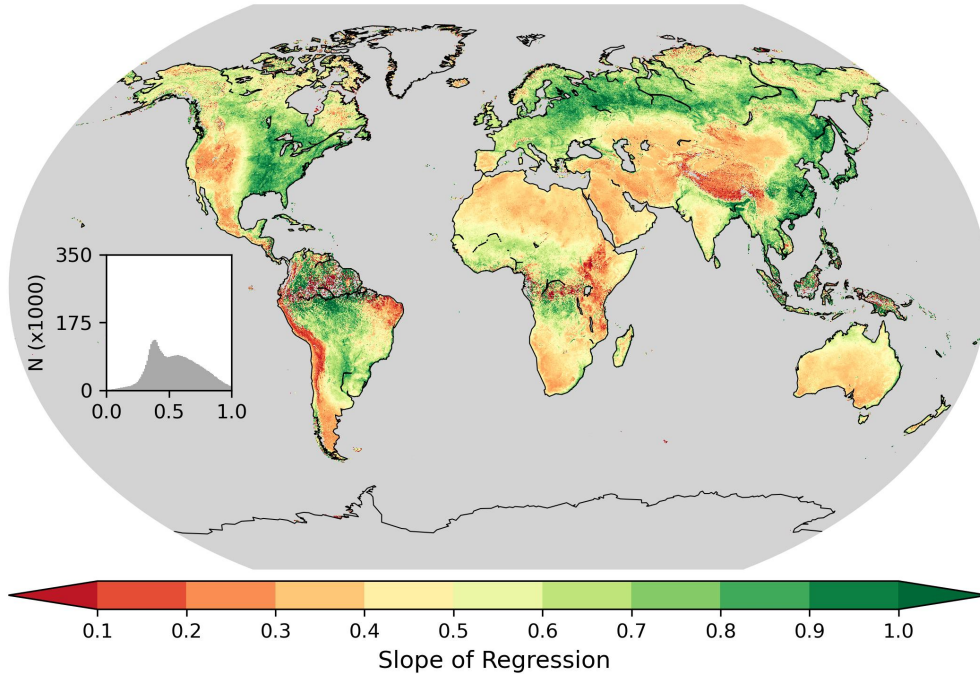
Figure 3.7: Regression slope between AVHRR (N19) B4-B5 brightness temperature difference and MODIS (Aqua) columnar water vapor. Gray areas correspond to regions with no available data.

3.5.3 Evaluation of AVHRR water vapor with AERONET

The comparison between AVHRR and AERONET TCWV is shown in Figure 3.8. In the case of N16 and N18, the ΔBT between B4 and B5 was spectrally adjusted to N19-like values before computing the TCWV (Section 3.4.2). Results of the evaluation showed good agreement between AVHRR water vapor and AERONET observations. The R^2 was greater than 0.75 and RMSE lower than 0.45 $g \cdot cm^{-2}$ for all three cases. Values for the bias were low, with N18 showing the largest differences of 0.13 $g \cdot cm^{-2}$. The Sigma (i.e., the estimates' precision) was similar between N-16/-18/-19 and explained most of the estimation uncertainty.
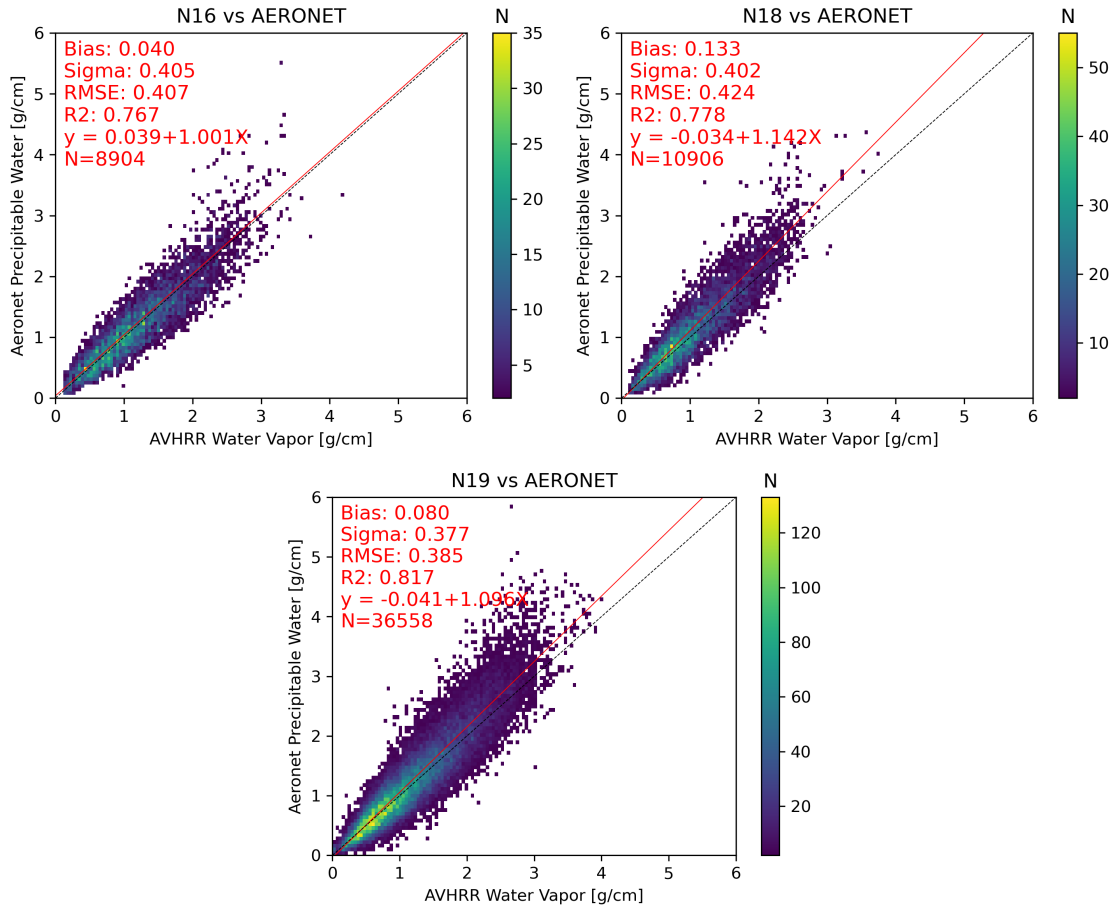
Figure 3.8: Evaluation of column water vapor derived from AVHRR vs collocated measurements from AERONET. Results are shown for N16, N18, and N19.

3.5.4 Global evaluation of AVHRR water vapor with MODIS Aqua

Next, we show the bias, R^2, and RMSE of the global evaluation between TCWV from AVHRR N-16/-18/-19 with MODIS Aqua (Figure 3.9). As mentioned before, the N-16/-18 ΔBT was spectrally adjusted to N19-like values before computing the TCWV (Section 3.4.2).
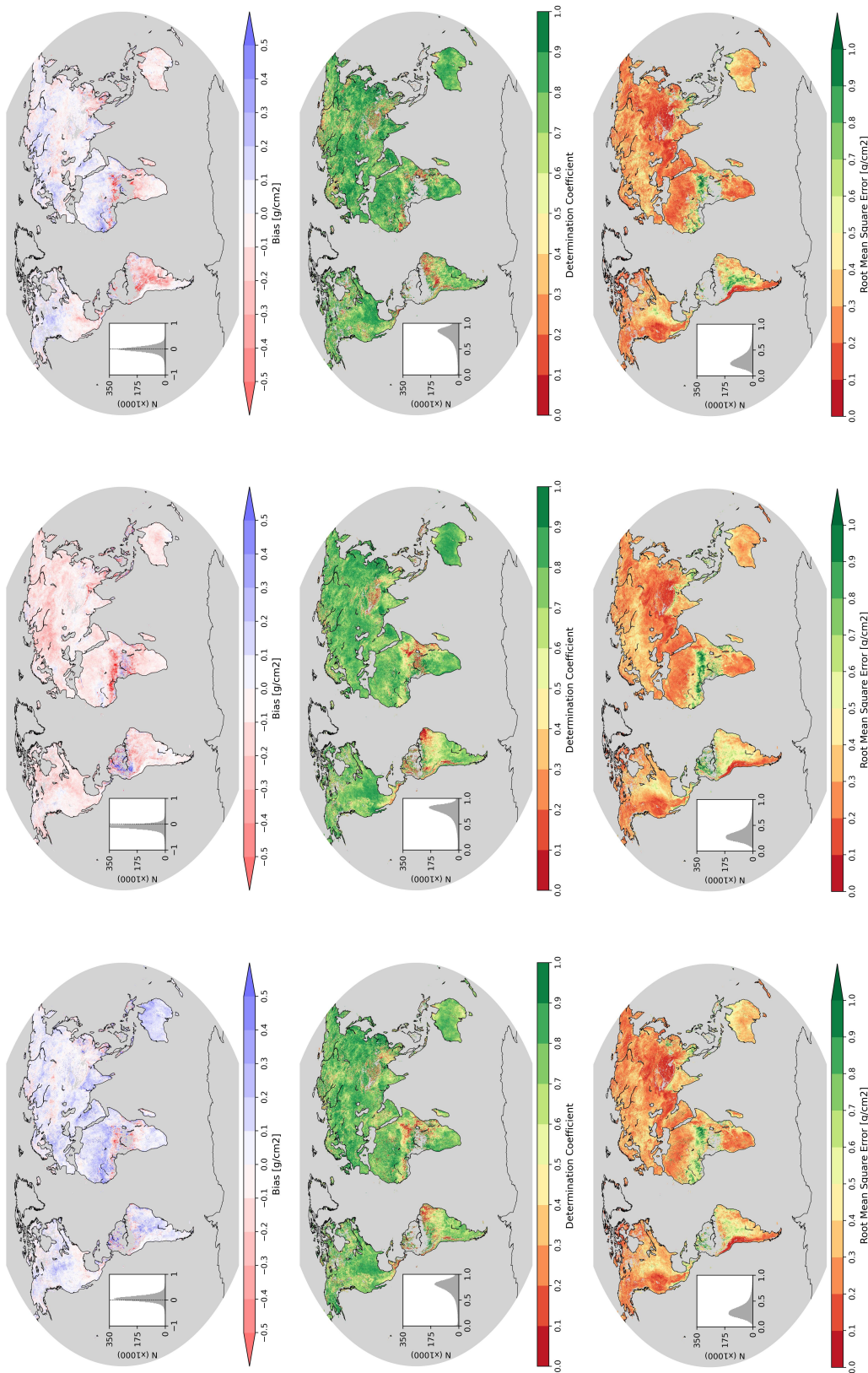
Figure 3.9: Evaluation of TCWV from N16 (left), N18 (center), and N19 (right) with MODIS Aqua TCWV. Only pixels with >30 matches are shown.

Results of the global evaluation show good performance of the TCWV from AVHRR when compared to MODIS Aqua. Bias for N16 and N19 were close and distributed around 0, while N18 values showed a small dry bias. The magnitude and spatial distribution of R^2 and RMSE was similar between the three platforms: R^2 values were generally greater than 0.65 and RMSE values were lower than 0.5. All three metrics showed poor performance on tropical regions.

3.5.5 Evaluation of AVHRR water vapor for atmospheric correction

Figure 3.10 shows the evaluation of AVHRR-derived water vapor on the atmospheric correction of surface reflectance and NDVI.
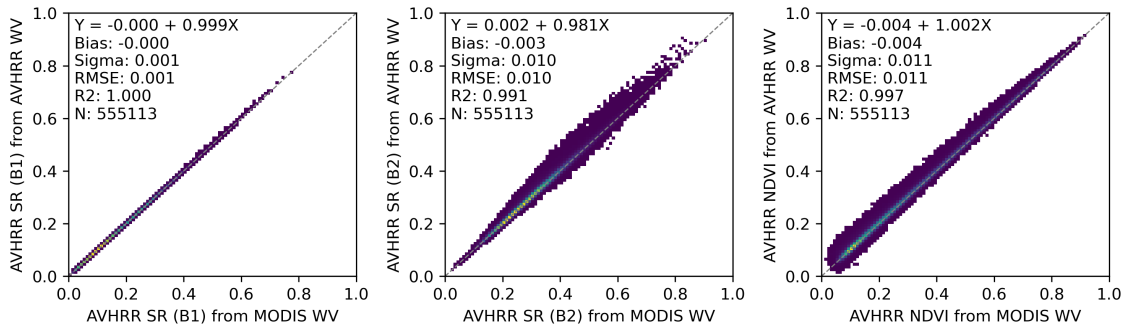
Figure 3.10: Comparison of atmospheric correction results using water vapor derived from AVHRR against results from MODIS water vapor values. Results are shown Red (left), NIR (center), and NDVI (right).

Results of the atmospheric correction evaluation showed good agreement between surface reflectance corrected with water vapor values from AVHRR and MODIS. Results for the Red band were practically identical, which due to the low influence of water vapor at shorter visible wavelengths was something to be expected. In this sense, results for the NIR and NDVI are more interesting. Only minor differences

71

were found for the NIR between both sets of values, with a Bias of 0.003, RMSE of 0.010, and R^2 of 0.991. The NDVI showed positive results as well, with a Bias of 0.004, RMSE of 0.011, and R^2 of 0.997.

3.6   Discussion

The evaluation of TCWV from MODIS Aqua with AERONET showed good relationship between both datasets but a wet bias on MODIS, which is in agreement to results from other studies that compared TCWV retrievals from Aqua NIR bands with GPS stations [82, 83] and other ground based techniques [84]. These results were useful to adjust the TCWV from Aqua before using it to calibrate the split-window algorithm, thus minimizing the potential biases on AVHRR estimates.

The relationship between TCWV and AVHRR ΔBT used in this chapter has been well characterized by previous studies but only for specific surface and atmospheric characteristics. Over oceans, where spectral emissivity is stable, this relationship can be accurately described by radiative transfer simulations [76]. In contrast, spectral and atmospheric characteristics over land surfaces are more diverse, which makes describing the relationship between TCWV and ΔBT more complex [79] and limits the applicability of coefficients derived from radiative transfer. In this study we overcome this limitation by deriving location specific split-window coefficients using near-simultaneous observations from MODIS Aqua at a global scale.

The proposed method agrees well with results from a previous study by [15] that computed split-window coefficients between NOAA-16 ΔBT and TCWV from MODIS Aqua over an homogeneous area in the Saharan desert. That study found a linear slope and intercept of 0.41 and 1.0, respectively. In comparison, over the same area our method yields a slope of 0.38 and intercept of 1.0.

Regarding the spatial distribution of the split-window coefficients, the results from this study give some interesting insights. For both of MODIS ΔBT and AVHRR ΔBT, there is a noticeable difference in the regression slope value between areas with no (or sparse) vegetation and vegetated areas, with marked transition zones between them. While this agrees with the dependence of the split-window method on the local surface emissivity, it suggests the possibility of estimating coefficients grouped by land cover class, which could be used to assign coefficients in areas where the number of matched AVHRR/AQUA observations are not enough for a robust statistical regression.

The evaluation with AERONET and MODIS showed good global performance of the TCWV from AVHRR, with errors that were generally close or lower to those found by previous studies [71, 76]. The poor performance of estimates in tropical regions might be attributed to persistent cloud coverage [93] or high water vapor content and variability [94]. Furthermore, the bad performance observed over the West African Sahel could be the result of swings between periods of drought and abundant rainfall [95], and increasingly frequently flooding events [96]. All these phenomena can modify the local relationship between ΔBT and TCWV and influence the estimated split-window coefficients.

Finally, when the TCWV from AVHRR was used in the atmospheric correction process of the LTDR, the obtained surface reflectance values showed a good agreement with the surface reflectance corrected using the TCWV from MODIS. These findings show that the proposed method is a valid alternative to derive TCWV for atmospheric correction directly from AVHRR, instead of depending on coarse resolution ancillary data, which might often be inadequate at representing the spatiotemporal variation of atmospheric water vapor.

3.7   Conclusions

This study presented the first estimates of TCWV over land derived from AVHRR at a global scale. This was achieved through the per-pixel calibration of a split-window algorithm using ΔBT from AVHRR N19 bands 4 $(11\mu m)$ and 5 $(12\mu m)$ with the collocated TCWV from MODIS Aqua. To transfer the split-window coefficients to AVHRR instruments on other NOAA platforms we used spectral adjustment factors derived from MODTRAN radiative transfer simulations. The TCWV derived from AVHRR was then evaluated against collocated AERONET and MODIS Aqua observation, showing good agreement and errors lower that those reported by previous studies. In terms of the LTDR atmospheric correction, the water vapor estimates from AVHRR were comparable to estimates from MODIS. The findings of this study are promising and a step-forward in both the improvement of the LTDR atmospheric correction and the potential generation of a long-term water vapor product from AVHRR. The next chapter will target calibration inconsisten-

cies between AVHRR instruments and attempt to calibrate the surface reflectance

product using stable areas.

Chapter 4: Recalibration of the AVHRR Long Term Data Record

4.1 Abstract

The LTDR is a unique source of information for the study of the Earth's surface processes and their long-term dynamics. However, numerous studies have evidenced calibration inconsistencies in the LTDR. This study proposes an approach for the recalibration of the record with observations from automatically selected stable areas. The areas are selected with a pattern-matching algorithm and then used to compare the surface reflectance from AVHRR with the MODIS climatological value and derive recalibration coefficients. The recalibration coefficients were evaluated using the comprehensive method presented in Chapter 2. Results from the evaluation were positive and showed that the derived coefficients improved the accuracy of most instruments. These findings are promising and show potential of the proposed method to improve the calibration of the LTDR and minimize the consistency issues.

4.2 Introduction

The surface reflectance LTDR is generated using almost 30 years of daily data from seven AVHRR instruments onboard different NOAA satellites. This makes the

LTDR a unique source of information for long-term studies of the Earth's surface. While numerous efforts have been made throughout the years to generate a well calibrated and consistent product, combining observations from multiple sensors is certainly not an easy task. In this context, numerous studies have shown inconsistencies between the observations made by the AVHRR instruments on board different NOAA platforms [3,4,23], especially for the period before NOAA-16, when the sensor degradation and orbital drift were major issues. This is something that studies have addressed by proposing corrections suitable for their intended purposes [3, 97, 98]. These issues should ideally be addressed by the data producers before they propagate to higher level products. In summary, there is a need to improve the LTDR surface reflectance inter-consistency.

The calibration of the AVHRR reflective bands is not an easy task due to the lack of an on-board calibration system [19], which has made the topic of AVHRR calibration popular in the literature for many years. In this regard, pseudo-invariant targets have been shown to be suitable for the detection of instrument degradation [15], and the transference of calibration coefficients from a well calibrated instrument [22]. In fact, pseudo-invariant stable calibration sites are the most exploited invariant targets for the purpose of sensor inter-calibration [99].

Numerous studies have proposed stable areas or analyzed their feasibility for the purpose. For example, [100] evaluated the temporal stability of twenty 100 x 100 km2 desert targets located in the Saharan and Arabian desert using TOA visible images from Meteosat-4 between July of 1989 and January of 1990 and found temporal variations of up to 15%, which were reduced to 3% with a desert-

specific BRDF model [101]. More recently, [22] analyzed a set of these sites using 12 years of MODIS Aqua Ch.1 TOA observations with similar results. However, one of the issues with calibration methods based on stable sites is their inability to detect changes in their reference targets, which are assumed to be stable during the inter-calibration period. In this regard, the use of multiple varied targets might aid in isolating the part of the signal variation that is independent of each site and can be assumed to emerge from the sensor. To this end, pattern-matching algorithms seem like an interesting alternative. These types of algorithms have already been applied to Land Use and Land Cover classification studies with good results [102, 103], so they seem to be a promising option for the automatic selection of stable areas.

One issue that can complicate the intercalibration and comparison of different instruments is related to differences in their spectral response. Which depending on the sensor combination, can cause differences of up to 20% [40]. This issue can be mitigated by deriving spectral adjustment coefficients that adjust the sensors to a common radiometric scale. Previous studied have accounted for this by deriving spectral band adjustment factors. For example, [104] took advantage of hyperspectral radiances from the Scanning Imaging Absorption Spectrometer for Atmospheric Cartography (SCIAMACHY) to spectrally adjust and inter-calibrate geostationary sensors by deriving SBAF on a global scale. More recently, [6] used a curated selection of laboratory measurements to derive and evaluate spectral adjustment equation between numerous sensors.

Moreover, differences in the signals from two sensors can be due to directional (BRDF) effects [36] and should be accounted for. While the LTDR product includes

a BRDF-normalization step in its processing, any other product used for addressing the calibration inconsistencies of the LTDR should also account for this. Fortunately, methods to achieve this in rather simple ways already exist [17].

This chapter presents a method to assess calibration inconsistencies present in the LTDR. This method is based on a novel approach, that uses pattern-matching techniques, for the automatic selection of stable areas suitable for the intercalibration of remote sensors. The selected stable areas are then used to derive calibration coefficients for all AVHRR instruments in the LTDR and recalibrate the data record. Finally, the results from this recalibration are evaluated with the methodology developed in Chapter 2. Section 4.3 describe the data and materials used in this chapter. Section 4.4 presents the methodology. Section 4.5 presents the results 4.5 which are discussed in Section 4.6. Finally, section 4.7 gives the chapter conclusions.

4.3   Data

4.3.1   AVHRR Surface Reflectance

In this study, we analyzed the calibration inconsistencies present in the AVHRR surface reflectance Long Term Data Record (LTDR) [8]. The LTDR is generated from L1b GAC data from 7 AVHRR instruments between 1981 to present day. Data from the LTDR provides daily BRDF-normalized observations at spatial resolution of 0.05°x0.05° in the Climate Modeling Grid (CMG). The surface reflectance product includes information for 5 spectral channels, solar and view zenith angles, relative azimuth angles, and quality assessment. For this study, we use surface reflectance

from the red (0.58-0.68 µm) and near infrared (0.72-1.10 µm) channels, and the quality layer, which was used to remove pixels contaminated by clouds or other atmospheric effects and analyze only those with the highest quality. The AVHRR surface reflectance products were obtained from the LTDR project website[1].

4.3.2   MODIS Surface Reflectance

Red and near-infrared surface reflectance from MODIS Aqua Collection 6 were used in the study for evaluating the calibration of AVHRR. The MODIS MYD09CMG Collection 6 product provides surface reflectance images on 7 channels between 450 and 2100 nm at a spatial resolution of 0.05°x0.05°) in the same grid as AVHRR. The surface reflectance from MODIS was evaluated by [28], who reported uncertainties lower than $0.005 + 0.05\rho$. In this study, we normalized the MODIS BRDF using the method explained in Section 2.4.3.

4.3.3   Hyperion Surface Reflectance Spectra

Spectral band adjustment factors (SBAF) between AVHRR and MODIS Aqua were derived from a set of more than 100,000 hyperspectral surface reflectance spectra acquired by the Hyperion (H0) spectrometer onboard the Earth Observer-1 (EO-1) satellite[2].

---

[1]https://ltdr.modaps.eosdis.nasa.gov
[2]Note that this is the same dataset used in Chapter 2.

4.3.4 Relative Spectral Responses

Relative spectral responses (RSR) from AVHRR and MODIS were used to spectrally convolve the H0 surface reflectance spectra and derive spectral adjustment factors in a similar way to the method explained in Section 2.4.4. The RSR's for MODIS and every AVHRR instrument int the record was obtained from the NASA Langley cloud and radiation research webpage[3].

4.4 Method

4.4.1 Global selection of Stable Sites

In this study we propose a method for the automatic selection of stable sites (i.e., pixels) that are suitable for characterizing the calibration inconsistencies present in the LTDR. The automatic selection method is based on a reference temporal profile and on a similarity metric.

4.4.1.1 Definition of reference temporal profile

To find stable sites using the AVHRR data we began by defining a reference temporal profile. AVHRR surface reflectance shows temporal variations in the signal that are not representative of changes in the surface of Earth but are generated by sensor degradation and calibration issues. To account for this, we based our metric to find stable targets, on the temporal profile of the Red to Near-Infrared surface

---

[3]https://cloudsway2.larc.nasa.gov

reflectance ratio anomaly. The reference temporal profile was generated from observations of 8 stable sites (Table 4.1) over the entire AVHRR record. These sites were selected because their spatiotemporal variability and atmospheric conditions has been previously analyzed by several studies and found suitable for the intercalibration of satellite instruments [15, 22, 99, 100, 105].

Site	Latitude	Longitude	Type
DomeC	75.102	123.395	Snow
Libya4	28.55	23.39	Desert
Niger1	19.67	9.81	Desert
Saharan	21.5	14.4	Desert
Sudan1	21.74	28.22	Desert
Arabia1	18.88	46.76	Desert
Libya1	24.42	13.35	Desert

Table 4.1: Reference calibration sites.

A profile of the Red to Near-Infrared ratio temporal anomaly (Figure 4.1) was computed independently for each site and averaged to derive the reference profile used to automatize the selection of sites globally.

4.4.1.2   Automatic selection of stable sites

The method for automatic selection of stable sites, is based on measuring the similarity between the reference profile computed in the previous section, with that of other land pixels. There are numerous techniques designed to extract patterns and measure the similarity between time series [106, 107]. For this study, we selected the Dynamic Time Warping (DTW) distance [108], a well-known metric used to quantify the similarity between two or more sequences.
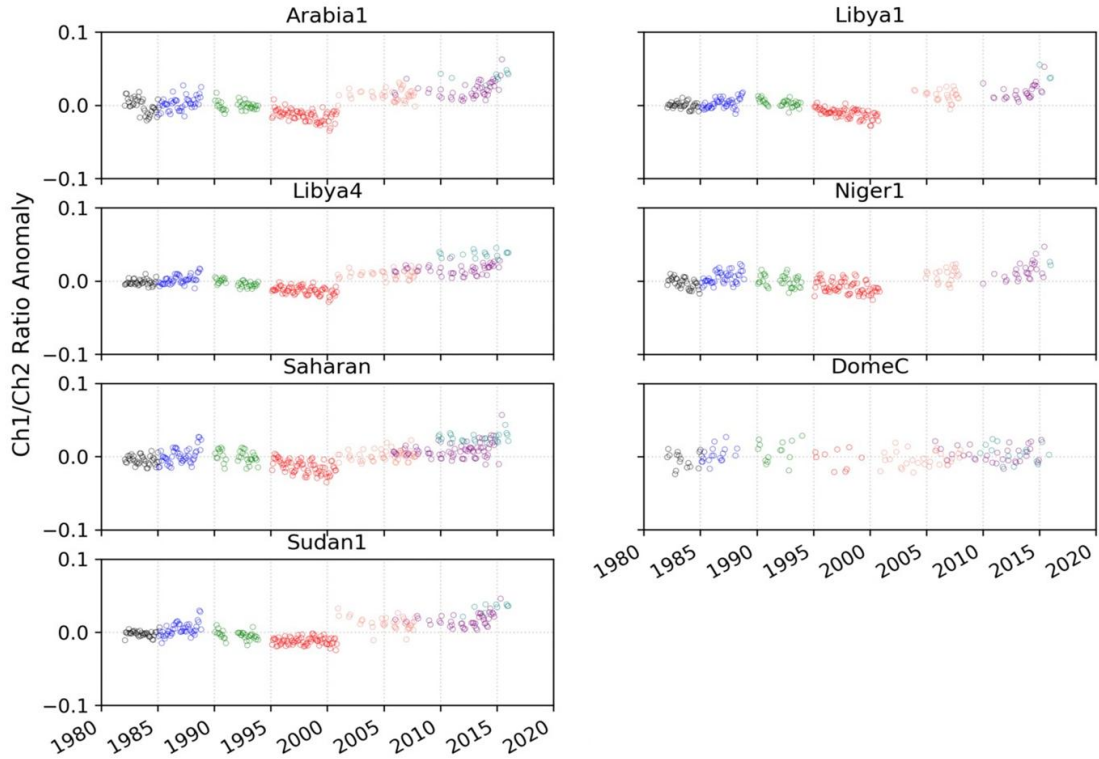
Figure 4.1: Temporal anomaly of the Red/NIR ratio.

We selected the DTW as a similarity metric because it is suitable for use on time series with missing observations and has been shown to be one of the fastest [109] and better performing techniques for the identification of pattern in data series [110].

4.4.2 Reference Surface Reflectance Climatology

To get a reference value against which to compare the surface reflectance from AVHRR we computed the MODIS Aqua BRDF-corrected surface reflectance per-pixel climatology (2002-2016) for each stable site selected by the DTW distance metric. The climatology was calculated from all cloud and shadow free pixels with an aerosol optical depth lower than 0.6.

4.4.3 Spectral Adjustment between the AVHRR and MODIS

The method used to derive spectral adjustment factors (SBAF) is similar to the one presented in Section 2.4.4 and is omitted here for brevity. However, for this study we fitted the SBAFs between MODIS and AVHRR to the NDVI from AVHRR using the double exponential model described in Equation 4.1:

$$SBAF_{\frac{Reference}{AVHRR}} = a \cdot exp(b \cdot NDVI_{AVHRR}) + c \cdot exp(d \cdot NDVI_{AVHRR}) \qquad (4.1)$$

The double exponential model was selected because it has been shown to best represent the spectral relationship between AVHRR and MODIS Red and NIR bands [6].

4.4.4 Derivation of Recalibration Coefficients

At each stable site we computed the ratio between the MODIS climatological value and the corresponding AVHRR Red and NIR surface reflectances. These ratios are what we refer to as "recalibration coefficients". To obtain an equation useful for the recalibration of the entire record, we fitted the 3-month averaged ratios to the number of days that each NOAA platform had been in orbit at the time of the observation. This type of fit is useful for characterizing signal changes due to sensor and orbit degradation [14, 22, 111]. Finally, to evaluate the impact of the recalibration coefficients on the LTDR, we replicated the evaluation presented in Chapter 2 with the recalibrated record.

4.5 Results

4.5.1 Global selection of stable sites

Figure 4.2 shows the stable areas selected using the DTW method.
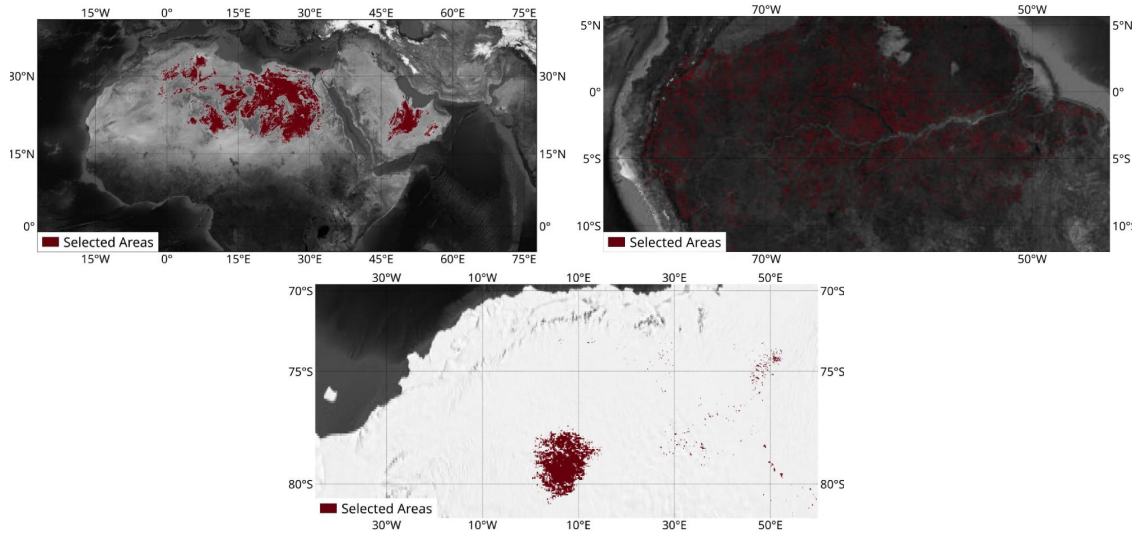
Figure 4.2: Areas selected by the DTW distance method.

The approach, based on a reference time series and the DTW method generated a selection of pixels over North Africa, the South Pole, and the Amazon forest. The majority of selected pixels was found over bare ground or snow areas which are similar to the surfaces of the sites used to generate the reference time series.

4.5.2   Spectral Adjustment

Figure 4.3 shows the resulting fit and spectra adjustment coefficients for MODIS/AVHRR.
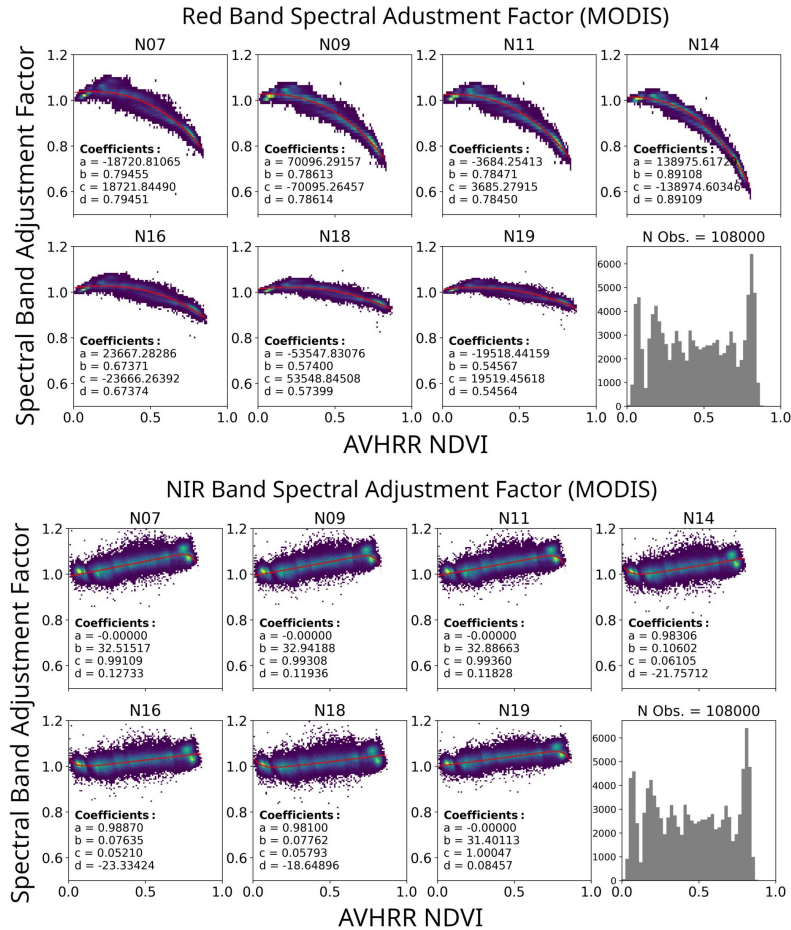
Figure 4.3: Spectral Band Adjustment Factors between AVHRR and MODIS. The histogram shows the distribution of NDVI values from MODIS.

There is a noticeable difference between the SBAFs for the Red and NIR bands. The SBAFs for the Red band tend to decrease in value when the NDVI increases, and this dependence is noticeable stronger for N07-N14 than for N16-N19. In contrast, the NIR band SBAFS tend to increase with the NDVI and show a more consistent behavior.

4.5.3 Calibration Coefficients

Figure 4.4 shows the computed recalibration coefficients for the Red band as a function of the days that each platform has been in orbit. Each plot shows the linear and quadratic fits.
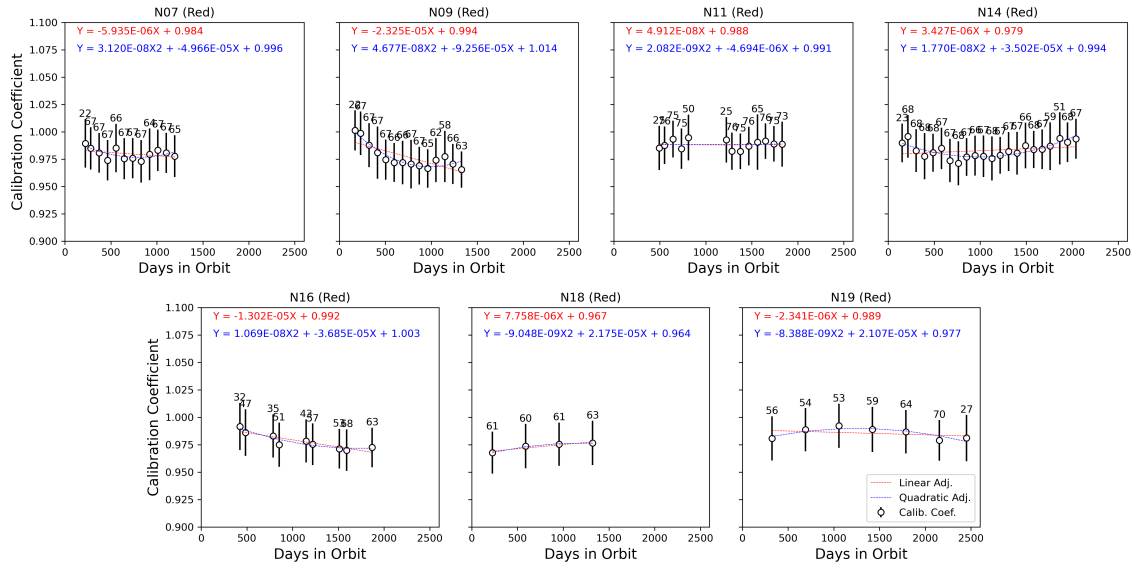
Figure 4.4: Recalibration coefficients for AVHRR Red band. The markers represent 3-month mean and standard deviation. Numbers on top of each marker show the number of observations in thousands. The gap in N11 values is due to the eruption of Mt. Pinatubo in 1991.

The recalibration coefficients for the Red band were generally smaller than unity. Results for N11 showed the smallest calibration slope, which suggest a more stable calibration of the instrument. In contrast, N09 showed the largest calibration slope. For most cases, the temporal variation of the coefficients was better represented by a quadratic fit. However, for N11, N16 and N18 there was little difference between the linear and quadratic methods. Some of the coefficients showed a small seasonality, which was more evident for the N07 and N14. Figure 4.5 shows the recalibration coefficients for the NIR band.
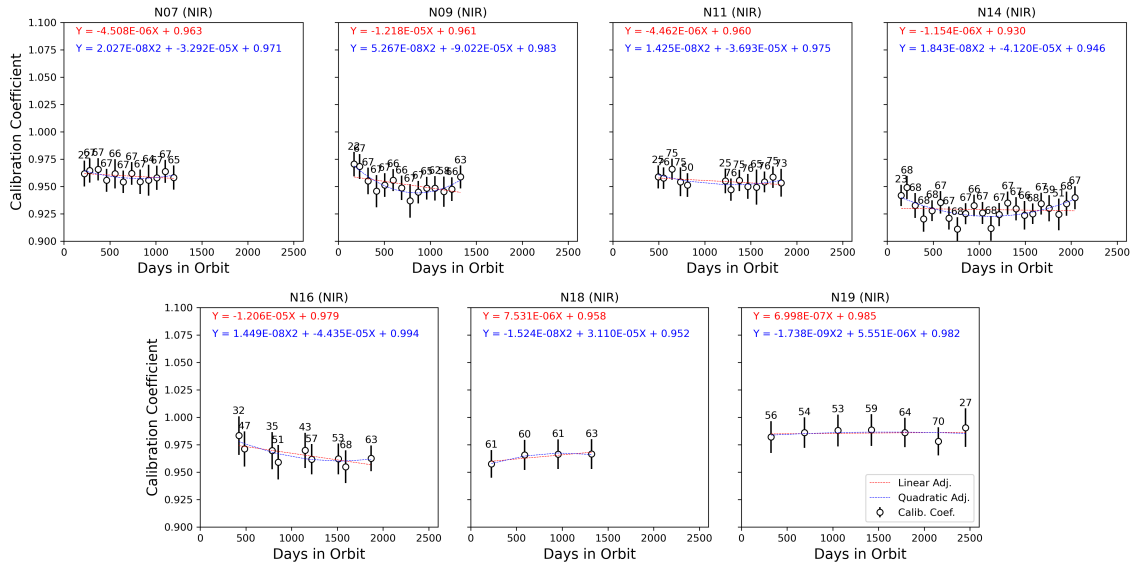
Figure 4.5: Recalibration coefficients for AVHRR Red band. The markers represent 3-month mean and standard deviation. Numbers on top of each marker show the number of observations in thousands. The gap in N11 values is due to the eruption of Mt. Pinatubo in 1991.

Results for the NIR band are similar to the Red band. The calibration coefficients were smaller than unity and their temporal variation was generally better represented by a quadratic fit. In the following section, we evaluate the LTDR recalibration using the quadratic coefficients.

4.5.4 Evaluation of the Recalibrated LTDR

Table 4.2 shows the Red band APU metrics computed for the original LTDR and the recalibrated record (LTDR-I) using the quadratic coefficients.

| | Red Band | | | | | |
| | Accuracy | | Precision | | Uncertainty | |
	LTDR	**LTDRI-I**	**LTDR**	**LTDR-I**	**LTDR**	**LTDR-I**
N07	0.001	-0.001	0.019	0.020	0.020	0.020
N09	0.004	0.001	0.017	0.017	0.018	0.017
N11	-0.001	-0.002	0.016	0.016	0.016	0.017
N14	0.002	0.000	0.017	0.016	0.017	0.016
N16	0.002	-0.001	0.016	0.016	0.016	0.016
N18	0.004	0.001	0.015	0.015	0.015	0.015
N19	0.005	0.003	0.012	0.012	0.014	0.013

Table 4.2: Red APU for the original (LTDR) and recalibrated (LTDR-I) record.

Results of the Red band recalibration were generally positive, albeit small. Except for N11, the accuracy for all instruments improved after the recalibration. The largest accuracy improvements were shown for N09 and N07 (0.004 to 0.001). Changes in uncertainty reached 5% and were mostly due to accuracy improvements, as the precision was mostly unchanged. Results for the NIR are shown in Table 4.3.

| | NIR Band | | | | | |
| | Accuracy | | Precision | | Uncertainty | |
	LTDR	**LTDRI-I**	**LTDR**	**LTDR-I**	**LTDR**	**LTDR-I**
N07	-0.008	-0.019	0.027	0.026	0.028	0.032
N09	-0.003	-0.008	0.026	0.025	0.027	0.027
N11	-0.004	-0.014	0.022	0.021	0.022	0.026
N14	0.014	-0.004	0.024	0.022	0.028	0.022
N16	0.010	0.002	0.022	0.021	0.024	0.021
N18	0.010	0.001	0.021	0.020	0.023	0.020
N19	0.006	0.001	0.019	0.019	0.020	0.019

Table 4.3: NIR APU for the original (LTDR) and recalibrated (LTDR-I) record.

Results for the NIR band were mixed. For the instruments on N07-N14, the accuracy decreased after the recalibration, with N07 showing the worst results (from -0.008 to -0.019). For N14-N16 the situation was different, with a considerable accuracy improvement in all cases. The largest accuracy improvements after the recalibration were show by N14 (0.014 to -0.004) and N18 (0.010 to 0.001). Changes in uncertainty ranged between 5% for N19 to 22% for N14. As with the Red band, the precision was mostly unchanged. Figure 4.6 shows the relative change in the Red and NIR bands uncertainty for all instruments. The APU graphs for the recalibrated record are shown in Appendix B.
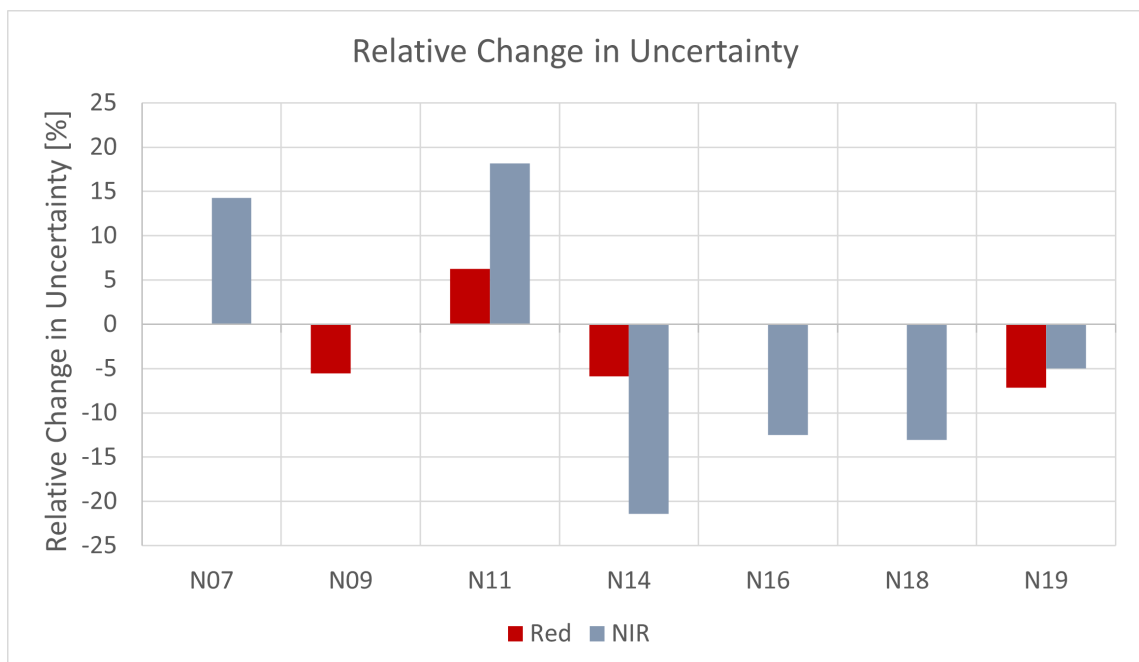
Figure 4.6: Relative change in uncertainty after surface reflectance recalibration.

4.6   Discussion

In this chapter, we proposed an approach to address calibration inconsistencies in the LTDR. The proposed approach used a novel method based on a pattern-matching algorithm (DTW) to drive the automated selection of stable areas suitable for sensor intercalibration. The areas selected by the pattern-matching algorithm were then used to derive recalibration coefficients for the LTDR. This was done by comparing the surface reflectance from spectrally adjusted AVHRR with a climatological value derived from MODIS Aqua BRDF-normalized reflectance.

The areas selected by the automatic method correspond to well-known calibrated targets (deserts, permanent snow), which shows the good performance of the pattern-matching algorithms as a method to identify surfaces from reference time-series. In fact, numerous studies have also taken advantage of the DTW method for Land-Use and Land-Cover mapping and classification [102, 103]. Moreover, the selection of forest areas agreed with calibration methods previously proposed [10].

The spectral adjustment factors derived in this study were an important step for the appropriate recalibration of the LTDR. Specially for the forest areas, since larger NDVI values show the largest spectral differences between AVHRR and MODIS Aqua.

The recalibration coefficients showed that the LTDR surface reflectance has a positive bias when compared to the climatological value from MODIS Aqua. The coefficients generally showed a quadratic relationship with the number of days that each platform has been in orbit. It is important to note that these results do

not necessarily represent issues in the AVHRR instruments, and they are more likely accounting for small variations not entirely addressed by the initial LTDR calibration, or by artifacts introduced during the LTDR processing steps. However, it is important not to forget that calibration issues are many times worse before being corrected by the LTDR absolute calibration.

The evaluation of the recalibrated record showed good results. The Red band showed improvements in accuracy for most of the instruments (up to 5%). In contrast, changes in the NIR band accuracy after calibration were more noticeable (up to 22%). The large accuracy improvements of N14-N19 (0.005-0.01) showed that the method developed in this chapter will contribute to a more consistent LTDR record. The reduced performance of N07-N11 should be further looked into, but results suggest that the recalibration issues could be generated by water vapor effects not accounted in the atmospheric correction due to the coarse resolution products used. This issue might be solved by implementing the AVHRR water vapor retrieval approach presented in Chapter 3. Furthermore, a new method to define the reference time series used by the patter-matching algorithm, based in the temporal profile of high-altitude bright clouds, is currently being researched and may provide further improvements.

4.7   Conclusions

This chapter presented a novel approach to assess and correct the calibration uncertainties present in the LTDR. Our proposed method was based on reference

time series from 8 well-characterized stable sites to drive a pattern-match algorithm and automatically select areas suitable for the intercalibration of AVHRR spectral bands. The stable sites where then used to derive recalibration coefficients by comparing the AVHRR observations to a climatological value from MODIS Aqua. Evaluation of the recalibrated LTDR was promising and showed the potential of the proposed method to improve the calibration of the LTDR and minimize the consistency issues.

Chapter 5:   Conclusions

5.1   Summary of Findings and Impact of Research

The main objective of this dissertation was to advance the development of the AVHRR surface reflectance LTDR. This section summarizes the main findings of this dissertation and how they might impact both the community of LTDR data users and the LTDR future development.

First, in Chapter 2 a method was proposed for the comprehensive evaluation of the LTDR surface reflectance performance, and the characterization of its uncertainties. The method used same-day observations from Landsat TM5 as a reference dataset, the VJB BRDF-normalization method to account for differences in observation geometry, and spectral adjustment factors to harmonize both sensors' spectral behavior. The LTDR performance was evaluated in terms of accuracy, precision, and uncertainty metrics and compared to a target specification.

The evaluation showed that the overall performance of the LTDR is close to the target specification of $0.071\rho + 0.0071$. In general, the more recent AVHRR instruments performed better. The temporal analysis of uncertainties showed an increasing trend during the lifetime of N07-N14 that was not present for N16-N19. This increase in uncertainty was mainly attributed to orbital drift effects present

in the earlier AVHRR instruments of the LTDR. Moreover, the seasonal analysis showed no significant variation between seasons in either the Northern or Southern Hemisphere. The spatial distribution of uncertainties was similar for all AVHRR instruments, with the largest uncertainties found over forests in high latitudes and tropical regions. A strong correlation was found between the relative errors of the Red and NIR bands over barren (R^2>0.8) and sparsely vegetated (R^2>0.5) areas.

These results provide the first comprehensive evaluation of the LTDR, which is valuable to data users and the LTDR development team. This evaluation will help users better understand the potential and limitations of the record for their particular studies and address them as needed. Furthermore, LTDR users now can include uncertainty estimates, which are will improve correct interpretation of their research results. The LTDR development team also benefits from this evaluation, as the assessment of the product's spatiotemporal performance provides insight on potential issues in the production of the data record.

Next, Chapter 3 presents a method to derive water vapor content from the AVHRR observations and provide better input information for the LTDR atmospheric correction. The proposed method relied on near-coincident observations from AVHRR N19 and MODIS Aqua to calibrate local split-window coefficients globally. Moreover, spectral adjustment factors made it possible to use the coefficients derived for N19 on other AVHRR instruments, which allowed the retrieval of water vapor from AVHRR for the pre-MODIS era.

The water vapor estimates from N16-N19 were validated against measurements from globally-distributed AERONET sunphotometers with good results (R^2>0.75;

95

RMSE<$0.45g \cdot cm^{-2}$). Moreover, the estimates from AVHRR were evaluated globally on a per-pixel basis using near-coincident total column water vapor from MODIS Aqua. This evaluation showed good performance of the estimates globally, with an error lower than $0.50g \cdot cm^{-2}$, with the exception of some tropical areas.

To evaluate the potential use of AVHRR water vapor for the atmospheric correction of the Red and NIR bands, a dataset of over 500,000 AVHRR TOA observations was atmospherically corrected using the water vapor estimates from AVHRR and compared to values corrected with MODIS water vapor. Results for the NIR band (which is impacted by absorption from atmospheric water vapor) showed good agreement between the surface reflectance derived using water vapor from AVHRR and the values corrected using MODIS water vapor (R^2=0.99; RMSE=0.01; Bias=0.003).

The derived global split-window coefficients will allow the LTDR team to estimate water vapor for the atmospheric correction directly from the instrument that measures the surface reflectance. At least in theory, this will enable the generation of better and more consistent surface reflectance values than the current ones obtained from coarse resolution atmospheric products. Furthermore, if the atmospheric correction is improved, users of LTDR data will directly benefit from surface reflectance estimates that better represent the land surface.

Finally, Chapter 4 proposed an approach to address calibration inconsistencies in the LTDR. The proposed approach used a novel method based on the Dynamic Time Warping metric to drive the automated selection of globally distributed stable areas. The areas selected by the DTW-based method were then used to derive

calibration coefficients for the LTDR. This was done by comparing the 3-month average surface reflectance from spectrally adjusted AVHRR observation with a climatological value derived from MODIS Aqua BRDF-normalized reflectance.

Evaluation of the recalibrated LTDR showed good results, with improvements in uncertainty that reached 5% for the Red band and varied between 5% to 22% for the NIR. Results for N07 and N09 NIR band showed an uncertainty increase after the recalibration. This was attributed to water vapor effects not accounted in the atmospheric correction due to the currently used coarse resolution products. These findings provide valuable information for the LTDR development team and a further step towards the improved calibration of the surface reflectance record.

5.2   Future Research

In this dissertation, the LTDR evaluation was based on an inter-comparison with surface reflectance values from TM5, a product with quantified performance and uncertainties. This type of inter-comparison is well established in the literature as a way to evaluate or inter-calibrate remote sensors. However, evaluation of surface reflectance derived from satellite observations is a topic for continued development. In this context, it is interesting to research novel alternatives for the validation of satellite measurements. To this end, I am currently part of a team developing such an alternative. Our approach employs ground-based multi-spectral cameras for the continuous measurement of surface reflectance and characterization of representative sites. While the system is still in development, initial results show promise [112].

97

This type of system could provide a good source of reference data to evaluate surface reflectance from high and very-high resolution instruments.

Regarding the water vapor retrieval method from the AVHRR, while the original purpose of the estimates was to generate better input data for the LTDR atmospheric corrections, it is interesting to investigate if they might prove useful in other research areas. For example, estimates from AVHRR can be used to extend the water vapor record from MODIS to the early 1980s, practically doubling its current length. This information could be highly interesting for the atmospheric research community and help provide a better understanding of water vapor spatiotemporal-temporal variability [113]. However, before the water vapor estimates from AVHRR can be used for scientific research, a comprehensive evaluation that provides uncertainty information for the entire period should be carried out. Moreover, the orbital drift of NOAA platforms could provide a significant complication for long-term analysis. Nevertheless, this is an exciting topic for future research.

Furthermore, the LTDR current atmospheric correction approach does not account for the effect of stratospheric and tropospheric aerosols, which can be a large source of uncertainty. However, retrieving aerosols over land from AVHRR data is a complex task due to the small number of spectral bands. Numerous studies have proposed methods for the estimation of aerosol optical depth over land surfaces, however most of them are limited to specific surfaces where the surface reflectance can be accurately modeled for the aerosol inversion. In terms of global estimation, the Deep Blue algorithm developed for the Sea-viewing Wide Field-of-View satellite was adapted to AVHRR and could be an interesting alternative [11].

However, recent studies showed that it frequently underestimates the AOT over bright surfaces [114]. It would be interesting to undertake research on this topic in the future from the perspective of the LTDR, for example by taking advantage of the middle-infrared reflectance generated in the data record [115].

5.3 Conclusion

The LTDR project has been in continuous development for more than fifteen years. In that time, the LTDR has gone through numerous changes, which have been motivated by advances in processing techniques, retrieval algorithms, instrument changes, and more. This interest for constant improvement is motivated by the idea that AVHRR, even with all its technical limitations by today's technological standards, provides a unique opportunity to study our planet. That idea also motivated this dissertation, with the goal of contributing to this ambitious research agenda to create a unique data record of the land surface and advance the development of the AVHRR Surface Reflectance LTDR. Increasing attention to the effects of climate change on the Earth's surface will require quantitative approaches to measuring and assess such change. The LTDR could play an important role in assessing such changes.

Appendix A: LTDR Recalibration Coefficients

Instrument	Band	Intercept	Slope	Quadratic Slope
N07	RED	0.996	-4.97E-05	3.12E-08
N09	RED	1.014	-9.26E-05	4.68E-08
N11	RED	0.991	-4.69E-06	2.08E-09
N14	RED	0.994	-3.50E-05	1.77E-08
N16	RED	1.001	-3.72E-05	1.14E-08
N18	RED	0.965	1.37E-05	-3.28E-09
N19	RED	0.976	2.20E-05	-8.82E-09
N07	NIR	0.971	-3.29E-05	2.03E-08
N09	NIR	0.983	-9.02E-05	5.27E-08
N11	NIR	0.975	-3.69E-05	1.43E-08
N14	NIR	0.946	-4.12E-05	1.84E-08
N16	NIR	0.990	-4.67E-05	1.71E-08
N18	NIR	0.953	2.28E-05	-9.03E-09
N19	NIR	0.978	1.21E-05	-4.45E-09

Table A.1: Quadratic Recalibration Coefficients

Instrument	Band	Intercept	Slope
N07	RED	0.984	-5.94E-06
N09	RED	0.994	-2.33E-05
N11	RED	0.988	4.91E-08
N14	RED	0.979	3.43E-06
N16	RED	0.990	-1.18E-05
N18	RED	0.967	7.50E-06
N19	RED	0.990	-3.68E-06
N07	NIR	0.963	-4.51E-06
N09	NIR	0.961	-1.22E-05
N11	NIR	0.960	-4.46E-06
N14	NIR	0.930	-1.15E-06
N16	NIR	0.973	-8.53E-06
N18	NIR	0.959	5.75E-06
N19	NIR	0.985	-8.52E-07

Table A.2: Linear Recalibration Coefficients

Appendix B: APU of Recalibrated LTDR

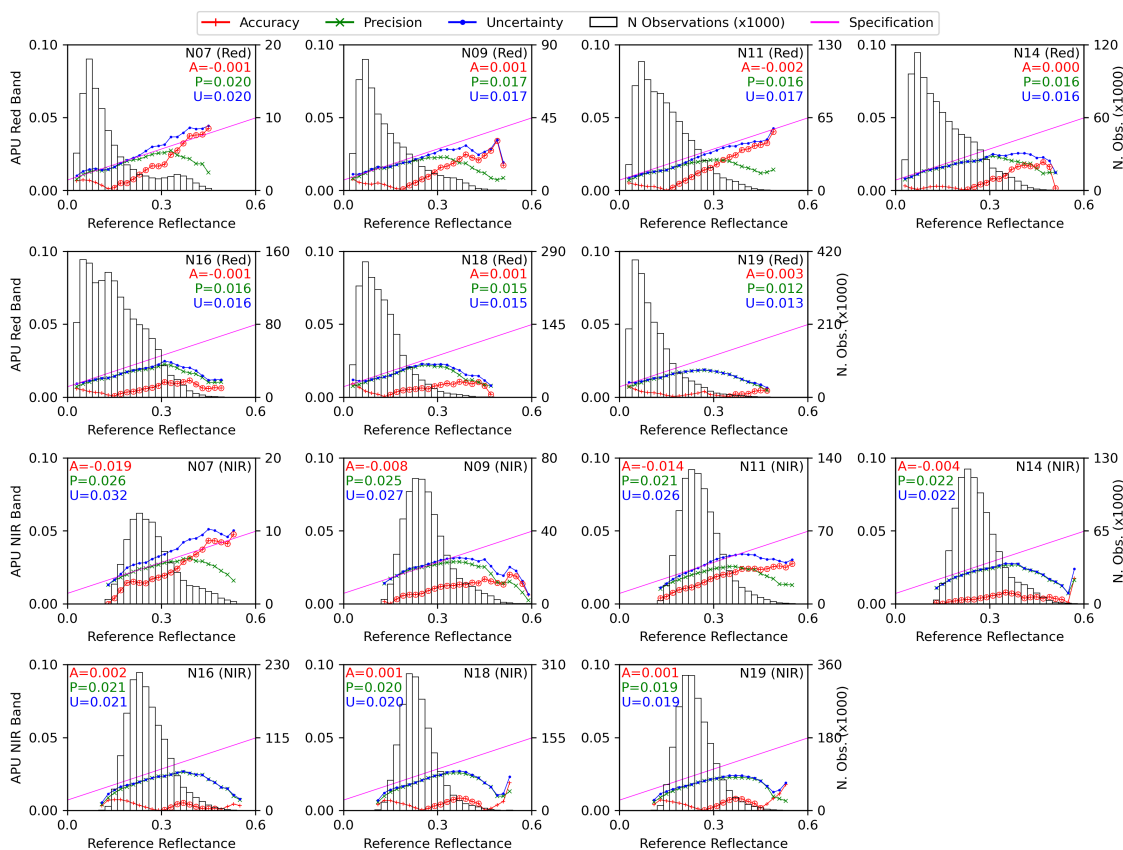Figure B.1 shows the APU graphs[1] for the recalibrated surface reflectance record.

Figure B.1: Accuracy (A), Precision (P), and Uncertainty (U) of the LTDR after the Surface Reflectance Recalibration. Details of the graphs are given on the caption of Figure 2.6.

---

[1]For details check on how the APU are computed, check Section 2.4.5.

Bibliography

[1] P. Potapov, S. Turubanova, A. Tyukavina, A. Krylov, J. McCarty, V. Radeloff, and M. Hansen, "Eastern Europe's forest cover dynamics from 1985 to 2012 quantified from the full Landsat archive," *Remote Sensing of Environment*, vol. 159, pp. 28–43, 2015. [Online]. Available: https://doi.org/10.1016%2Fj.rse.2014.11.027

[2] S. Skakun, N. Kussul, A. Shelestov, and O. Kussul, "The use of satellite data for agriculture drought risk quantification in Ukraine," *Geomatics, Natural Hazards and Risk*, vol. 7, no. 3, pp. 901–917, 2015. [Online]. Available: https://doi.org/10.1080%2F19475705.2015.1016555

[3] X.-P. Song, M. C. Hansen, S. V. Stehman, P. V. Potapov, A. Tyukavina, E. F. Vermote, and J. R. Townshend, "Global land change from 1982 to 2016," *Nature*, vol. 560, no. 7720, pp. 639–643, 2018. [Online]. Available: https://doi.org/10.1038%2Fs41586-018-0411-9

[4] X. Zhang, "Reconstruction of a complete global time series of daily vegetation index trajectory from long-term AVHRR data," *Remote Sensing of Environment*, vol. 156, pp. 457–472, 2015. [Online]. Available: https://doi.org/10.1016%2Fj.rse.2014.10.012

[5] S. Kalluri, C. Cao, A. Heidinger, A. Ignatov, J. Key, and T. Smith, "The advanced very high resolution radiometer: Contributing to earth observations for over 40 years," *Bulletin of the American Meteorological Society*, vol. 102, no. 2, pp. E351–E366, 2021. [Online]. Available: https://doi.org/10.1175%2Fbams-d-20-0088.1

[6] J. L. Villaescusa-Nadal, B. Franch, J.-C. Roger, E. F. Vermote, S. Skakun, and C. Justice, "Spectral Adjustment Model's Analysis and Application to Remote Sensing Data," *IEEE Journal of Selected Topics in Applied Earth Observations and Remote Sensing*, vol. 12, no. 3, pp. 961–972, 2019. [Online]. Available: https://doi.org/10.1109%2Fjstars.2018.2890068

[7] J. Pedelty, S. Devadiga, E. Masuoka, M. Brown, J. Pinzon, C. Tucker, E. Vermote, S. Prince, J. Nagol, C. Justice, D. Roy, J. Ju, C. Schaaf, J. Liu, J. Privette, and A. Pinheiro, "Generating a long-term land data record from the AVHRR and MODIS instruments," in *2007 IEEE International Geoscience and Remote Sensing Symposium.* IEEE, 2007. [Online]. Available: https://doi.org/10.1109%2Figarss.2007.4422974

[8] B. Franch, E. Vermote, J.-C. Roger, E. Murphy, I. Becker-Reshef, C. Justice, M. Claverie, J. Nagol, I. Csiszar, D. Meyer, F. Baret, E. Masuoka, R. Wolfe, and S. Devadiga, "A 30+ Year AVHRR Land Surface Reflectance Climate Data Record and Its Application to Wheat Yield Monitoring," *Remote Sensing*, vol. 9, no. 3, p. 296, 2017. [Online]. Available: https://doi.org/10.3390%2Frs9030296

[9] J. Robel and A. Graumann, "NOAA KLM user's guide," 2014. [Online]. Available: https://www.star.nesdis.noaa.gov/mirs/documents/0. 0_NOAA_KLM_Users_Guide.pdf

[10] Z. Song, S. Liang, D. Wang, Y. Zhou, and A. Jia, "Long-term record of top-of-atmosphere albedo over land generated from AVHRR data," *Remote Sensing of Environment*, vol. 211, pp. 71–88, 2018. [Online]. Available: https://doi.org/10.1016%2Fj.rse.2018.03.044

[11] N. C. Hsu, J. Lee, A. M. Sayer, N. Carletta, S.-H. Chen, C. J. Tucker, B. N. Holben, and S.-C. Tsay, "Retrieving near-global aerosol loading over land and ocean from AVHRR," *J. Geophys. Res. Atmos.*, vol. 122, no. 18, pp. 9968–9989, sep 2017. [Online]. Available: https://doi.org/10.1002%2F2017jd026932

[12] A. M. Sayer, N. C. Hsu, J. Lee, N. Carletta, S.-H. Chen, and A. Smirnov, "Evaluation of NASA deep blue/SOAR aerosol retrieval algorithms applied to AVHRR measurements," *J. Geophys. Res. Atmos.*, vol. 122, no. 18, pp. 9945–9967, sep 2017. [Online]. Available: https://doi.org/10.1002%2F2017jd026934

[13] M. Claverie, J. Matthews, E. Vermote, and C. Justice, "A 30+ Year AVHRR LAI and FAPAR Climate Data Record: Algorithm Description and Validation," *Remote Sensing*, vol. 8, no. 3, p. 263, 2016. [Online]. Available: https://doi.org/10.3390%2Frs8030263

[14] E. Vermote and Y. Kaufman, "Absolute calibration of AVHRR visible and near-infrared channels using ocean and cloud views," *International Journal of Remote Sensing*, vol. 16, no. 13, pp. 2317–2340, 1995. [Online]. Available: https://doi.org/10.1080%2F01431169508954561

[15] E. Vermote and N. Saleous, "Calibration of NOAA16 AVHRR over a desert site using MODIS data," *Remote Sensing of Environment*, vol. 105, no. 3, pp. 214–220, 2006. [Online]. Available: https: //doi.org/10.1016%2Fj.rse.2006.06.015

[16] E. Vermote, D. Tanre, J. Deuze, M. Herman, and J.-J. Morcette, "Second Simulation of the Satellite Signal in the Solar Spectrum, 6S: an overview," *IEEE Transactions on Geoscience and Remote Sensing*, vol. 35, no. 3, pp. 675–686, 1997. [Online]. Available: https://doi.org/10.1109%2F36.581987

[17] E. Vermote, C. Justice, and F.-M. Breon, "Towards a Generalized Approach for Correction of the BRDF Effect in MODIS Directional Reflectances," *IEEE Transactions on Geoscience and Remote Sensing*, vol. 47, no. 3, pp. 898–908, 2009. [Online]. Available: https://doi.org/10.1109%2Ftgrs.2008.2005977

[18] E. Vermote and M. Claverie, "Climate Algorithm Theoretical Basis Document (C-ATBD) AVHRR Land Bundle - Surface Reflectance and Normalized Difference Vegetation Index," 2018. [Online]. Available: https://www.ncei.noaa.gov/pub/data/sds/cdr/CDRs/AVHRR%20Surface%20Reflectance/AlgorithmDescription_01B-20a.pdf

[19] P. Teillet, P. Slater, Y. Ding, R. Santer, R. Jackson, and M. Moran, "Three methods for the absolute calibration of the NOAA AVHRR sensors in-flight," *Remote Sensing of Environment*, vol. 31, no. 2, pp. 105–120, 1990. [Online]. Available: https://doi.org/10.1016/0034-4257(90)90060-y

[20] R. Frouin and C. Gautier, "Calibration of NOAA-7 AVHRR, GOES-5, and GOES-6 VISSR/VAS solar channels," *Remote Sensing of Environment*, vol. 22, no. 1, pp. 73–101, 1987. [Online]. Available: https://doi.org/10.1016%2F0034-4257%2887%2990028-9

[21] A. K. Heidinger, C. Cao, and J. T. Sullivan, "Using moderate resolution imaging spectrometer (MODIS) to calibrate advanced very high resolution radiometer reflectance channels," *Journal of Geophysical Research*, vol. 107, no. D23, pp. AAC 11–1–AAC 11–10, 2002. [Online]. Available: https://doi.org/10.1029%2F2001jd002035

[22] R. Bhatt, D. R. Doelling, B. R. Scarino, A. Gopalan, C. O. Haney, P. Minnis, and K. M. Bedka, "A consistent AVHRR visible calibration record based on multiple methods applicable for the NOAA degrading orbits. part i: Methodology," *Journal of Atmospheric and Oceanic Technology*, vol. 33, no. 11, pp. 2499–2515, 2016. [Online]. Available: https://doi.org/10.1175%2Fjtech-d-16-0044.1

[23] L. Giglio and D. Roy, "On the outstanding need for a long-term, multi-decadal, validated and quality assessed record of global burned area: Caution in the use of Advanced Very High Resolution Radiometer data," *Science of Remote Sensing*, vol. 2, p. 100007, 2020. [Online]. Available: https://doi.org/10.1016%2Fj.srs.2020.100007

[24] E. Vermote and D. Tanré, "Analytical expressions for radiative properties of planar rayleigh scattering media, including polarization contributions,"

Journal of Quantitative Spectroscopy and Radiative Transfer, vol. 47, no. 4, pp. 305–314, 1992. [Online]. Available: https://doi.org/10.1016/0022-4073(92)90149-x

[25] S. Y. Kotchenova, E. F. Vermote, R. Matarrese, and F. J. Klemm, Jr., "Validation of a vector version of the 6S radiative transfer code for atmospheric correction of satellite data. Part I: Path radiance," *Applied Optics*, vol. 45, no. 26, p. 6762, 2006. [Online]. Available: https://www.osapublishing.org/abstract.cfm?URI=ao-45-26-6762

[26] S. Y. Kotchenova and E. F. Vermote, "Validation of a vector version of the 6S radiative transfer code for atmospheric correction of satellite data. Part II Homogeneous Lambertian and anisotropic surfaces," *Applied Optics*, vol. 46, no. 20, p. 4455, 2007. [Online]. Available: https://www.osapublishing.org/abstract.cfm?URI=ao-46-20-4455

[27] S. Y. Kotchenova, E. F. Vermote, R. Levy, and A. Lyapustin, "Radiative transfer codes for atmospheric correction and aerosol retrieval: intercomparison study," *Applied Optics*, vol. 47, no. 13, p. 2215, 2008. [Online]. Available: https://www.osapublishing.org/abstract.cfm?URI=ao-47-13-2215

[28] E. F. Vermote and S. Kotchenova, "Atmospheric correction for the monitoring of land surfaces," *Journal of Geophysical Research*, vol. 113, no. D23, 2008. [Online]. Available: https://doi.org/10.1029%2F2007jd009662

[29] E. F. Vermote and N. Saleous, *Operational Atmospheric Correction of MODIS Visible to Middle Infrared Land Surface Data in the Case of an Infinite Lambertian Target.* Springer Berlin Heidelberg, 2006, pp. 123–153. [Online]. Available: https://doi.org/10.1007/978-3-540-37293-6_8

[30] N. Z. El Saleous, E. F. Vermote, C. O. Justice, J. R. G. Townshend, C. J. Tucker, and S. N. Goward, "Improvements in the global biospheric record from the advanced very high resolution radiometer (AVHRR)," *International Journal of Remote Sensing*, vol. 21, no. 6-7, pp. 1251–1277, 2000. [Online]. Available: https://doi.org/10.1080/014311600210164

[31] B. C. Gao and Y. J. Kaufman, "Water vapor retrievals using Moderate Resolution Imaging Spectroradiometer (MODIS) near-infrared channels," *Journal of Geophysical Research: Atmospheres*, vol. 108, no. 13, pp. 1–10, 2003.

[32] C. G. Wellemeyer, P. K. Bhartia, S. L. Taylor, W. Qin, and C. Ahn, "Version 8 Total Ozone Mapping Spectrometer (TOMS) Algorithm," 2004.

[33] N. C. for Environmental Prediction (NCEP), "Global Data Assimilation System." [Online]. Available: https://www.nco.ncep.noaa.gov/pmb/products/gfs/

[34] E. Kalnay, M. Kanamitsu, R. Kistler, W. Collins, D. Deaven, L. Gandin, M. Iredell, S. Saha, G. White, J. Woollen, Y. Zhu, A. Leetmaa, R. Reynolds, M. Chelliah, W. Ebisuzaki, W. Higgins, J. Janowiak, K. C. Mo, C. Ropelewski, J. Wang, R. Jenne, D. Joseph, E. Kalnay, M. Kanamitsu, R. Kistler, W. Collins, D. Deaven, L. Gandin, M. Iredell, S. Saha, G. White, J. Woollen, Y. Zhu, M. Chelliah, W. Ebisuzaki, W. Higgins, J. Janowiak, K. C. Mo, C. Ropelewski, J. Wang, A. Leetmaa, R. Reynolds, R. Jenne, and D. Joseph, "The NCEP/NCAR 40-Year Reanalysis Project," *Bulletin of the American Meteorological Society*, vol. 77, no. 3, pp. 437–471, 1996. [Online]. Available: http://journals.ametsoc.org/doi/abs/10.1175/1520-0477{%}281996{%}29077{%}3C0437{%}3ATNYRP{%}3E2.0.CO{%}3B2

[35] F. Maignan, F.-M. Bréon, and R. Lacaze, "Bidirectional reflectance of Earth targets: evaluation of analytical models using a large set of spaceborne measurements with emphasis on the Hot Spot," *Remote Sensing of Environment*, vol. 90, no. 2, pp. 210–220, 2004. [Online]. Available: https://doi.org/10.1016%2Fj.rse.2003.12.006

[36] J.-L. Roujean, M. Leroy, and P.-Y. Deschamps, "A bidirectional reflectance model of the Earth's surface for the correction of remote sensing data," *Journal of Geophysical Research*, vol. 97, no. D18, p. 20455, 1992. [Online]. Available: https://doi.org/10.1029%2F92jd01411

[37] B. Franch, E. Vermote, and M. Claverie, "Intercomparison of Landsat albedo retrieval techniques and evaluation against in situ measurements across the US SURFRAD network," *Remote Sensing of Environment*, vol. 152, pp. 627–637, 2014. [Online]. Available: https://doi.org/10.1016%2Fj.rse.2014.07.019

[38] J. Villaescusa-Nadal, B. Franch, E. Vermote, and J.-C. Roger, "Improving the AVHRR Long Term Data Record BRDF Correction," *Remote Sensing*, vol. 11, no. 5, p. 502, 2019. [Online]. Available: https://doi.org/10.3390%2Frs11050502

[39] L. L. Stowe, P. A. Davis, and E. P. McClain, "Scientific basis and initial evaluation of the CLAVR-1 global clear/cloud classification algorithm for the advanced very high resolution radiometer," *Journal of Atmospheric and Oceanic Technology*, vol. 16, no. 6, pp. 656–681, 1999. [Online]. Available: https://journals.ametsoc.org/view/journals/atot/16/6/1520-0426_1999_016_0656_sbaieo_2_0_co_2.xml

[40] J. L. Villaescusa-Nadal, E. Vermote, B. Franch, A. Santamaría-Artigas, J.-C. Roger, and S. Skakun, "MODIS-Based AVHRR cloud and snow separation algorithm," *IEEE Transactions on Geoscience and Remote Sensing*, pp. 1–13, 2021.

[41] C. Li, Y. Xue, Q. Liu, J. Guang, X. He, J. Zhang, T. Wang, and X. Liu, "Post calibration of channels 1 and 2 of long-term AVHRR data

record based on SeaWiFS data and pseudo-invariant targets," *Remote Sensing of Environment*, vol. 150, pp. 104–119, 2014. [Online]. Available: https://doi.org/10.1016%2Fj.rse.2014.04.020

[42] A. Santamaría-Artigas, E. F. Vermote, B. Franch, J.-C. Roger, and S. Skakun, "Evaluation of the AVHRR surface reflectance long term data record between 1984 and 2011," *International Journal of Applied Earth Observations and Geoinformation*, vol. 98, p. 102317, 2021. [Online]. Available: https://doi.org/10.1016/j.jag.2021.102317

[43] J. Ju, D. P. Roy, E. Vermote, J. Masek, and V. Kovalskyy, "Continental-scale validation of MODIS-based and LEDAPS Landsat ETM+ atmospheric correction methods," *Remote Sensing of Environment*, vol. 122, pp. 175–184, 2012. [Online]. Available: https://doi.org/10.1016%2Fj.rse.2011.12.025

[44] J. Masek, E. Vermote, N. Saleous, R. Wolfe, F. Hall, K. Huemmrich, F. Gao, J. Kutler, and T.-K. Lim, "A Landsat Surface Reflectance Dataset for North America, 1990–2000," *IEEE Geoscience and Remote Sensing Letters*, vol. 3, no. 1, pp. 68–72, 2006. [Online]. Available: https://doi.org/10.1109%2Flgrs.2005.857030

[45] E. Vermote, C. Justice, M. Claverie, and B. Franch, "Preliminary analysis of the performance of the Landsat 8/OLI land surface reflectance product," *Remote Sensing of Environment*, vol. 185, pp. 46–56, 2016. [Online]. Available: https://doi.org/10.1016%2Fj.rse.2016.04.008

[46] G. Chander and B. Markham, "Revised landsat-5 tm radiometric calibration procedures and postcalibration dynamic ranges," *IEEE Transactions on Geoscience and Remote Sensing*, vol. 41, no. 11, pp. 2674–2677, 2003. [Online]. Available: https://doi.org/10.1109%2Ftgrs.2003.818464

[47] G. Chander, D. Helder, B. Markham, J. Dewald, E. Kaita, K. Thome, E. Micijevic, and T. Ruggles, "Landsat-5 TM reflective-band absolute radiometric calibration," *IEEE Transactions on Geoscience and Remote Sensing*, vol. 42, no. 12, pp. 2747–2760, 2004. [Online]. Available: https://doi.org/10.1109%2Ftgrs.2004.836388

[48] G. Chander, B. L. Markham, and D. L. Helder, "Summary of current radiometric calibration coefficients for Landsat MSS, TM, ETM+, and EO-1 ALI sensors," *Remote Sensing of Environment*, vol. 113, no. 5, pp. 893–903, 2009. [Online]. Available: https://doi.org/10.1016%2Fj.rse.2009.01.007

[49] B. L. Markham and D. L. Helder, "Forty-year calibrated record of earth-reflected radiance from Landsat: A review," *Remote Sensing of Environment*, vol. 122, pp. 30–40, 2012. [Online]. Available: https://doi.org/10.1016%2Fj.rse.2011.06.026

[50] M. Claverie, E. F. Vermote, B. Franch, and J. G. Masek, "Evaluation of the Landsat-5 TM and Landsat-7 ETM+ surface reflectance products," *Remote Sensing of Environment*, vol. 169, pp. 390–403, 2015. [Online]. Available: https://doi.org/10.1016%2Fj.rse.2015.08.030

[51] D. Lee, J. Storey, M. Choate, and R. Hayes, "Four years of Landsat-7 on-orbit geometric calibration and performance," *IEEE Transactions on Geoscience and Remote Sensing*, vol. 42, no. 12, pp. 2786–2795, 2004. [Online]. Available: https://doi.org/10.1109%2Ftgrs.2004.836769

[52] M. Friedl and D. Sulla-Menashe, "MCD12C1 MODIS/Terra+Aqua Land Cover Type Yearly L3 Global 0.05Deg CMG V006," 2015. [Online]. Available: https://doi.org/10.5067/MODIS/MCD12C1.006

[53] A. Pérez-Hoyos, F. García-Haro, and J. San-Miguel-Ayanz, "Conventional and fuzzy comparisons of large scale land cover products: Application to CORINE, GLC2000, MODIS and GlobCover in Europe," *ISPRS Journal of Photogrammetry and Remote Sensing*, vol. 74, pp. 185–201, 2012. [Online]. Available: https://doi.org/10.1016%2Fj.isprsjprs.2012.09.006

[54] J. Pearlman, P. Barry, C. Segal, J. Shepanski, D. Beiso, and S. Carman, "Hyperion, a space-based imaging spectrometer," *IEEE Transactions on Geoscience and Remote Sensing*, vol. 41, no. 6, pp. 1160–1173, 2003. [Online]. Available: https://doi.org/10.1109%2Ftgrs.2003.815018

[55] M. Broomhall, "Auscover/curtin hyperion enhancement and atmospheric correction technique atbd," 2012. [Online]. Available: http://www.auscover.org.au/purl/hyperspectral-surf-refl-hyperion

[56] J. Chambers, "Lba-eco cd-34 hyperion 30-m surface reflectance, amazon basin: 2002-2005," *ORNL DAAC, Oak Ridge, Tennessee, USA.*, 2012.

[57] G. Chander, N. Mishra, D. L. Helder, D. B. Aaron, A. Angal, T. Choi, X. Xiong, and D. R. Doelling, "Applications of Spectral Band Adjustment Factors (SBAF) for Cross-Calibration," *IEEE Transactions on Geoscience and Remote Sensing*, vol. 51, no. 3, pp. 1267–1281, 2013. [Online]. Available: https://doi.org/10.1109%2Ftgrs.2012.2228007

[58] W. J. van Leeuwen, B. J. Orr, S. E. Marsh, and S. M. Herrmann, "Multi-sensor NDVI data continuity: Uncertainties and implications for vegetation monitoring applications," *Remote Sensing of Environment*, vol. 100, no. 1, pp. 67–81, 2006. [Online]. Available: https://doi.org/10.1016%2Fj.rse.2005.10.002

[59] S. Skakun, C. O. Justice, E. Vermote, and J.-C. Roger, "Transitioning from MODIS to VIIRS: an analysis of inter-consistency of NDVI data sets for agricultural monitoring," *International Journal of Remote Sensing*, vol. 39, no. 4, pp. 971–992, 2017. [Online]. Available: https://doi.org/10.1080%2F01431161.2017.1395970

[60] D. R. Doelling, C. Lukashin, P. Minnis, B. Scarino, and D. Morstad, "Spectral Reflectance Corrections for Satellite Intercalibrations Using SCIAMACHY Data," *IEEE Geoscience and Remote Sensing Letters*, vol. 9, no. 1, pp. 119–123, 2012. [Online]. Available: https://doi.org/10.1109%2Flgrs.2011.2161751

[61] T. Miura, A. Huete, and H. Yoshioka, "An empirical investigation of cross-sensor relationships of NDVI and red/near-infrared reflectance using EO-1 Hyperion data," *Remote Sensing of Environment*, vol. 100, no. 2, pp. 223–236, 2006. [Online]. Available: https://doi.org/10.1016%2Fj.rse.2005.10.010

[62] M. M. Breunig, H.-P. Kriegel, R. T. Ng, and J. Sander, "LOF: identifying density-based local outliers," in *Proceedings of the 2000 ACM SIGMOD international conference on Management of data - SIGMOD '00*, 2000. [Online]. Available: https://doi.org/10.1145%2F342009.335388

[63] F.-M. Bréon and E. Vermote, "Correction of MODIS surface reflectance time series for BRDF effects," *Remote Sensing of Environment*, vol. 125, pp. 1–9, 2012. [Online]. Available: https://doi.org/10.1016%2Fj.rse.2012.06.025

[64] B. Franch, E. Vermote, S. Skakun, J.-C. Roger, J. Masek, J. Ju, J. Villaescusa-Nadal, and A. Santamaria-Artigas, "A Method for Landsat and Sentinel 2 (HLS) BRDF Normalization," *Remote Sensing*, vol. 11, no. 6, p. 632, 2019. [Online]. Available: https://doi.org/10.3390%2Frs11060632

[65] E. C. B. de Colstoun and C. L. Walthall, "Improving global scale land cover classifications with multi-directional POLDER data and a decision tree classifier," *Remote Sensing of Environment*, vol. 100, no. 4, pp. 474–485, 2006. [Online]. Available: https://doi.org/10.1016%2Fj.rse.2005.11.003

[66] A. Mahtab, V. N. Sridhar, and R. R. Navalgund, "An assessment of angular variations of red and NIR reflectances in multi-date IRS-1D Wide Field Sensor data," *International Journal of Remote Sensing*, vol. 30, no. 17, pp. 4599–4619, 2009. [Online]. Available: https://doi.org/10.1080%2F01431160802621226

[67] Y. J. Kaufman, "Satellite sensing of aerosol absorption," *Journal of Geophysical Research*, vol. 92, no. D4, p. 4307, 1987. [Online]. Available: https://doi.org/10.1029%2Fjd092id04p04307

[68] R. Kaufmann, L. Zhou, Y. Knyazikhin, V. Shabanov, R. Myneni, and C. Tucker, "Effect of orbital drift and sensor changes on the time series of AVHRR vegetation index data," *IEEE Transactions on Geoscience and Remote Sensing*, vol. 38, no. 6, pp. 2584–2597, 2000. [Online]. Available: https://doi.org/10.1109%2F36.885205

[69] R. Latifovic, D. Pouliot, and C. Dillabaugh, "Identification and correction of systematic error in NOAA AVHRR long-term satellite data record," *Remote Sensing of Environment*, vol. 127, pp. 84–97, 2012. [Online]. Available: https://doi.org/10.1016%2Fj.rse.2012.08.032

[70] M. Feng, J. O. Sexton, C. Huang, J. G. Masek, E. F. Vermote, F. Gao, R. Narasimhan, S. Channan, R. E. Wolfe, and J. R. Townshend, "Global surface reflectance products from Landsat: Assessment using coincident MODIS observations," *Remote Sensing of Environment*, vol. 134, pp. 276–293, 2013. [Online]. Available: https://doi.org/10.1016%2Fj.rse.2013.02.031

[71] C. Justice, T. F. Eck, D. Tanré, and B. N. Holben, "The effect of water vapour on the normalized difference vegetation index derived for the sahelian region from NOAA AVHRR data," *International Journal of Remote Sensing*, vol. 12, no. 6, pp. 1165–1187, 1991. [Online]. Available: https://doi.org/10.1080%2F01431169108929720

[72] T. Zhao, J. Wang, and A. Dai, "Evaluation of atmospheric precipitable water from reanalysis products using homogenized radiosonde observations over china," *J. Geophys. Res. Atmos.*, vol. 120, no. 20, pp. 10,703–10,727, oct 2015. [Online]. Available: https://doi.org/10.1002%2F2015jd023906

[73] S. Wang, T. Xu, W. Nie, C. Jiang, Y. Yang, Z. Fang, M. Li, and Z. Zhang, "Evaluation of precipitable water vapor from five reanalysis products with ground-based GNSS observations," *Remote Sensing*, vol. 12, no. 11, p. 1817, jun 2020. [Online]. Available: https://doi.org/10.3390%2Frs12111817

[74] A. Makarau, R. Richter, D. Schlapfer, and P. Reinartz, "APDA water vapor retrieval validation for sentinel-2 imagery," *IEEE Geoscience and Remote Sensing Letters*, vol. 14, no. 2, pp. 227–231, feb 2017. [Online]. Available: https://doi.org/10.1109%2Flgrs.2016.2635942

[75] J. Fischer, R. Leinweber, and R. Preusker, "Retrieval of total water vapour content from olci measurements. atbd," Tech. Rep., 2010. [Online]. Available: https://doi.org/10.1080%2F01431169108929720

[76] G. Dalu, "Satellite remote sensing of atmospheric water vapour," *International Journal of Remote Sensing*, vol. 7, no. 9, pp. 1089–1097, sep 1986. [Online]. Available: https://doi.org/10.1080%2F01431168608948911

[77] C. C. Walton, "Nonlinear multichannel algorithms for estimating sea surface temperature with AVHRR satellite data," *J. Appl. Meteor.*, vol. 27, no. 2, pp. 115–124, feb 1988. [Online]. Available: https://doi.org/10.1175%2F1520-0450%281988%29027%3C0115%3Anmafes%3E2.0.co%3B2

[78] K. A. Kilpatrick, G. P. Podestá, and R. Evans, "Overview of the NOAA/NASA advanced very high resolution radiometer pathfinder algorithm for sea surface temperature and associated matchup database," *J. Geophys. Res.*, vol. 106, no. C5, pp. 9179–9197, may 2001. [Online]. Available: https://doi.org/10.1029%2F1999jc000065

[79] F. Becker and Z.-L. Li, "Towards a local split window method over land surfaces," *International Journal of Remote Sensing*, vol. 11, no. 3,

pp. 369–393, mar 1990. [Online]. Available: https://doi.org/10.1080%2F01431169008955028

[80] J. Sobrino, C. Coll, and V. Caselles, "Atmospheric correction for land surface temperature using NOAA-11 AVHRR channels 4 and 5," *Remote Sensing of Environment*, vol. 38, no. 1, pp. 19–34, oct 1991. [Online]. Available: https://doi.org/10.1016%2F0034-4257%2891%2990069-i

[81] J. Sobrino, N. Raissouni, J. Simarro, F. Nerry, and F. Petitcolin, "Atmospheric water vapor content over land surfaces derived from the AVHRR data: application to the iberian peninsula," *IEEE Transactions on Geoscience and Remote Sensing*, vol. 37, no. 3, pp. 1425–1434, may 1999. [Online]. Available: https://doi.org/10.1109%2F36.763306

[82] Z. Li, J.-P. Muller, and P. Cross, "Comparison of precipitable water vapor derived from radiosonde, gps, and moderate-resolution imaging spectroradiometer measurements," *Journal of Geophysical Research: Atmospheres*, vol. 108, no. D20, 2003. [Online]. Available: https://agupubs.onlinelibrary.wiley.com/doi/abs/10.1029/2003JD003372

[83] J. Vaquero-Martínez, M. Antón, J. P. O. de Galisteo, V. E. Cachorro, M. J. Costa, R. Román, and Y. S. Bennouna, "Validation of MODIS integrated water vapor product against reference GPS data at the iberian peninsula," *International Journal of Applied Earth Observation and Geoinformation*, vol. 63, pp. 214–221, dec 2017. [Online]. Available: https://doi.org/10.1016%2Fj.jag.2017.07.008

[84] Y. S. Bennouna, B. Torres, V. E. Cachorro, J. P. O. de Galisteo, and C. Toledano, "The evaluation of the integrated water vapour annual cycle over the iberian peninsula from EOS-MODIS against different ground-based techniques," *Q.J.R. Meteorol. Soc.*, vol. 139, no. 676, pp. 1935–1956, jan 2013. [Online]. Available: https://doi.org/10.1002%2Fqj.2080

[85] V. S. Martins, A. Lyapustin, Y. Wang, D. M. Giles, A. Smirnov, I. Slutsker, and S. Korkin, "Global validation of columnar water vapor derived from EOS MODIS-MAIAC algorithm against the ground-based AERONET observations," *Atmospheric Research*, vol. 225, pp. 181–192, sep 2019. [Online]. Available: https://doi.org/10.1016%2Fj.atmosres.2019.04.005

[86] F. Shi, J. Xin, L. Yang, Z. Cong, R. Liu, Y. Ma, Y. Wang, X. Lu, and L. Zhao, "The first validation of the precipitable water vapor of multisensor satellites over the typical regions in china," *Remote Sensing of Environment*, vol. 206, pp. 107–122, mar 2018. [Online]. Available: https://doi.org/10.1016%2Fj.rse.2017.12.022

[87] B. Holben, T. Eck, I. Slutsker, D. Tanré, J. Buis, A. Setzer, E. Vermote, J. Reagan, Y. Kaufman, T. Nakajima, F. Lavenu,

I. Jankowiak, and A. Smirnov, "AERONET—a federated instrument network and data archive for aerosol characterization," *Remote Sensing of Environment*, vol. 66, no. 1, pp. 1–16, oct 1998. [Online]. Available: https://doi.org/10.1016%2Fs0034-4257%2898%2900031-5

[88] D. M. Giles, A. Sinyuk, M. G. Sorokin, J. S. Schafer, A. Smirnov, I. Slutsker, T. F. Eck, B. N. Holben, J. R. Lewis, J. R. Campbell, E. J. Welton, S. V. Korkin, and A. I. Lyapustin, "Advancements in the aerosol robotic network (AERONET) version 3 database – automated near-real-time quality control algorithm with improved cloud screening for sun photometer aerosol optical depth (AOD) measurements," *Atmos. Meas. Tech.*, vol. 12, no. 1, pp. 169–209, jan 2019. [Online]. Available: https://doi.org/10.5194%2Famt-12-169-2019

[89] C. Mattar, C. Durán-Alarcón, J. C. Jiménez-Muñoz, A. Santamaría-Artigas, L. Olivera-Guerra, and J. A. Sobrino, "Global atmospheric profiles from reanalysis information (GAPRI): a new database for earth surface temperature retrieval," *International Journal of Remote Sensing*, vol. 36, no. 19-20, pp. 5045–5060, jun 2015. [Online]. Available: https://doi.org/10.1080%2F01431161.2015.1054965

[90] D. P. Dee, S. M. Uppala, A. J. Simmons, P. Berrisford, P. Poli, S. Kobayashi, U. Andrae, M. A. Balmaseda, G. Balsamo, P. Bauer, P. Bechtold, A. C. M. Beljaars, L. van de Berg, J. Bidlot, N. Bormann, C. Delsol, R. Dragani, M. Fuentes, A. J. Geer, L. Haimberger, S. B. Healy, H. Hersbach, E. V. Hólm, L. Isaksen, P. Kållberg, M. Köhler, M. Matricardi, A. P. McNally, B. M. Monge-Sanz, J.-J. Morcrette, B.-K. Park, C. Peubey, P. de Rosnay, C. Tavolato, J.-N. Thépaut, and F. Vitart, "The ERA-interim reanalysis: configuration and performance of the data assimilation system," *Q.J.R. Meteorol. Soc.*, vol. 137, no. 656, pp. 553–597, apr 2011. [Online]. Available: https://doi.org/10.1002%2Fqj.828

[91] R. Saunders, J. Hocking, E. Turner, P. Rayer, D. Rundle, P. Brunel, J. Vidot, P. Roquet, M. Matricardi, A. Geer, N. Bormann, and C. Lupu, "An update on the RTTOV fast radiative transfer model (currently at version 12)," *Geosci. Model Dev.*, vol. 11, no. 7, pp. 2717–2737, jul 2018. [Online]. Available: https://doi.org/10.5194%2Fgmd-11-2717-2018

[92] F. Baret, J. Morissette, R. Fernandes, J. Champeaux, R. Myneni, J. Chen, S. Plummer, M. Weiss, C. Bacour, S. Garrigues, and J. Nickeso, "Evaluation of the representativeness of networks of sites for the global validation and intercomparison of land biophysical products: proposition of the CEOS-BELMANIP," *IEEE Transactions on Geoscience and Remote Sensing*, vol. 44, no. 7, pp. 1794–1803, jul 2006. [Online]. Available: https://doi.org/10.1109%2Ftgrs.2006.876030

[93] M. D. King, S. Platnick, W. P. Menzel, S. A. Ackerman, and P. A. Hubanks, "Spatial and temporal distribution of clouds observed by MODIS onboard the terra and aqua satellites," *IEEE Transactions on Geoscience and Remote Sensing*, vol. 51, no. 7, pp. 3826–3852, jul 2013. [Online]. Available: https://doi.org/10.1109%2Ftgrs.2012.2227333

[94] B. Chen and Z. Liu, "Global water vapor variability and trend from the latest 36 year (1979 to 2014) data of ECMWF and NCEP reanalyses, radiosonde, GPS, and microwave satellite," *J. Geophys. Res. Atmos.*, vol. 121, no. 19, pp. 11,442–11,462, oct 2016. [Online]. Available: https://doi.org/10.1002%2F2016jd024917

[95] A. T. Evan, C. Flamant, C. Lavaysse, C. Kocha, and A. Saci, "Water vapor–forced greenhouse warming over the sahara desert and the recent recovery from the sahelian drought," *Journal of Climate*, vol. 28, no. 1, pp. 108–123, dec 2014. [Online]. Available: https://doi.org/10.1175%2Fjcli-d-14-00039.1

[96] C. M. Taylor, D. Belušić, F. Guichard, D. J. Parker, T. Vischel, O. Bock, P. P. Harris, S. Janicot, C. Klein, and G. Panthou, "Frequency of extreme sahelian storms tripled since 1982 in satellite observations," *Nature*, vol. 544, no. 7651, pp. 475–478, apr 2017. [Online]. Available: https://doi.org/10.1038%2Fnature22069

[97] R. B. Myneni, C. J. Tucker, G. Asrar, and C. D. Keeling, "Interannual variations in satellite-sensed vegetation index data from 1981 to 1991," *J. Geophys. Res.*, vol. 103, no. D6, pp. 6145–6160, mar 1998. [Online]. Available: https://doi.org/10.1029%2F97jd03603

[98] G. G. Gutman, "On the use of long-term global data of land reflectances and vegetation indices derived from the advanced very high resolution radiometer," *J. Geophys. Res.*, vol. 104, no. D6, pp. 6241–6255, mar 1999. [Online]. Available: https://doi.org/10.1029%2F1998jd200106

[99] G. Chander, T. J. Hewison, N. Fox, X. Wu, X. Xiong, and W. J. Blackwell, "Overview of intercalibration of satellite instruments," *IEEE Transactions on Geoscience and Remote Sensing*, vol. 51, no. 3, pp. 1056–1080, mar 2013. [Online]. Available: https://doi.org/10.1109%2Ftgrs.2012.2228654

[100] H. Cosnefroy, M. Leroy, and X. Briottet, "Selection and characterization of saharan and arabian desert sites for the calibration of optical satellite sensors," *Remote Sensing of Environment*, vol. 58, no. 1, pp. 101–114, oct 1996. [Online]. Available: https://doi.org/10.1016%2F0034-4257%2895%2900211-1

[101] W. F. Staylor and J. T. Suttles, "Reflection and emission models for deserts derived from nimbus-7 ERB scanner measurements," *J. Climate Appl. Meteor.*, vol. 25, no. 2, pp. 196–202, feb 1986. [Online].

Available: https://doi.org/10.1175%2F1520-0450%281986%29025%3C0196%3Araemfd%3E2.0.co%3B2

[102] V. Maus, G. Camara, R. Cartaxo, A. Sanchez, F. M. Ramos, and G. R. de Queiroz, "A time-weighted dynamic time warping method for land-use and land-cover mapping," *IEEE Journal of Selected Topics in Applied Earth Observations and Remote Sensing*, vol. 9, no. 8, pp. 3729–3739, aug 2016. [Online]. Available: https://doi.org/10.1109%2Fjstars.2016.2517118

[103] O. Csillik, M. Belgiu, G. P. Asner, and M. Kelly, "Object-based time-constrained dynamic time warping classification of crops using sentinel-2," *Remote Sensing*, vol. 11, no. 10, p. 1257, may 2019. [Online]. Available: https://doi.org/10.3390%2Frs11101257

[104] D. R. Doelling, B. R. Scarino, D. Morstad, A. Gopalan, R. Bhatt, C. Lukashin, and P. Minnis, "The intercalibration of geostationary visible imagers using operational hyperspectral SCIAMACHY radiances," *IEEE Transactions on Geoscience and Remote Sensing*, vol. 51, no. 3, pp. 1245–1254, mar 2013. [Online]. Available: https://doi.org/10.1109%2Ftgrs.2012.2227760

[105] S. Uprety and C. Cao, "Radiometric and spectral characterization and comparison of the antarctic dome c and sonoran desert sites for the calibration and validation of visible and near-infrared radiometers," *Journal of Applied Remote Sensing*, vol. 6, no. 1, p. 063541, jul 2012. [Online]. Available: https://doi.org/10.1117%2F1.jrs.6.063541

[106] T. chung Fu, "A review on time series data mining," *Engineering Applications of Artificial Intelligence*, vol. 24, no. 1, pp. 164–181, feb 2011. [Online]. Available: https://doi.org/10.1016%2Fj.engappai.2010.09.007

[107] S. Lhermitte, J. Verbesselt, W. Verstraeten, and P. Coppin, "A comparison of time series similarity measures for classification and change detection of ecosystem dynamics," *Remote Sensing of Environment*, vol. 115, no. 12, pp. 3129–3152, dec 2011. [Online]. Available: https://doi.org/10.1016%2Fj.rse.2011.06.020

[108] D. J. Berndt and J. Clifford, "Using dynamic time warping to find patterns in time series," in *Proceedings of the 3rd International Conference on Knowledge Discovery and Data Mining*, ser. AAAIWS'94. AAAI Press, 1994, p. 359–370.

[109] T. Rakthanmanon, B. Campana, A. Mueen, G. Batista, B. Westover, Q. Zhu, J. Zakaria, and E. Keogh, "Searching and mining trillions of time series subsequences under dynamic time warping," in *Proceedings of the 18th ACM SIGKDD international conference on Knowledge discovery and data mining - KDD '12*. ACM Press, 2012. [Online]. Available: https://doi.org/10.1145%2F2339530.2339576

[110] H. Ding, G. Trajcevski, P. Scheuermann, X. Wang, and E. Keogh, "Querying and mining of time series data: Experimental comparison of representations and distance measures," *Proc. VLDB Endow.*, vol. 1, no. 2, p. 1542–1552, Aug. 2008. [Online]. Available: https://doi.org/10.14778/1454159.1454226

[111] E. Vermote, D. Tanré, J. L. Deuze, M. Herman, J. J. Morcrette, and S. Y. Kotchenova, "Second Simulation of a Satellite Signal in the Solar Spectrum - Vector (6SV) User Manual V3," vol. Part1, 2006.

[112] E. Vermote, J. McCorkel, W. Rountree, A. Santamaría-Artigas, S. Skakun, B. Franch, and J. Roger, "Validation Of High Spatial Resolution Surface Reflectance Using A Camera System (CAMSIS)," in *American Geophysical Union (AGU) Fall Meeting*, San Francisco, CA, USA, 2019.

[113] K. Ccoica-López, J. Pasapera-Gonzales, and J. Jimenez, "Spatio-temporal variability of the precipitable water vapor over peru through MODIS and ERA-interim time series," *Atmosphere*, vol. 10, no. 4, p. 192, apr 2019. [Online]. Available: https://doi.org/10.3390%2Fatmos10040192

[114] L. Mei, C. Zhao, G. Leeuw, J. P. Burrows, V. Rozanov, H. Che, M. Vountas, A. Ladstätter-Weißenmayer, and X. Zhang, "A critical evaluation of deep blue algorithm derived AVHRR aerosol product over china," *J. Geophys. Res. Atmos.*, vol. 124, no. 22, pp. 12 173–12 193, nov 2019. [Online]. Available: https://doi.org/10.1029%2F2018jd029929

[115] J. Roger and E. Vermote, "A method to retrieve the reflectivity signature at 3.75 μm from AVHRR data," *Remote Sensing of Environment*, vol. 64, no. 1, pp. 103–114, apr 1998. [Online]. Available: https://doi.org/10.1016%2Fs0034-4257%2897%2900173-9